Mass Optimization and Experimental Validation of a Forced-Convection Heat Exchanger for Mars Surface Waste Heat Rejection

By

Nathan Colgan

A dissertation submitted in partial fulfillment of

the requirements for the degree of

Doctor of Philosophy

(Nuclear Engineering and Engineering Physics)

at the

UNIVERSITY OF WISCONSIN - MADISON

2023

Date of oral examination: 05/10/2023

The dissertation is approved by the following members of the Final Oral Committee:

Mark Anderson, Professor, Mechanical Engineering

Gregory Nellis, Professor, Mechanical Engineering

John Pfotenhauer, Professor, Mechanical Engineering

Paul Wilson, Professor, Chair, Engineering Physics

Ricardo Bonazza, Professor, Associate Chair, Engineering Physics

Abstract

NASA and other space agencies are currently planning the first human missions to Mars in the next 20 years. These missions will require much more power than current robotic missions, and so will require significant waste heat rejection capabilities to maintain steady state operations. Forced convection heat exchangers, particularly crossflow tube array compact heat exchangers, may offer significant volume- and mass-efficiency benefits over radiators for these applications. However, no experimentally validated correlations exist in the literature for the pressure drop and heat transfer characteristics of a forced-convection heat exchanger under the relevant dimensionless conditions which correspond to low (7-200) Reynolds number and moderate (0.0009-0.009) Knudsen number under axial and vortical flows. A staggered-tube crossflow heat exchanger has been constructed and its performance experimentally measured in a low-density wind tunnel. Data has been gathered in low-Reynolds, moderate-Knudsen conditions for both axial and vortical flows over a range of pressures and wall temperatures that is relevant to future Mars or high-altitude heat exchanger operation using both CO_2 and air. The measured pressure drop exceeds what is predicted by correlations in the literature at very low (<75) Reynolds number while the Nusselt numbers were fairly well-predicted by existing correlations. A new correlation for pressure drop is presented for low-Reynolds, axial and vortical flow through a staggered circular tube array in crossflow.

A detailed heat exchanger model is developed using these correlations and the heat exchanger geometry is optimized to minimize the overall system mass for a range of candidate heat exchanger materials and heat transfer rates. Curve fits that capture the heat exchanger

performance are generated based on the input conditions in order to develop a reduced order model that can be used to integrate the heat exchanger model with an existing recuperated Brayton cycle high-temperature gas cooled reactor (HTGR) power cycle model. This power cycle model is used to determine the impact of using convective heat rejection on optimal system mass and compare this approach to radiative heat rejection. For a 40 kW_e power output, the optimal overall cycle mass is found to decrease by 78% when using convective heat rejection compared to a radiator; this is due to the decreased mass of the heat rejection system as well as the lower optimal rejection temperature which results in a lower recuperator mass. The heat exchanger itself has a mass of only 37 kg, a frontal area of 11.3 m^2, and requires 1806 W of fan power to operate. The system is shown to perform well over a wide range of Mars ambient conditions. A high-power LOx cryocooler cycle is also modeled to determine the benefit of using convective heat rejection for in-situ resource utilization (ISRU) applications. Across a range of power source options and ambient temperatures, using a convective heat rejection system reduced total system mass and size compared to a radiator and also reduced the mass-optimal cycle power draw by increasing the optimal cycle efficiency. Overall, this technology offers significant performance advantages over radiative heat rejection systems for waste heat rejection applications on Mars and therefore may significantly benefit future crewed Mars missions.

Acknowledgements

Firstly I would like to thank my parents, Brian and Judi Colgan, for your unending support and encouragement throughout my academic career, although I'm sure it was longer than any of us expected. You've always taken a strong interest in my education, from asking what I learned in school every day at dinner to calling to ask how my heat exchanger modelling was going or whether I ever got those sCO_2 pumps working. I would also like to thank my sister Jen for always being there for me, whether for emotional support, life and career advice, or just to kvetch. Thanks as well to Josh, Pete and Steph for all your support and for listening to me complain about grad school during most recent holidays and gatherings. Finally, I would like to thank Aunt Mil and Nana Bertha for all your love and support.

I would also like to thank my advisors, Mark Anderson and Greg Nellis. Greg, your insights into heat exchanger modelling and design and experimental data analysis have been invaluable, as well as your endless patience editing all of my overly-long papers. Mark, thank you for guidance during the experimental design, construction, and data collection phases of the project and for all the lab equipment you've let me borrow so I could stay within my budget. I would also like to thank the member of my committee, John Pfotenhauer, Paul Wilson, and Ricardo Bonazza. I owe a great deal also to Paul Brooks and Seth Jones for all your advice and help on building and testing my heat exchanger. Finally, I would also like to thank my Master's advisor Caleb Brooks for his support during my time at UIUC.

Finally, thanks to all the members of the SEL, particularly Andrew, Ryder, Lewis, Ian, Will, Evan, Mackenzie, Tiago, and Erik, to my friends in the Nuclear department, particularly Carolyn,

Ricardo, Lucas, Max, Katie, and Jon, to all my friends in the Madison Jewish community, to the members of the UW Sport Taekwondo team for making my time in grad school more fun and meaningful than I ever thought it would be.

Table of Contents

List of Figures

List of Tables

Nomenclature

a_i	Correlation Parameters, [-]
A	Area, [m^2]
b_i	Correlation Parameters, [-]
c_p	Specific Heat Capacity, [J kg^{-1} K^{-1}]
c_1, c_2	Correlation Parameters, [-]
C	Constant, [-]
$\dot{C}$	Capacitance Rate, [W K^{-1}]
D	Diameter, [m]
DC	Fan Duty Cycle. [-]
D_h	Hydraulic Diameter, [m]
e	RMS Roughness, [m]
err	Error
f	Friction Factor, [-]
G_c	Coolant Pressure Drop Weighting Factor, [kg Pa^{-1}]
G_m	Motor Power Weighting Factor, [kg W_e^{-1}]
G_r	Reactor Power Weighting Factor, [kg W_e^{-1}]
h	Specific Enthalpy, [J kg^{-1}]
$\overline{h}$	Average Heat Transfer Coefficient, [W m^{-2} K^{-1}]
H	Height, [m]
hub_{rat}	Hub-to-Fan Diameter Ratio, [-]
k	Thermal Conductivity, [W m^{-1} K^{-1}]
k_B	Boltzmann Constant, [J K^{-1}]
k_{config}	Configuration Factor, [-]
k_{eff}	Effective Multiplication Factor, [-]
k_1, k_2, k_3	Correlation Correction Factors, [-]
K	Anemometer Correction Factors, [-]
L	Length, [m]
m	Mass, [kg]
$\dot{m}$	Mass Flowrate, [kg s^{-1}]
M	Molecular Mass, [kg]
Ma	Mach Number, [-]
MOS	Margin of Safety, [-]
N	Number, [-]
NTU	Number of Transfer Units, [-]
p	Pitch, [m]
P	Pressure, [Pa]
$\dot{Q}$	Thermal Power, [W]
R	Thermal Resistance, [K W^{-1}]
R_e	Electrical Resistance, [Ω]
R_p	Pitch-to-Diameter Ratio, [-]
S_L	Lateral Tube Pitch, [m]
S_T	Transverse Tube Pitch, [m]
S_y	Yield Stress, [Pa]
t	Thickness, [m]
T	Temperature, [K]
u	Velocity, [m s^{-1}]

UA	Conductance, [W K^{-1}]
V	Voltage, [V]
$\dot{V}$	Volumetric Flowrate, [m^3 s^{-1}]
$\dot{W}$	Electrical Power, [W_e]
x	Axial Distance, [m]
α	Power-Specific Mass, [kg W_e^{-1}]
α_{SS}	Stainless Steel Thermal Expansion Coefficient, [K^{-1}]
δ_t	Thermal Boundary Layer Thickness, [m]
ϵ_{HX}	Heat Exchanger Effectiveness
ϵ_{rad}	Emissivity, [-]
ϵ_{por}	Tube Bundle Porosity, [-]
η	Efficiency, [-]
μ	Dynamic Viscosity, [Pa s]
ρ	Density, [kg m^{-3}]
ρ_e	Electrical Resistivity, [Ω m]
σ	Stephan-Boltzman constant, [W m^{-2} K^{-4}]
ϕ	Flow Coefficient, [-]
ψ	Head Coefficient, [-]
ω	Rotational Speed, [rad s^{-1}]

Subscripts

amb	Ambient
$anem$	Anemometer
$blade$	Fan Blade
c	Cold (Atmosphere) Side
cal	calibration
$cols$	Tube Columns
$cool$	Cooling
$comp$	Compressor
$cond$	Conduction
$crit$	Critical
$cryo$	Cryocooler
D_h	Hydraulic Diameter
$duct$	Duct
est	Estimated
exp	Experimental
fan	Fan
fd	Fully-Developed
fin	Fins
$foul$	Fouling
fp	Flat Plate
h	Hot (Coolant) Side
$head$	Header
$HEDH$	Heat Exchanger Design Handbook
HX	Heat Exchanger
in	Inlet
lam	Laminar
lfm	Laminar Flowmeter
$loss$	losses
LOx	Liquid Oxygen
m	Motor
mid	Mid-Chord
min	Minimum

max	Maximum
nc	Natural Convection
Neu	Neustein Correlation
$optim$	Optimal
out	Outlet
p	Pipe
$peak$	Centerline Peaking Factor
pow	Power
$pred$	Predicted
$props$	Properties
r	Refrigerant
R	Ratio
rad	Radiator
rat	Ratio
raw	Uncorrected
rec	Recuperator
rej	Rejected
row	Per tube row
$rows$	Tube Rows
sat	Saturation
$spec$	Mass-specific
$surr$	Surroundings
t	Tube
$Tariq$	Tariq et al. Correlation
tot	Total
$tubes$	Tubes
$turb$	Turbulent
$turbine$	Turbine
u	Velocity
vc	Vacuum Chamber
$wall$	Wall
x	Axial Distance
xs	cross-section

Dimensionless Numbers

Eu	Euler Number
Kn	Knudsen Number
Nu	Nusselt Number
Pr	Prandtl Number
Re	Reynolds Number

1. Introduction

1.1 Motivation

Human exploration of the Martian surface has been a main focus for NASA's Vision for Space Exploration [1] since 2004. While no definitive mission architecture has been decided yet, the Human Exploration of Mars Design Reference Architecture (DRA) 5.0 [2] provides a detailed outline of the requirements of a future crewed Mars mission. Such a mission would yield unprecedented scientific data on Martian geology and climate, potentially determine if life has ever existed on Mars, and provide insight into how early Mars, which seems to have had a magnetic field and thick atmosphere capable of sustaining liquid surface water, eventually lost these Earth-like life-sustaining attributes [2]. Understanding how these processes occur on Mars will significantly improve our understanding of similar processes on Earth and on other potentially-habitable terrestrial planets, of which Mars is the only other example in the Solar System for which human surface exploration is currently feasible. While remote observation and robotic exploration have revealed significant insights into Martian habitability, human researchers are much more efficient at gathering samples and analyzing them, capable of independent decision-making without waiting 6-20 minutes for a command from Earth, more flexible in the tasks they can carry out, and more adaptable and capable of problem solving than a robotic probe [2]. Furthermore, much like the Apollo missions last century and ISS of this century, a crewed Mars mission will be an undertaking of such magnitude that its accomplishment will spur international cooperation, inspire a generation of students to pursue STEM fields, and require advances in numerous fields like power, biotechnology and life support,

robotics, and communications, each of which have far-reaching benefits outside of space exploration [1]. This reference mission envisions a 500 day surface stay by a crew of 6, a pre-placed propellant plant using in-situ resource utilization (ISRU) to generate fuel required for the return trip, multiple long-distance rovers and numerous pieces of high-power scientific equipment such as sub-surface drilling equipment. The current heaviest payload delivered to the Martian surface, the Perseverance rover, has a mass of more than 1025 kg, 52 kg of which is scientific payload [3], and costs an estimated $2.5B [4], implying a cost per landed payload of approximately $50M/kg. While substantial reductions in this amount will necessarily occur before a crewed mission, mass will continue to be a significant cost driver, and any reductions in system mass that will allow for greater scientific payload will be highly desirable. Astronaut EVA time will also be limited so mission hardware that requires significant deployment time and complexity is undesirable. Additionally, current and near-future launch vehicle payload fairings limit the size of mission hardware to approximately 4-8 m.

The estimated electrical power requirement for this initial reference mission is estimated to be 40 kWe, however potential follow-on missions and permanent outposts could require up to 1 MWe [5]. Photovoltaic solar power has a long flight heritage for space missions and does not present additional radiation risk to the crew, however it is highly dependent on local insolation, limiting its usefulness in high latitudes where water ice is more abundant, and requiring significant energy storage capability for nighttime operation and during dust storms, which can last 1 to 2 months and reduce generation by up to 85% [2]. Additionally, due to the low insolation and solar cell efficiency, over 5000m^2 of solar panels would be required to meet the mission power needs, weighing 22.5 tons and necessitating complex deployment mechanisms. A

significant portion of this capacity would have to be deployed robotically as the proposed ISRU plant is to land and generate fuel before crew arrival to reduce risk [2]. Large-scale radioisotope power systems (RPSs) equipped with Stirling engines are also considered due to their flight heritage, simplicity, and insensitivity to local insolation; however, such a system would require 250 kg of ^{238}Pu [2], or roughly 167 times the projected annual production rate in 2023 of 1.5 kg/yr using the existing Advanced Test Reactor and High Flux Isotope Reactor [6], likely requiring the construction of a dedicated reactor similar to the Savannah River Plant, which was capable of producing up to 50 kg/yr [7] until it ceased production in 1988.

In contrast, fission surface power systems (FSPSs) are a promising power source for a crewed Mars mission. Nuclear fission offers high power density and specific power using abundant Uranium fuel, and does not depend on local insolation, reducing landing site constraint and dust storm risk, and decreasing deployment complexity due to the small size of the required system [2]. A fission reactor can produce consistent power throughout the day, reducing the need for energy storage and excess production capacity required by a solar power system, and can operate for up to 10 years without refueling. A FSPS also reduces radiation exposure during a launch mishap relative to a RPS due to the fuel's much lower activity (1 to 10 Ci) prior to reactor startup and design measures to prohibit criticality in the event of water submersion [8]. However, FSPSs present a radiation risk during operation and so must be sited away from crew living quarters and require a radiation shield, which may be constructed of local material to reduce launch mass. The FSPS envisioned in the NASA DRA requires siting 1 km from the base with a shadow shield achieving a dose rate at the base of 5 rem/year, requiring a mobile deployment mechanism and a long power cable [2]. FSPSs also have little flight heritage. NASA has flown a

single rudimentary fission reactor, SNAP-10A in 1965 which produced 500 W of electrical power for 43 days [9].

Waste heat rejection is a significant challenge for space reactors. As even the most efficient power conversion systems can only achieve 40-60% efficiency, significant thermal energy must be dissipated to the environment to sustain steady operation and prevent overheating. While this waste heat could potentially be used in low-temperature applications requiring significant heat such as melting ice for drinking water or ISRU feedstock or as ISRU process heat, an independent waste heat rejection system would still be required so that the reactor operation does not become tightly coupled to another process, increasing risk. In a vacuum, thermal radiation is the only viable method of heat transfer to the environment. Therefore, radiators have a long flight heritage as waste heat rejection systems on spacecraft, including on SNAP-10A [9]. However, radiators have a few significant drawbacks that limit their utility. Thermal radiation provides a relatively low heat transfer rate compared to convection except at very high temperatures as the heat transfer rate scales with temperature to the 4th power, as shown in Equation 1 below.

$$\dot{Q}_{rad} = \epsilon_{rad}\sigma A(T_{rad}^4 - T_{surr}^4) \quad (1)$$

where ϵ_{rad} is the emissivity, σ is the Stefan-Boltzmann constant, A is the surface area, T_{rad} is the surface temperature, and T_{surr} is the temperature of the surroundings. Therefore, in order to transfer large amounts of heat, radiators require either a large surface area exposed to the surroundings, which increases system mass and deployment complexity, or a high rejection

temperature, which decreases overall thermal efficiency. In general, reactor mass does not scale linearly with power output for low-power reactors as the core geometry is driven by criticality requirements but radiator area, and therefore mass, does increase linearly with dissipated power. Therefore, at higher power output levels, the radiator can become the most massive component of the power system. For example, Sondelski performed a mass optimization study on a supercritical CO_2 (sCO_2) cooled high-temperature gas reactor (HTGR) coupled to a recuperated Brayton cycle power conversion system designed to generate 40 kW_e on the Martian surface using regolith as a radiation shield to reduce mass [10]. A diagram of this cycle is shown in Figure 1. This study assumed a solid highly enriched uranium (HEU) core and did not account for the mass of any shielding. It also did not consider the mass of control elements or the mass of the turbomachinery. As such, this model produces low system mass estimates compared to other studies in the literature of Mars FSPS sizing and it found that the radiator accounted for the majority of the total system mass, 570 kg out of 782 kg. Because of the high radiator mass, the optimization tended to push the compressor inlet temperature away from the vapor dome as shown in Figure 2, resulting in a substantial reduction in the fluid density entering the compressor which negated the primary benefit of using supercritical power cycles. As a result, the cycle efficiency was only 27% and required an 84.4 m^2 radiator. Additionally, the heat transfer area must also have a line-of-sight to the environment to dissipate heat so a large radiator will require complex deployment mechanisms involving coolant channel connections to fit within a launch vehicle fairing, increasing system complexity.

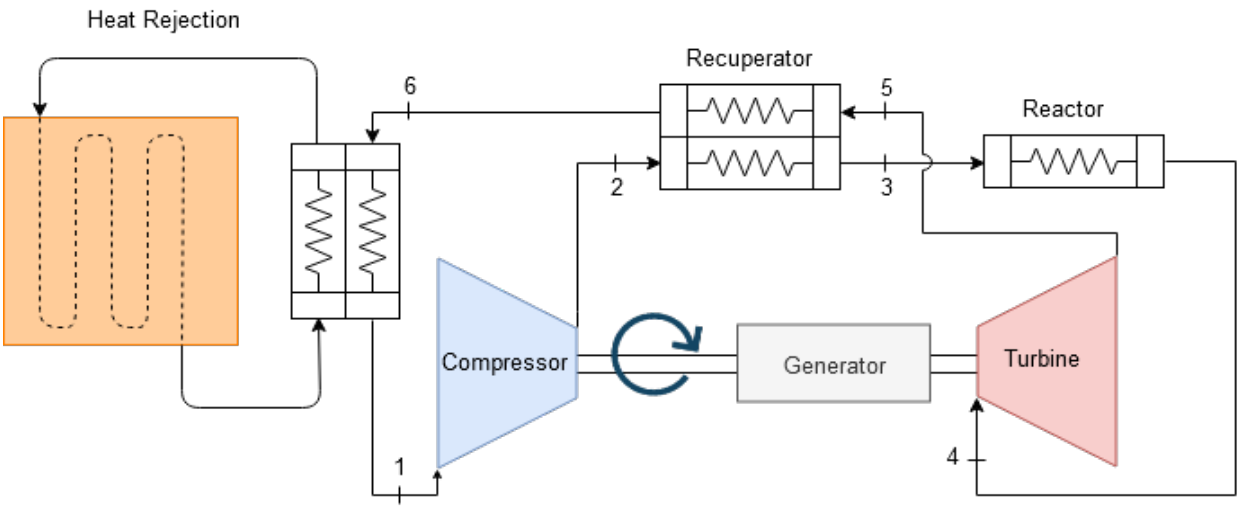

Figure 1: Diagram of a recuperated Brayton cycle power conversion system, from Sondelski [9]

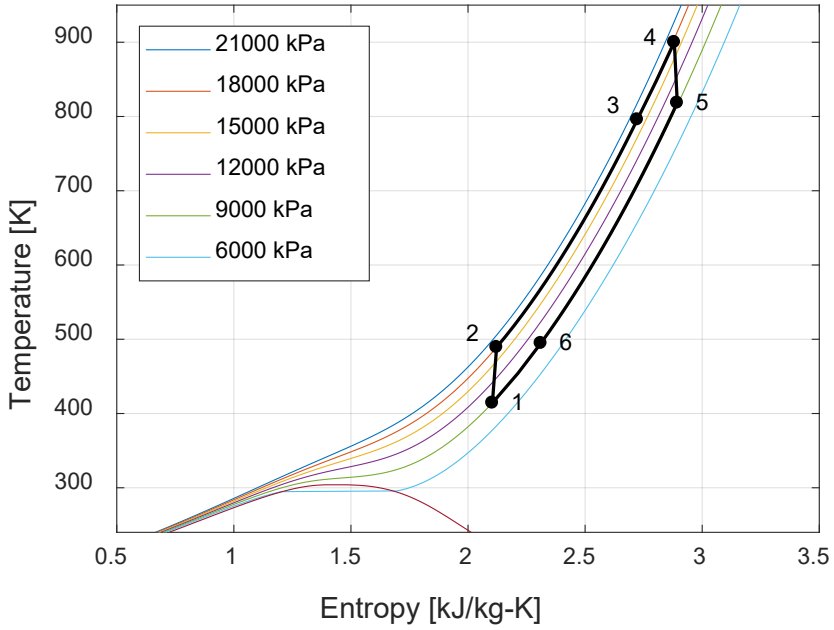

Figure 2: T-s diagram of the mass-optimal cycle found by Sondelski [9] using radiative heat rejection. The high minimum cycle temperature reduces thermal efficiency but minimizes radiator mass.

Morrison also examined the scaling relationships of component masses of a closed-Brayton-Cycle FSPS to determine the lowest-possible power specific mass [11] given current or

near-future technology. For a 15 MWe system with a maximum temperature of 1500 K, the radiator, consisting of heat pipes brazed to Carbon fiber textile stowable sheets with an area mass density of 3.5 kg/m^2, would mass 18.1 tons or 26% of the total system mass and require a surface area of 6390 m^2 and the overall specific mass of the system would be 9.22 kg/kW_e.

However, a Mars surface reactor may be able to avoid these issues by rejecting heat convectively to the atmosphere using a forced-convection heat exchanger. Convection offers much higher heat transfer coefficients than radiation, a weaker dependence on temperature, and does not require the heat transfer surface to be exposed to the sky, allowing for a much more compact structure and reducing deployment complexity. The Martian atmosphere presents a number of challenges to convection waste heat rejection. The atmosphere consists of 95% CO_2, with the balance Nitrogen and Argon, at an average pressure of 600 Pa and average temperature of -60°C, although temperatures can reach as high as 20°C at noon with diurnal temperature swings of 60°C, and pressure can vary 200 Pa throughout the year as the CO_2 polar caps sublimate and freeze with the seasons. The resulting low atmospheric density, leads to low predicted Nusselt numbers in a convective heat exchanger, so a large surface area and high flow rate are required to transfer sufficient heat. A high flow rate will tend to create a high pressure loss in the heat exchanger (relative to the atmospheric pressure), but the achievable fan static pressure rise required to drive the flow through the heat exchanger also decreases with density according to the fan laws, shown in Equations 2-4 [12]. This reduction in static pressure rise can only be compensated for by increasing fan speed up to a tip Mach number of approximately 0.7 as compressibility effects above this speed dominate and reduce fan efficiency.

$$\dot{V}_{fan} \propto \omega_{fan} D_{fan}^3 \quad (2)$$

$$\Delta P_{fan} \propto \omega_{fan}^2 D_{fan}^2 \rho \quad (3)$$

$$\dot{W}_{fan} \propto \omega_{fan}^3 D_{fan}^5 \rho \quad (4)$$

Where $\dot{V}_{fan}, \omega_{fan}, D_{fan}, \Delta P_{fan}$, and $\dot{W}_{fan}$ are the fan volumetric flowrate, rotational speed, tip diameter, pressure rise, and power respectively, while ρ is the fluid density in which the fan is operating.

This system will operate in conditions well outside the norm for convective heat exchangers. The flow on the gas side is expected to have a Reynolds number of 10-300 for optimal geometries, indicating laminar flow, and a Knudsen number, defined as the ratio of the molecular mean free path and the geometrical length scale:

$$Kn = \frac{\mu}{\rho L}\sqrt{\frac{\pi M}{2k_B T}} \quad (5)$$

where μ is the dynamic viscosity, ρ is the fluid density, L is the length scale, M is the molecular mass of the fluid, and k_B is the Boltzmann constant, of approximately 0.01, which is on the boundary between continuum and slip flow. Due to the low speed of sound on Mars, the fan will also operate in the little-studied regime of low to moderate Reynolds, high tip Mach number, and high head coefficient. Additionally, due to operational thermal constraints and the density

dependence of the fan pressure rise shown in Equation 3 above, for optimal fan performance the fan will be placed upstream of the heat exchanger and thus the heat exchanger will experience highly-vortical inlet flow conditions. Experimentally measuring the performance of a heat exchanger in these conditions will therefore yield novel data for heat exchanger behavior in low Reynolds, high Knudsen number, vortical conditions that can be used to validate existing Nusselt number and Euler correlations or generate new ones. These correlations will be very useful for future Mars heat exchanger design efforts.

If it can be shown that a forced convection heat exchanger can effectively reject waste heat from a medium- to high-power FSPS to the Martian atmosphere with a total mass less than a comparable radiative heat rejection system, significant performance, simplicity, and cost benefits for a future Mars FSPS could be enabled. Employing a forced convection heat rejection system could then greatly reduce power system overall cost and deployment time and increase mission scientific payload and data collection. Additionally, such a system could be easily scalable to fulfill other heat rejection applications on Mars besides power generation, such as cryofuel liquefaction and refrigeration, rover cooling and habitat climate control.

To determine if forced-convection heat transfer offers a viable method of waste heat rejection on Mars, an analytical model of a heat exchanger has been developed using existing Nusselt number and Euler number correlations and the effective-NTU method of heat exchanger modelling. A geometry optimization algorithm was written to use the heat exchanger model to determine the minimum-mass heat exchanger design capable of meeting a specified heat rejection load. This optimizer was then used to create reduced order models for heat exchanger mass, conductance, and fan power based on a wide array of heat rejection loads for a given

ambient condition. These fits were used to integrate a simplified heat exchanger model into Sondelski's HTGR thermal cycle optimization code to determine the difference in overall system performance when using a convective heat exchanger compared to a radiator in Martian conditions, and to determine the optimal heat exchanger geometry for this application. The heat exchanger model and optimizer were both written in Julia [13], a high-performance open-source language well-suited for complex optimization problems.

A prototype heat exchanger based on the Mars-optimized design from the initial modelling effort has been constructed. An experimental facility, consisting of an open cycle wind tunnel within a vacuum chamber, is also constructed in order to operate the heat exchanger under a range of Reynolds number and Knudsen number conditions that are representative of operation in the Martian environment. The system is configurable to create both axial and vortical flows into the heat exchanger and capable of operating in a pure air or 98% CO2 composition. By collecting heat exchanger Nusselt number and Euler number data across the full range of these conditions, the existing correlations are validated against a novel dataset and new correlations are generated to more accurately model heat exchanger performance in these conditions. The heat exchanger model is then updated to incorporate the new correlations to generate experimentally-validated predictions of heat exchanger mass and geometry for Martian surface applications, as well as updated FSPS cycle optimization results.

Liquid Oxygen cryocooling represents another potentially useful application of forced convection waste heat rejection on Mars. The in-situ production and storage of rocket propellants and oxidizer could enable significantly more down-mass capability or shorter trip times on future Mars missions by obviating the need to bring fuel for the return journey from

Earth. Once the Oxygen and/or fuel are isolated from the in-situ resources, a cryocooler is required to liquefy them for efficient storage and eventual use in a launch vehicle. The cryocooler will require high rates of heat transfer to the environment. Due to the thermodynamics of the cryocooling cycle, the total power required to obtain a certain cooling rate is dependent on the heat rejection temperature, therefore the use of a convective heat exchanger may reduce the system mass by reducing the optimal heat rejection temperature. To study this application, a cryocooler model and optimizer were written in Julia to examine the performance benefit of using a convective heat rejection system for this application.

1.2 Literature Review

1.2.1 Fission Surface Power

Fission surface power system development has undergone multiple periods of activity and inactivity over the last 40 years. The SP-100 program was initiated in 1986 and aimed to develop a reactor power system in the 10-1000 kW_e range [14]. An architecture using a liquid-metal-cooled fast reactor coupled with a closed Brayton cycle power conversion system was found to be optimal for the 20-100 kW_e range. The main application of this program was for high-power Earth-orbit satellites as part of the Strategic Defense Initiative, although NASA missions to the outer planets using electric propulsion were also considered. As it was intended for use in dep space, this power system necessarily used a radiator for waste heat rejection. Although no flight hardware or nuclear systems were built, the design study provided significant technology heritage and influenced the design of future space power programs. In particular, the SP-100 design was investigated by Mason [15] as a power source to meet the requirements of NASA's

1997 Mars Design Reference Mission. The surface power system was required to produce 160 kW_e and autonomously position and deploy itself far away from the crew lander. A recuperated Brayton cycle was selected for this system over Stirling, Rankine, or thermoelectric conversion due to the former's low weight, demonstrated technological readiness, and the potential to be directly coupled to a gas-cooled reactor. A trade study was conducted comparing a liquid-metal-cooled reactor based on the SP-100 and a gas-cooled reactor (GCR) based on an earlier study by Pratt & Whitney of such a system called ESCORT [16]. As the heritage for both systems lay in space-based designs, a radiator was the only considered heat rejection system for both cases. The directly-coupled GCR-Brayton was determined to provide the highest performance, massing 12 tons with a radiator area of 285 m^2.

NASA's next fission surface power development project in collaboration with LANL, fittingly called the Fission Surface Power (FSP) project, began in 2006, aimed to develop a 40 kW_e system suitable for both lunar and Mars missions. Based on previous experience and the desire to produce a high-TRL design, the chosen architecture was a highly-enriched UO_2-fueled, pumped-NaK cooled fast reactor with Stirling conversion and a pumped-water radiator for heat rejection, with a peak coolant temperature of 900 K [17]. Figure 3 illustrates this concept. Beryllium radial reflectors are used to control reactivity instead of control rods and the core consists of a bundle of 316SS-clad fuel pins. To reduce shielding mass, the reactor core would be buried 2 m below grade and the converters and radiator panels would extend from a truss above the core.

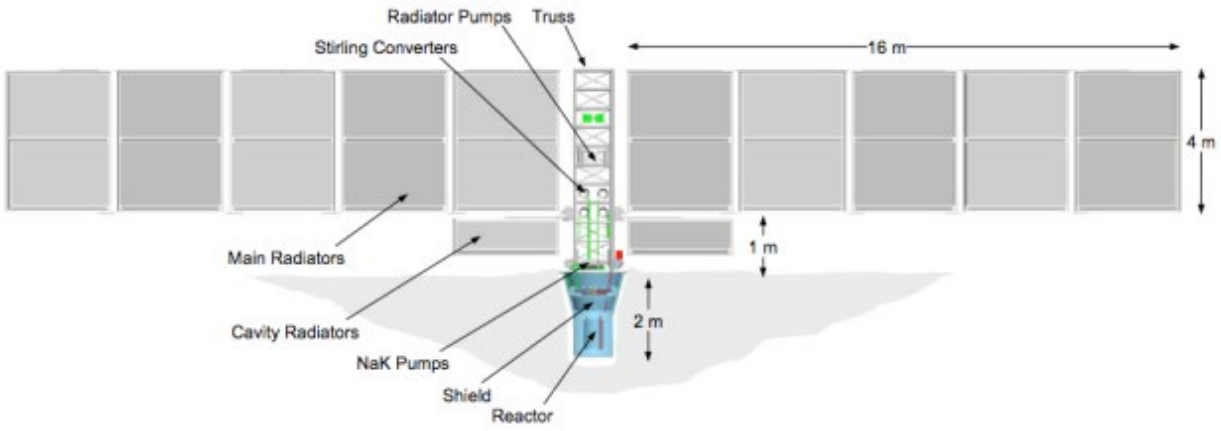

Figure 3: An illustration of the FSP concept. Deployable radiators were to be mounted on trusses above a buried reactor. From Mason et al. [14]

Significant risk-reduction of ancillary system components was achieved through the successful demonstration of the power conversion system, radiator, and NaK pump systems, however no criticality tests were carried out.

Significant development has taken place recently on the KiloPower reactor, a NASA program to develop a 10 kW_e FSPS for lunar and Mars missions [18]. The KiloPower reactor design features a monolithic highly-enriched Uranium (HEU) Molybdenum core surrounded by a BeO reflector and controlled via a single B_4C control rod, Sodium heat pipes brazed to the core to provide heat transfer coupled with Stirling engines for power generation, and a deployable radiator for waste heat rejection. The entire system mass not including shielding is estimated to be 1500 kg and 4 units would be required to meet the reference mission power needs, and could do so for 10 years. Significantly, a scaled-down version of KiloPower has been tested at the Nevada National Security Site in 2018, generating 4 kW_t from nuclear fission at a core

temperature of 800°C and using this heat to run the Stirling engines, representing the first critical test of an American space reactor since the 1960s [19].

1.2.2 Mars Forced Convection

Comparatively very little research has been conducted into natural- and forced-convection heat rejection systems for use on Mars. Von Arx and Delgado [20] examined the feasibility of convective waste heat rejection for a Brayton cycle-cooled 2.5 kW_e RPS on Mars compared to thermal radiation and determined that a radiator produced a lower-mass system, but the design of the forced-convection system studied was very non-optimal, consisting of a finned heat sink coupled to a fan and fan shroud. More recently, in 2015 Creare LLC was awarded a Phase I SBIR grant to study a forced-convection-based compact heat rejection system for Mars FSP [21]. Their design consisted of a high-speed axial flow fan and compact micro-tube heat exchanger. For a 3 kW_e Brayton system, their modelling suggested a mass reduction of 90 kg and a more compact overall system design by using forced-convection heat rejection, however no experimental study of the heat exchanger performance was carried out. The proposal was not selected for further study and no other studies of forced-convection heat rejection on Mars have been found in the literature.

1.2.3 Existing Euler Number and Nusselt Number Correlations

The Reynolds number within a Mars-optimized heat exchanger are expected to be quite low, on the order of 10-100. While numerous studies found in the literature examine the Nusselt number and Euler number associated with flow over a tube bank at low Reynolds number [22] [23] [24], none were found that experimentally validated these correlations in rarefied gases that

are similar to the Martian environment and therefore no data are available at relevant Knudsen numbers. The only study found that experimentally tested a heat exchanger in a low pressure environment is by Jia et al. [25] who studied a plate-fin heat exchanger and collected data only above 60 kPa absolute pressure. To obtain a similar Knudsen number in standard, atmospheric pressure air, a tube or wire diameter of approximately 10 μm would be required and no experimental works of this kind were found. Xie et al. [26] developed a Nusselt number correlation for a single cylinder in crossflow at Knudsen numbers ranging from 0.0045 to 1.31 by measuring the heat transfer rate associated with a 20 μm wire in rarefied gas at pressures ranging from 0.1 to 100 kPa and at Reynolds numbers below 20. They found that below a Knudsen number of 0.01, indicating continuum flow, Nusselt number was weakly correlated to Knudsen number. However from 0.01 to 0.1, in the slip flow regime, the Nusselt number was more strongly negatively impacted by increasing Knudsen number. However, while the first row of a tube bank can be approximated as isolated tubes for the Reynolds number range of interest here [22], this same approximation could only be made for subsequent rows for Reynolds numbers low enough to not induce flow separation, around $Re = 5$ [27]. Peles et al. [28] studied forced convection heat transfer and pressure drop in water flows across a deep bank of cylindrical pins on a micro heat sink. While the geometry and test conditions vary greatly from the present study, for a Reynolds number of 10-1000, Knudsen number of .001-.005, and a pitch-to-diameter ratio of 1.5, the authors found reasonable agreement with their experimental data using the Zukauskas [22] correlation for Nusselt number and with the correlation given in the *Heat Exchanger Design Handbook* [29] (referred to throughout this work as the HEDH correlation) for the pressure drop, though a negative deviation from the predicted Nusselt number is noted at

higher heat fluxes. The authors do not present their own correlation to fit the data. Tariq et al. [30] developed a Nusselt number correlation based on a numerical study of porous media, modelled as a repeating pattern of staggered cylinders of varying porosity. This model predicts a slight dependence on Knudsen number in the range of interest and is the only work found to model the relevant Reynolds number, Knudsen number, and tube spacing.

The pressure drop and heat transfer effects of swirling flow at the tube bundle inlet are of interest to designers of air-cooled heat exchangers for large-scale heat rejection applications. The forced-draft design, in which the fan forces air through the tube bundle from the upstream side, allows for easier maintenance, higher fan efficiency, and lower exit velocities. Moore et al. [31] experimentally studied the pressure drop and heat transfer of a forced-draft and induced-draft (in which the fan is situated downstream of the tube bundle) air-cooled heat exchanger tube bundle using 4 and 6 rows of finned tubes at a Reynolds number of approximately 3000-20000 and found that the forced-draft case resulted in an increase of approximately 30% in the friction factor but negligible increase in the dimensionless heat transfer, but did not provide a correlation of this deviation with the fan speed. The authors suggest the increased pressure drop results from flow separation from the fins. Gianoli and Cuti [32] suggest this increased pressure drop should be cancelled out by pressure recovery as the radial component of the velocity straightens through the tube bundle. However the conditions and geometry studied by the authors differs greatly from the present work, which examines bare tubes in laminar conditions. As most work in this field focuses on large air coolers in ambient pressure air [31] [32] [33], no studies could be found in the literature examining vortical inlet condition effects on tube bundle performance at low Reynolds numbers or moderate Knudsen numbers.

In summary, no studies of swirling, vortical flow through staggered bare tube banks could be found in the literature. Neither could any experimental data collected on staggered tube bank arrays for heat transfer or pressure drop in low pressure forced convection be found, nor cylindrical tube bank heat transfer or pressure drop data in Knudsen numbers of 0.005-0.01 and low Reynolds numbers. The experimental work described in this paper generates novel data on tube bank heat transfer and pressure drop in low Reynolds number, moderate Knudsen number, and axial and vortical flows. The data will be vital to benchmark and facilitate future modelling efforts to design heat rejection systems for use on Mars or at high altitudes on Earth.

1.2.4 Mars Wind Tunnel Design

The experimental data collection proposed in this work will require the construction of a low-pressure test section in which a 12 m/s flow speed and 14 Pa of pressure drop at a static pressure of approximately 800 Pa can be both generated and accurately measured. To measure the flow rate accurately, an enclosed flow channel containing the heat exchanger, fan, and flow sensor, effectively a low-pressure wind tunnel, must be built. In 1981 NASA built the Mars Surface Wind Tunnel (MARSWIT) facility, an open-circuit 1 m^2 cross section wind tunnel capable of producing wind speeds up to 180 m/s using a high-pressure nozzle ejector system [34]. A smaller-scale version of this design was built at the University of Washington. CO_2 from a bottle is passed through an orifice plate to regulate and measure the flowrate, then through a refrigerated test section to mimic Martian surface temperatures. A vacuum pump expels the CO_2 from the chamber to maintain the target pressure. For both systems, flow rate is determined by measuring the mass flow rate of the gas being injected into the test section. However, it is desired to also investigate the effect of the fan-induced vorticity on the heat exchanger performance, so a fan-

driven wind tunnel design is required. Merrison et al. [35] constructed a closed-circuit fan-driven wind tunnel at Aarhus University to study dust transport which uses an external fan drive magnetically-coupled to an internal fan to provide flow without complicated seals or a vacuum-rated motor. They use a laser anemometer for flow velocity measurement and a cryogenic cooling system to reproduce typical Mars conditions. Veismann et al. [36] constructed a wind tunnel using a large bank of off-the-shelf axial cooling fans to test Mars helicopter flight dynamics. The fan array was constructed within a 25 foot diameter vacuum chamber to reproduce Martian conditions and the fans were capable of producing 12 m/s flow velocities in 1000 Pa air. A Pitot tube was used for measuring the flow velocity. A flow straightener was mounted flush to the fans to improve flow uniformity.

2. Modelling

2.1 Analytical Heat Exchanger Model

2.1.1 Modelling Geometry and Approach Overview

The heat exchanger geometry considered for this project is a once-through, plate-finned circular tube crossflow heat exchanger, illustrated in Figure 4. This design was chosen because it offers a good compromise between high conductance in a compact design and relatively low gas-side pressure loss, both desirable traits in the Martian environment due to the low atmospheric density. Additionally, while design enhancements such as airfoil-shaped tubes, alternative fin geometries, and a twice-through high-pressure fluid path may provide a performance benefit, circular tubes are widely available over a range of sizes and the once-through high-pressure fluid path simplifies the construction of the experimental prototype. Several geometric parameters

were investigated such as the tube pitch to diameter ratio and the use of a staggered vs in-line tube arrangement. In the staggered arrangement, the tubes are arranged equilaterally so that the minimum separation between adjacent tubes in the same column and in adjacent columns is the same. In this case the lateral column separation is $\sqrt{3}/2$ times the tube pitch. Figure 5 illustrates the two tube arrangements, where D_t is the tube diameter, R_p is the pitch to diameter ratio, S_T is the transverse tube pitch, S_L is the lateral tube pitch, and A_{min} is the minimum flow area between adjacent tubes.

Five candidate heat exchanger materials were also considered: 316 Stainless Steel, 6061 Aluminum, Copper, Titanium, and 740H Inconel. Two working fluids were considered: sCO_2 and Helium. The fins are modelled as 0.1 mm thick sheets of the same material as the tubes. The fin efficiency is approximated as being 100% due to the small tube pitch that results from the optimization and the low surface heat transfer coefficient; therefore the fin surface temperature is assumed to equal the tube surface temperature.

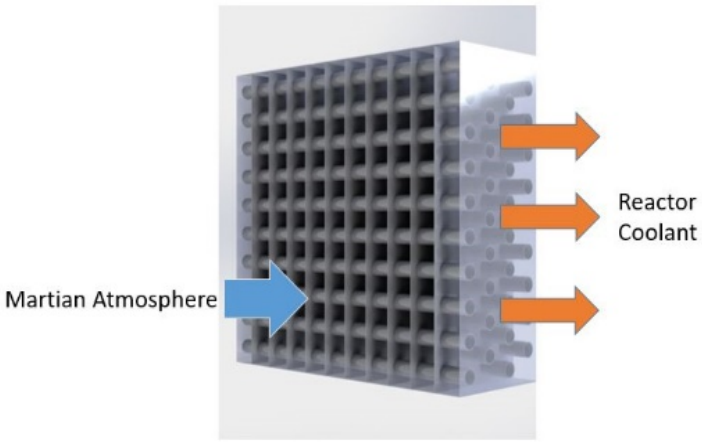

Figure 4: Illustration of the crossflow heat exchanger type modelled in this work

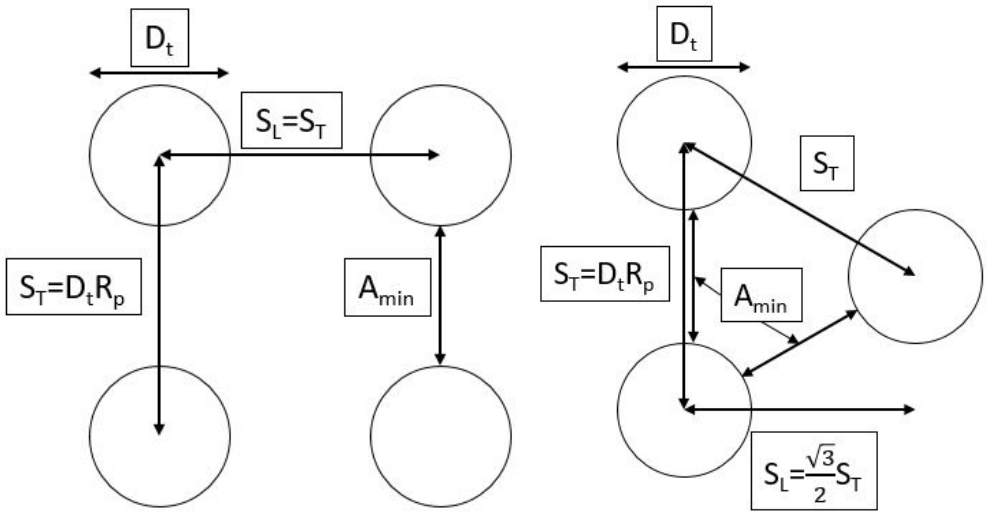

(a) (b)

Figure 5: Diagram of the (a) in-line and (b) staggered tube arrangements

Dust can be present in the Martian atmosphere during dust storms; however, the effect of dust on the heat exchanger performance was neglected here. Wind tunnel experiments by Merrison et al. [37] demonstrate that wind speeds above 10-15 m/s, a typical range of the optimal flow speed through the heat exchanger, will cause dust removal to occur on flat plates in Martian conditions for all but the smallest dust particle sizes. While it is possible that dust may accumulate on the leeward side of the tubes on the fins or the tubes due to low local flow velocities there, this should not greatly affect the overall heat exchanger performance as most of the heat transfer will be occurring in the areas of high local velocity.

Figure 6 shows a flowchart illustrating the method that the model follows to determine the performance of a heat exchanger with a given geometry and the outer loop that is used to identify the optimal heat exchanger geometry.

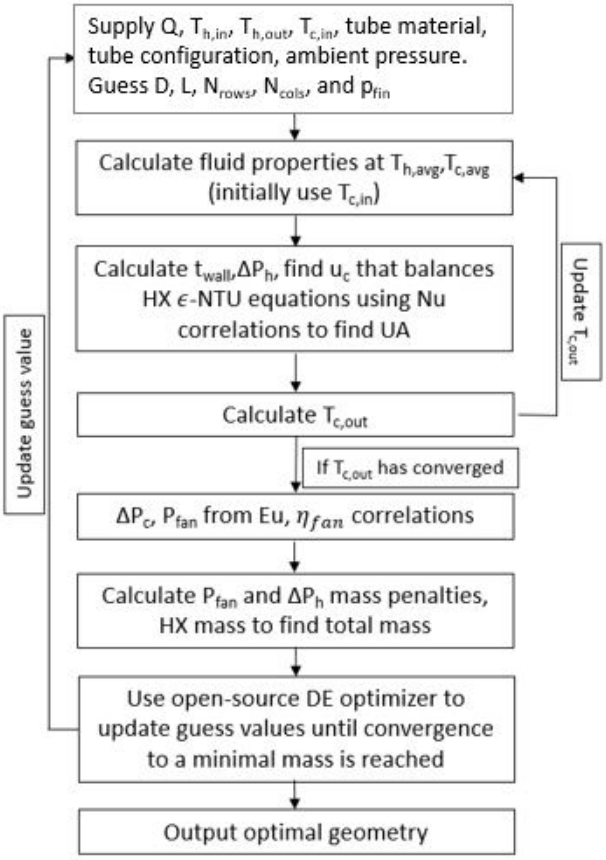

Figure 6: Heat exchanger modelling flowchart

2.1.2 Model Inputs

The model is supplied a set of heat rejection parameters, i.e. the rejected heat load $\dot{Q}$, the inlet and outlet coolant temperatures $T_{h,in}$ and $T_{h,out}$, the ambient atmospheric temperature $T_{c,in}$, the coolant (i.e., working fluid) pressure P_h, and the ambient pressure P_c, as well as a set of material and configuration parameters, i.e. the heat exchanger and coolant material and the tube arrangement and R_p, and a set of geometrical parameters, i.e. the number of tube rows and tube columns N_{rows} and N_{cols}, the tube diameter and length and L, and the fin pitch p_{fin}. The material and fluid properties are then determined based on the temperatures and pressures. The coolant specific heat, dynamic viscosity, density, and conductivity, denoted as

$c_{p,h}, \mu_h, \rho_h,$ and k_h respectively, are calculated at P_h and $\bar{T}_h$, the average of the inlet and outlet coolant temperature, and the wall density, conductivity, and yield stress, denoted as $\rho_{wall}, k_{wall},$ and S_y respectively, are calculated at $\bar{T}_h$. The atmosphere is modelled as pure CO_2 and the fluid properties $c_{p,c}, \mu_c, \rho_c,$ and k_c and calculated at P_c and $\bar{T}_c$, the average of the inlet and outlet gas-side temperature. Initially the inlet temperature $T_{c,in}$ is used to determine atmospheric properties as the outlet temperature $T_{c,out}$ is unknown. CO_2 and He properties are determined using the Julia package CoolProp, which determines fluid properties based on Helmholtz energy formulations of the equations of state [38]. Heat exchanger material properties are determined via property table interpolation.

2.1.3 Velocity Calculation

To calculate the airflow velocity required to dissipate the rejected heat load, the effectiveness-NTU method is used. First, the coolant mass flowrate, $\dot{m}_h$, is determined as follows:

$$\dot{m}_h = \frac{\dot{Q}_{HX}}{c_{p,h}\left(T_{h,in} - T_{h,out}\right)} \quad (6)$$

where $\dot{Q}_{HX}$ is the rate of heat rejection from the heat exchanger. Next the tube wall thickness, t_{wall}, is determined based on the hoop stress and a $MOS = 0.25$ factor of safety:

$$t_{wall} = \frac{D_t P_h}{2\left(\frac{S_y}{1 + MOS} + P_h\right)} \quad (7)$$

where D_t is the tube diameter and S_y is the yield stress of the tube material. For the purpose of constraining the optimization model, the wall thickness is limited to a minimum of 0.05 mm. The maximum Reynolds number of the gas-side flow, occurring at the narrowest gap between adjacent tubes, is determined as

$$Re_t = \frac{\rho_c u_{max} D_t}{\mu_c} = \frac{\rho_c R_p u_c D_t}{\mu_c (R_p - 1)} \quad (8)$$

for both the staggered and in-line arrangements, where R_p is the pitch-to-diameter ratio, u_c is the frontal atmospheric gas velocity at the heat exchanger inlet and u_{max} is the maximum gas velocity in the heat exchanger, or the gas velocity at the minimum flow area between adjacent tubes, A_{min}. u_c is not known explicitly but will be solved for to find a solution to the effectiveness-NTU method. To determine the average Nusselt number for the finned-tube array, the tube surfaces and fin surfaces are treated separately and the results are superposed, as suggested by Rich [39]. This process is used because no existing correlations for plate-finned tube array Nusselt number at relevant Reynolds numbers were found in the literature. This technique is also applied to correlations for the Euler number, defined as

$$Eu = \frac{2\Delta P_{row}}{\rho u_{max}^2} \quad (9)$$

where ΔP_{row} is the pressure drop across a single row, when determining pressure drop, also as suggested by Rich. To determine the Nusselt number of the tube array, the correlation developed by Tariq et al. [30] is used. The correlation is slightly modified to incorporate the entry length

effects estimations from Zukauskas and Ulinskas [40] as the Tariq et al. correlation was based on an infinite repeating array of cylinders in crossflow. The modified Tariq et al. correlation is given as

$$\overline{Nu} = k_1 \frac{\left(.48 - .2\epsilon_{por}\right)\left(\frac{\epsilon_{por}}{1-\epsilon_{por}}\right)\ln(Re_t)^{c_1}\, Pr}{1 + 0.1\ln(Re_t)^{c_2}\, Kn};$$

$$c_1 = 3.12 - 0.16e^{3\epsilon_{por}}; c_2 = 3.45 - 3e^{-3.45\epsilon_{por}}$$

(10)

where k_1 is the entry length correction factor, ϵ is the tube bundle porosity, i.e. the ratio of the tube cross-sectional area to the total cross-sectional area, and Pr is the Prandtl number. The fin Nusselt number approximates the fins as the walls of a rectangular duct, where the length of the duct is the overall depth of the heat exchanger in the airflow direction, the width is the fin pitch, and the height is the overall heat exchanger height. The thermal boundary layer thickness of a flat plate in laminar flow, $\delta_{t,lam}$, is given in Nellis and Klein [41] as

$$\delta_{t,lam} = \frac{4.916x}{\sqrt{Re_x}} Pr^{-\frac{1}{3}}$$

(11)

where Re_x is the Reynolds number considering the axial distance from the front edge of the plate. Until the boundary layers from adjacent fins intersect, the fins are treated as independent flat plates, and the average Nusselt number for laminar flow is

$$\overline{Nu}_{fp,lam} = \frac{\bar{h}_{fp,lam} L_{fin}}{k_c} = \frac{0.6774 Re_{x_{fd,lam}}^{0.5} Pr^{\frac{1}{3}}}{\left(1 + \left(\frac{0.0468}{\mathrm{Pr}}\right)^{\frac{2}{3}}\right)^{0.25}}$$

(12)

while for turbulent flow the average Nusselt number is

$$\overline{Nu}_{fp,turb} = \frac{0.6774 Re_{crit}^{.5} Pr^{\frac{1}{3}}}{\left(1 + \left(\frac{0.0468}{\mathrm{Pr}}\right)^{\frac{2}{3}}\right)^{.25}} + 0.037 Pr^{\frac{1}{3}} \left(Re_{x_{fd},turb}^{0.8} - Re_{crit}^{0.8}\right)$$

(13)

where $Re_{x_{fd,lam}}$ is the Reynolds number evaluated using the minimum of the fin length and the laminar developing length, $Re_{x_{fd,turb}}$ is the Reynolds number evaluated using the minimum of the fin length and the turbulent developing length, and Re_{crit} is the Reynolds number at which the flow along the plate becomes turbulent, defined as 5x10^5, $\bar{h}$ is the average heat transfer coefficient, and k_c is the atmosphere thermal conductivity. L_{fin}, the length of the duct formed by the fins, is

$$L_{fin} = D_t R_p N_{cols} k_{config}$$

(14)

where k_{config}, the configuration factor, is the lateral pitch-to-diameter ratio that depends on if the tube array is staggered or inline and equals

$$k_{config} = \begin{cases} \frac{\sqrt{3}}{2}; stagered\ array \\ 1; \qquad inline\ array \end{cases}$$

(15)

Once the boundary layers intersect, the plates act as a rectangular, and so the average Nusselt number in this regime for laminar flow, assuming constant heat flux along the fin, is

$$\overline{Nu}_{duct,lam} = \frac{\bar{h}_{duct,lam} D_{h,duct}}{k_c} = 8.235; D_{h,duct} = \frac{2H(p_{fin} - t_{fin})}{H + p_{fin} - t_{fin}}$$

(16)

where $D_{h,duct}$ is the hydraulic diameter of the duct, p_{fin} and t_{fin} are the fin pitch and thickness respectively, and H, the total height of the heat exchanger, is

$$H = D_t R_p N_{rows}.$$

(17)

For turbulent duct flow the Nusselt number is

$$\overline{Nu}_{duct,turb} = \left(\frac{f_{fd}}{8}\right) \frac{(Re_{D_h} - 1000)Pr}{1 + 12.7\left(Pr^{\frac{2}{3}} - 1\right)\sqrt{\frac{f_{fd}}{8}}}$$

(18)

where f_{fd} is the fully-developed friction factor. Turbulent duct flow is assumed to occur at hydraulic Reynolds numbers greater than 2300. The distance at which the boundary layers intersect, i.e. when the boundary layer grows to half the fin gap, is

$$x_{fd,lam} = \left(\frac{(p_{fin} - t_{fin})}{2} \frac{Pr^{\frac{1}{3}}}{4.916} \right)^2 \left(\frac{\rho_c u_c}{\mu_c} \right)$$

(19)

$$x_{fd,turb} = \left(\frac{p_{fin} - t_{fin}}{0.32} \left(\frac{\rho_c u_c}{\mu_c} \right)^{\frac{1}{7}} \right)^{\frac{7}{6}}$$

(20)

The Nusselt numbers for the developing and fully-developed regions are defined on different length scales, so to determine the average Nusselt number for the fins when fully-developed flow occurs, the average heat transfer coefficient is determined by area-averaging the developing and fully-developed heat transfer coefficient, as shown below.

$$\bar{h}_{fin} = \frac{\bar{h}_{fp} x_{fd} + \bar{h}_{duct} \left(L_{fin} - x_{fd} \right)}{L_{fin}}$$

(21)

By substituting in the definitions of the developing and fully-developed Nusselt numbers, this becomes

$$\bar{h}_{fin} = \frac{\frac{\overline{Nu}_{fp} k_c}{x_{fd}} \, x_{fd} + \frac{\overline{Nu}_{duct} k_c}{D_h} \left(L_{fin} - x_{fd} \right)}{L_{fin}}$$

(22)

and this expression can be simplified to

$$\bar{h}_{fin} = \frac{k_c}{L_{fin}}\left(\overline{Nu}_{fp} + \overline{Nu}_{duct}\frac{\left(L_{fin} - x_{fd}\right)}{D_h}\right).$$

(23)

Therefore the average fin Nusselt number can be expressed as

$$\overline{Nu}_{fin} = \frac{\overline{h_{fin}}L_{fin}}{k_c} = \begin{cases} \overline{Nu}_{fp}, & L < x_{fd} \\ \overline{Nu}_{fp} + \dfrac{\left(L_{fin} - x_{fd}\right)}{D_h}\,\overline{Nu}_{duct}, & L \geq x_{fd} \end{cases}$$

(24)

The total thermal resistance in the heat exchanger due to convection on the gas side is then

$$R_{out} = \frac{1}{\bar{h}_t A_t + \bar{h}_{fin} A_{fin}}$$

(25)

where A_t and A_f are the total surface areas of the tubes and the fins.

Next the thermal resistance between the coolant and the tubes is calculated. The coolant Reynolds number is calculated as

$$Re_h = \frac{4\dot{m}_h}{\pi D_{t,in}\mu_h N_{rows} N_{cols}}$$

(26)

where $\dot{m}_h$ is the mass flow rate of the high-pressure fluid and $D_{t,in}$, the tube internal diameter, is

$$D_{t,in} = D_t - 2t_{wall}.$$

(27)

The Nusselt number correlations for fully-developed internal flow in a smooth circular duct with constant heat flux are given in Nellis and Klein [41] as:

$$\overline{Nu_h} = \begin{cases} 4.36, & Re_h < 2300 \\ \dfrac{\frac{f_{t,turb}}{8}(Re_h - 1000)Pr_h}{1 + 12.7\left(Pr^{\frac{2}{3}} - 1\right)\sqrt{\frac{f_{fd,turb}}{8}}}\left[1 + \left(\dfrac{L}{D_{t,in}}\right)^{-0.7}\right]; & Re_h \geq 2300 \end{cases}$$

(28)

where $f_{t,turb}$, the fully developed turbulent friction factor for a smooth tube, is given by Zigrang and Sylvester [42] as

$$f_{t,turb} = \left(-2\log_{10}\left(\frac{2e}{7.54D_{t,in}} - \frac{5.02}{Re_h}\log_{10}\left(\frac{2e}{7.54D_{t,in}} + \frac{13}{Re_h}\right)\right)\right)^{-2}$$

(29)

The fully-developed assumption is reasonable as the dimensionless length, defined as

$$L^+ = \frac{L_t}{D_h Re_h}$$

(30)

is greater than 0.1 for all optimized heat exchanger geometries. The assumption of smooth internal walls is reasonable because, using a typical RMS roughness value for stainless steel seamless tubing of 0.015 mm, the smooth tube and rough tube friction factors differ by less than 4% for a 0.5 mm diameter tube. The total thermal resistance between the coolant and the tubes is then

$$R_{in} = \frac{1}{\bar{h}_h \pi D_{t,in} L N_{rows} N_{cols}}$$

(31)

where $\bar{h}_h$, the heat transfer coefficient between the coolant and tube wall, is derived from $\overline{Nu_h}$. The thermal resistance from conduction through the tube walls is

$$R_{cond} = \frac{\log\left(\frac{D_t}{D_{t,in}}\right)}{2k_{wall}\pi L N_{rows} N_{cols}}$$

(32)

and the fouling resistance on the inner wall of the tubes is approximated as the following, based on tubular heat exchanger design standards [43]:

$$R_{foul} = \frac{R"_{foul}}{\pi D_{t,in} L N_{rows} N_{cols}}; R"_{foul} = 0.000176 \frac{Km^2}{W}$$

(33)

The total conductance of the heat exchanger is therefore

$$UA = \frac{1}{R_{in} + R_{foul} + R_{cond} + R_{out}}$$

(34)

the gas-side capacitance rate of the system is

$$\dot{C}_c = \dot{m}_c c_{p,c}$$

(35)

where $c_{p,c}$ is the gas-side specific heat capacity, and $\dot{m}_c$, the gas-side mass flow rate, is determined by the frontal velocity, density, and total frontal flow area:

$$\dot{m}_c = \rho_c \dot{V}_c \tag{36}$$

$$\dot{V}_c = u_c(N_{fins} - 1)\big(p_{fin} - t_{fin}\big)H \tag{37}$$

where N_{fins}, the number of fins in the heat exchanger, is

$$N_{fins} = \frac{L_t}{p_{fin}} + 1. \tag{38}$$

Therefore, the gas-side capacitance rate can be simplified to

$$\dot{C}_c = \rho_c u_c L\left(1 - \frac{t_{fin}}{p_{fin}}\right) H c_{p,c} \tag{39}$$

and the coolant capacitance rate is

$$\dot{C}_h = \dot{m}_h c_{p,h} \tag{40}$$

When the fin pitch is small relative to the tube length, the heat exchanger is classified as a crossflow, both sides unmixed heat exchanger, but when the fin pitch close to the tube length, i.e. there are few or no fins in the heat exchanger, it is a crossflow, one side unmixed heat exchanger, so the effectiveness is

$$\epsilon_{HX} = \begin{cases} 1 - \exp\left(-\dfrac{1 - exp\left(-\dot{C}_R NTU\right)}{\dot{C}_R}\right), & p_{fin} \cong L_t, \quad \dot{C}_c < \dot{C}_h \\ \dfrac{\left(1 - \exp\left(\dot{C}_R\, exp(-NTU) - 1\right)\right)}{\dot{C}_R}, & p_{fin} \cong L_t, \quad \dot{C}_c \geq \dot{C}_h \\ 1 - \exp\left[\dfrac{NTU^{0.22}}{\dot{C}_R}\{exp(-C_R NTU^{0.78}) - 1\}\right], & p_{fin} \ll L_t \end{cases}$$

(41)

where NTU, the number of transfer units, is defined as

$$NTU = \frac{UA}{\dot{C}_{min}}; \dot{C}_{min} = \min\left(\dot{C}_c, \dot{C}_h\right)$$

(42)

and $\dot{C}_R$, the capacitance ratio, is

$$\dot{C}_R = \frac{\dot{C}_{min}}{\dot{C}_{max}};\ \dot{C}_{max} = \max\left(\dot{C}_c, \dot{C}_h\right).$$

(43)

To determine the atmospheric gas velocity that satisfies this system of equations, a function of the velocity, *find_u(u)*, was written encapsulating the above equations that returns the error value when solving the effectiveness-NTU equations for a set of guess values.

$$err_u = \frac{\dot{Q}_{HX}}{\epsilon_{HX}} - \dot{C}_{\min}\left(T_{h,in} - T_{c,in}\right).$$

(44)

As this value will be zero when the heat exchanger equations are balanced, finding the root of this function yields the gas velocity for these conditions. The outlet temperature can now be calculated as

$$T_{c,out} = T_{c,in} + \frac{\dot{Q}_{HX}}{\rho_c u_c L_t \left(1 - \frac{t_{fin}}{p_{fin}}\right) D_t R_p N_{rows}}$$

(45)

The fluid properties are then re-calculated using this new value for the outlet temperature and the above steps are iterated until the resulting velocity converges.

2.1.4 Pressure Drop Calculation

Once the gas side flow rate has been determined, the pressure drop and required fan power can be calculated. The fin pressure drop is calculated in a manner that is similar to the fin heat transfer by treating the developing region as separate flat plates and the fully-developed region as a rectangular duct, with laminar and turbulent friction factor correlations for both taken from Nellis and Klein [41].

As the CO_2 travels through the heat exchanger, it will become hotter after each tube column, thus the density will decrease and velocity will increase to conserve mass flow rate. The pressure drop per tube row increases with the square of the gas velocity for a given Euler number, as shown in Equation 9. Therefore, in order to determine the total pressure drop, first the CO_2 temperature before each tube column is calculated, from which the velocity at each column can be calculated from the pressure and flow rate. As the fan power is a significant driver of the total system mass, the optimal geometries will tend to have fairly high heat exchanger effectiveness and thus a large temperature rise from the inlet to the outlet of the cold side so this correction is necessary to calculate the pressure drop.

A full 2D modelling approach to calculate the average CO_2 temperature at each column was not deemed practical as the heat exchanger model needs to run quickly enough to solve the six-parameter geometry optimization model on the limited computing resources available. Therefore for the following analytical approach, the CO_2 temperature was approximated as only varying one-dimensionally through the heat exchanger and following the form

$$T_{c,i} - T_{c,i-1} = C_1(T_{h,in} - T_{c,i})$$

(46)

where $T_{c,i}$ is the cold side temperature after the i[th] column. C_1 is an unknown constant meant to capture the coupling of cold side per-column temperature rise and the coolant inlet temperature and is solved for by applying the boundary conditions of

$$T_{c,0} = T_{c,in}$$

(47)

and

$$T_{c,N_{cols}} = T_{c,in} + \frac{\dot{Q}_{HX}}{\dot{m}_c c_{p,c}}$$

(48)

which results from energy conservation and the approximation of constant specific heat capacity in the CO_2. Treating the cold side temperature as a continuous function, solving this ODE will yield an expression for the temperature of the form:

$$T_c(i) = T_{h,in} - C_2 \exp(-C_1 i)$$

(49)

Applying the boundary conditions of the known inlet and outlet temperature yield expressions for the constants:

$$T_c(0) = T_{c,in} = T_{h,in} - C_2; C_2 = T_{h,in} - T_{c,in}$$

(50)

$$T_c(N_{cols}) = T_{c,in} + \frac{\dot{Q}}{\dot{m}_c cp_c} = T_{h,in} - \left(T_{h,in} - T_{c,in}\right)\exp(-C_1 N_{cols})$$

(51)

$$C_1 = -\frac{1}{N_{cols}}\ln\left(\frac{\left(T_{h,in} - \left(T_{c,in} + \frac{\dot{Q}}{\dot{m}_c cp_c}\right)\right)}{T_{h,in} - T_{c,in}}\right)$$

(52)

Thus the approximation for the cold side temperature at the inlet of the ith tube column is

$$T_{c,i} = T_{h,in} - \left(T_{h,in} - T_{c,in}\right)\exp\left(\frac{i}{N_{cols}} ln\left(\frac{\left(T_{h,in} - \left(T_{c,in} + \frac{\dot{Q}_{HX}}{\dot{m}_c c_{p,c}}\right)\right)}{T_{h,in} - T_{c,in}}\right)\right)$$

(53)

Once the Euler number is predicted based on the correlations, the total pressure loss from the tube array can be calculated by summing the pressure loss from each tube column. The correlations for Eu from the *Heat Exchanger Design Handbook* [29], which are given for in-line and staggered arrays and R_P of 1.25, 1.5 and 2 for Reynolds number above 7 and include a correction for entry effects required by the small number of tube columns, are used to determine

the pressure drop resulting from the tube bank across each tube column. The HEDH correlation is given as

$$Eu_{HEDH} = k_2 k_3 \sum_{i=0}^{4} \frac{C_i}{Re_t^i}; k_2 = \left(\frac{Pr_{wall}}{Pr}\right)^{0.776\exp(-0.545 Re_t^{0.256})}; k_3 = entry\ length\ effects \quad (54)$$

where Pr_{wall} is the Prandtl number at the tube wall temperature. A modification to the HEDH correlation based on experimental data, described in Section 4 below, is proposed in this work and applied to the final version of the heat exchanger model.

The fin pressure drop is calculated similarly to the fins heat transfer by treating the developing region as separate flat plates and the fully-developed region as a rectangular duct, with laminar and turbulent friction factor correlations for both from Nellis and Klein [41]. These values are summed to determine the total pressure drop, as proposed by Rich [39].

2.1.5 Fan Model

The pressure drop is correlated to the fan speed, and the fan pressure rise is determined by the fan speed (as described in this system). A system of equations is set up to determine the fan speed and resulting expected pressure drop through the heat exchanger for a given flow rate and geometry. Quin and Grimes. [44] experimentally studied the performance of an axial fan in low Reynolds number flows. The authors used a commercially available high head coefficient fan design, scaled down uniformly to a diameter of 6 mm to study microaxial fan performance and did not attempt to optimize the fan design for the low-Reynolds conditions. While their data were collected in 1 bar air at a small length scale, the Reynolds number and Mach number of the fan

during testing roughly matched those expected of the fan that is required for a large Mars heat exchanger. The Reynolds number in this case is calculated using the mid-span velocity, u_{mid}, and the mid-span chord, L_{mid}, as the characteristic velocity and chord, i.e.

$$Re_{fan} = \frac{\rho_c u_{mid} L_{mid}}{\mu_c}$$

(55)

For this fan design, the authors determined the relationship between the dimensionless head coefficient and flow coefficient to be:

$$\psi = 0.307 - \left(2.3 + \frac{2860}{Re_{fan}}\phi^2\right)$$

(56)

where the head coefficient, ψ, and flow coefficient, ϕ, are defined as

$$\psi = \frac{\Delta P_{fan}}{\rho_c u_{mid}^2};\ \phi = \frac{\dot{V}_{fan}}{u_{mid} A_{fan}}$$

(57)

and where the fan flow area, A_{fan}, is

$$A_{fan} = \frac{\pi D_{fan}^2}{4}(1 - hub_{rat}^2).$$

(58)

hub_{rat}, the ratio of the fan hub to the fan blade tip diameter, is set to 0.3. The modelling in the current work assumes this same relationship between head and flow coefficient and also assumes that the mid-span chord equals the mid-span radius. Essentially the modelling assumes the same fan geometry as studied by Quin and Grimes. [44] The fan rotational speed that solves

the system of equations consisting of Equations 55, 56 and 57, and provides the required volumetric flow rate is determined iteratively using a root-finding algorithm.

The fan efficiency, defined as the ratio of the work imparted to the CO_2 by the fan to the work imparted to the fan by the motor, was determined based on Neustein's study of low-Reynolds-number axial fan efficiency [45]. The efficiency given by Neustein for fans operating at the optimal, i.e. most efficient, fan speed is:

$$\eta_{fan,Neu} = \begin{cases} \dfrac{Re_{fan}^{0.6987}}{404.64 + Re_{fan}^{0.6987}}; Re_{fan} < 20000 \\ \dfrac{Re_{fan}^{0.2917}}{7.187 + Re_{fan}^{0.2917}}; Re_{fan} > 20000 \end{cases}$$

(59)

However, Neustein did not investigate the combined effects of compressibility, i.e. high Mach number, in addition to low Reynolds number. As mentioned previously, this combination would be very unusual except in low-density environments so is not well-studied. Glauert [46] suggests that the effect of compressibility on fan efficiency takes the form

$$\eta_{fan} \propto \sqrt{1 - Ma_{fan}^2}$$

(60)

for fans in higher-Reynolds regimes, where Ma_f is the Mach number of the fan blade tip. This functional form is assumed in the present model as well. Therefore, the estimate for the fan efficiency is:

$$\eta_f = \sqrt{1 - Ma_{fan}^2} \begin{cases} \dfrac{Re_{fan}^{0.6987}}{404.64 + Re_{fan}^{0.6987}}; Re_{fan} < 20000 \\ \dfrac{Re_{fan}^{0.2917}}{7.187 + Re_{fan}^{0.2917}}; Re_{fan} > 20000 \end{cases}$$

(61)

The diameter of the fan is assumed to equal the smaller dimension of the heat exchanger frontal area, i.e. if the heat exchanger measures 1 m wide by 3 m high, the fan would have a diameter of 1 m and 3 fans would be stacked vertically to provide flow through the heat exchanger. This arrangement was chosen to maximize the fan size and thus increase the Reynolds number to reduce the effects of low Reynolds number fan operation. Finally, a motor efficiency, η_m, of 0.8 was also applied to determine the total electrical power required to drive the fan for a given geometry:

$$\dot{W}_{fan} = \frac{\dot{V}_{fan}\Delta P_{fan}}{\eta_{fan}\eta_m}$$

(62)

For mass modelling purposes, the fan is assumed to consist of aluminum blades with a thickness of $t_b = 1\ mm$ and a solidity factor, s_{fan}, of 1. More details regarding the computation of the fan mass is are included in the mass modelling section below.

2.1.6 Coolant Pressure Drop

The coolant pressure drop is estimated using the friction factor correlations given in Nellis and Klein for fully developed rough pipe flow. The coolant velocity is determined by the number of tubes, tube diameter, total dissipated heat and the coolant temperature drop as

$$u_h = \frac{4\dot{Q}_{HX}}{\pi D_{t,in}^2 N_{rows} N_{cols} \rho_h c_{p,h} \left(T_{h,in} - T_{h,out}\right)}$$

(63)

The coolant pressure drop is then:

$$\Delta P_h = \frac{\rho_h}{2} u_h^2 f_t \frac{L_t}{D_{t,in}}$$

(64)

where f_t, the friction factor, is:

$$f_t = \begin{cases} \frac{64}{Re_h}; & Re_h < 2000 \\ \left(-2\log_{10}\left(\frac{2e}{7.54D_{t,in}} - \frac{5.02}{Re_h}\log_{10}\left(\frac{2e}{7.54D_{t,in}} + \frac{13}{Re_h}\right)\right)\right)^{-2}; & Re_h > 2000 \end{cases}$$

(65)

The tube internal roughness, e, is estimated as 15 µm.

2.1.7 Total Mass

The total mass of the heat exchanger, including mass penalties to account for the power required to run the fan and the coolant pressure loss, can now be calculated. First the mass of the tubes is

$$m_t = \frac{N_{rows} N_{cols} L_t \pi \left(D_t^2 - D_{t,in}^2\right) \rho_{wall}}{4}$$

(66)

where ρ_{wall} is the density of the tube walls. The mass of the fins is:

$$m_{fin} = \left(1 + \frac{L_t}{p_{fin}}\right) A_{fin} t_{fin} \rho_{wall}$$

(67)

where A_{fin}, the per-fin surface area, is:

$$A_{fin} = \left(k_{config} R_p^2 - \frac{\pi}{4}\right) D_t^2 N_{rows} N_{cols}.$$

(68)

The heat exchanger header mass is estimated by approximating the header geometry as a tube of length equal to the heat exchanger overall height and diameter equal to the heat exchanger overall depth, i.e. $D_{head} = L_{fin}$, with a wall thickness based on the hoop stress Margin of Safety of 0.25.

$$m_{head} = 2H\rho_{wall} \frac{\pi}{4} \left(D_{head}^2 - \left(D_{head} - 2t_{wall,head}\right)^2\right)$$

(69)

where the header wall thickness, $t_{wall,head}$, has the same margin of safety as the tube walls:

$$t_{wall,head} = \frac{D_{head} P_h}{2\left(\frac{S_y}{1 + MOS} + P_h\right)}.$$

(70)

The mass of the fan includes several components. The fan blade mass is determined by the number of fans N_{fan}, fan area and the set blade thickness, density ρ_{blade}, and solidity factor:

$$m_b = N_{fan} A_{fan} \rho_b s_{fan} t_b$$

(71)

The mass of the fan motor is estimated from the required fan power and a value for the motor power-specific mass of $G_m = 5.75\ kg/kWe$, chosen to be representative of commercial high-performance electric motors.

$$m_m = \dot{W}_{fan} G_m$$

(72)

Finally, as the fan motor has an efficiency of 0.8, a non-negligible amount of heat will be generated by the fan. The mass of a cooling system required to maintain the motor temperature at an acceptable value is estimated by assuming the fan waste heat is channeled into tubes situated in parallel to the main coolant tubes in the heat exchanger and that they have the same geometry and experience the same heat flux as the main coolant tubes. Thus the cooling system simply scales up the mass of the heat exchanger tube array, fins, and headers by a factor of:

$$\frac{m_{cool}}{m_t + m_{fin} + m_{header}} = \frac{1 - \eta_m}{\eta_m} \frac{\dot{W}_{fan}}{\dot{Q}_{HX}}.$$

(73)

This analysis neglects the effect that this increased cooling requirement has on the required fan power as the motor waste heat is typically only a few percent of the total dissipated heat. Thus the total fan mass is:

$$m_{fan} = m_b + m_m + m_{cool}$$

(74)

And the total mass of the heat exchanger, not accounting for mass penalties, is

$$m_{HX} = m_t + m_{fin} + m_{header} + m_{fan}$$

(75)

To account for the incremental mass increase that the power plant would incur to generate the power required to run the fans, the Sondelski HTGR thermal cycle optimization model is run for a range of power outputs. The scaling of the reactor and recuperator mass with respect to the output power is calculated to be $G_r = 0.8205\ kg/kWe$. The reactor mas does not vary strongly with output power as the core is criticality-limited in the range of powers studied. Following the same method but varying the heat rejection system pressure drop, a mass penalty for the coolant pressure of $G_c = 2.997\ kg/kPa$ is obtained. Therefore, the total mass that the heat exchanger contributes to the overall power generation system, and the objective of the optimization model described below, is

$$m_{tot} = m_{HX} + G_r \dot{W}_{fan} + G_c \Delta P_h$$

(76)

2.2 Heat Exchanger Geometry Optimization

An optimization algorithm was then developed to determine the lowest-mass heat exchanger geometry for a given set of heat rejections parameters, ambient conditions, tube and coolant materials, and tube configuration. There are 5 geometrical parameters of interest: the tube length, tube diameter, fin pitch, the number of tube rows and the number of tube columns. Limits must be set for each value. The tube diameter is constrained to be greater than 0.5 mm due to commercial availability, the tube length and overall heat exchanger height, which limits the product of the tube diameter and number of tube rows according to Equation 17, are constrained to 4 m based on launch vehicle constraints and the minimum values of these lengths

are set to 0.1 m. The number of tube columns is constrained to be between 2 and 10 due to the availability of pressure drop correlations in this range and the minimum number of tube rows is set to 10 to avoid significant edge effects. The minimum fin pitch is set to 1.1 times the fin thickness and the maximum is set to the heat exchanger length (corresponding to having no fins).

The first three of these parameters are continuous values while the last two are discrete. The optimization problem is expected to be non-linear and non-differentiable due to the piece-wise correlations used for different Reynolds regimes and the implicit method of determining the CO_2 velocity and fan speed. Therefore, a mixed-integer non-linear problem (MINLP) solver is used. An open-source adaptive differential evolution radius-limited solver [47] is used to find the mass-optimal combination of the continuous geometrical parameters for a given set of heat rejection inputs and discrete geometrical parameters.

Figure 7 shows the results of convergence testing the model for a range of rejected heat loads and ambient pressures and temperatures for a steel heat exchanger to optimize the balance between speed and accuracy. Convergence was defined as a relative change of 0.5% between the optimal mass from subsequent runs, with the number of iterations of the above solver being increased by 500 for each run. Because the velocity-finding algorithm within the heat exchanger model described above uses a relative error of 0.1% for convergence, the overall model will not converge past this limit. By 5000 iterations, the vast majority of cases have reached the 0.5% convergence threshold, therefore this value is used in subsequent modelling. It is important to note that only the mass is convergence-tested as this is the value being optimized.

Due to the large number of optimization parameters and the nonlinearity of the problem, the model may report slightly different geometries all having very similar masses if run with the same input parameters due to the inherent variation in the optimal velocity described above. The most common occurrence of this phenomenon is seen in the variety of optimal fin pitches and is discussed in more detail in the results section. This effect does not affect the overall performance of the model for determining the minimal heat exchanger mass, but does make it harder to draw definite conclusions about the optimal fin density.

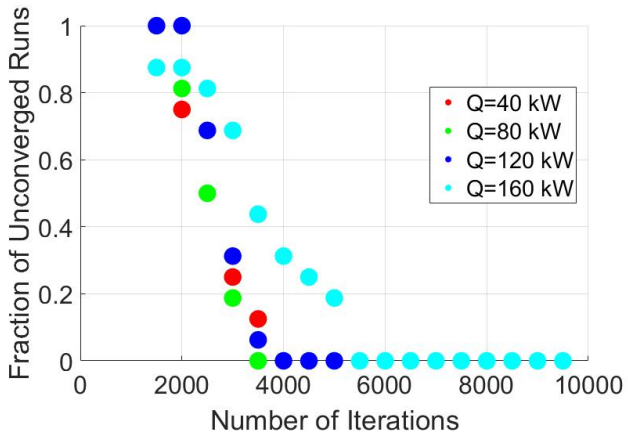

Figure 7: Convergence testing of the heat exchanger model. For each rejected heat load, 16 combinations of ambient pressure and temperature were studied. The fraction of these cases to reach the convergence threshold for a given number of iterations is shown. Lower rejected heat loads tended to converge more quickly.

Typically, optimal geometries were not constrained by the solution space boundaries except for the minimum number of tube columns for cases of low rejected heat and the maximum heat exchanger height and length for cases of high rejected heat. The runtime to find an optimal solution for a given set of input parameters is typically 1-2 minutes. The optimizer

reports the optimal values for the geometric parameters and then the associated performance characteristics for this heat exchanger are computed. In addition to the mass, the characteristics include the fan power and pressure rise, the coolant pressure drop, the heat exchanger conductance, the coolant and atmospheric side mass flow rates, and the fan efficiency and speed.

2.3 Integration with the Sondelski Thermal Cycle Model

The optimization described in the previous section provides the optimum heat exchanger mass for a given set of heat rejection parameters, i.e. the total rejected heat power, the coolant pressure, and the inlet and outlet coolant temperature, in addition to other environmental, material, and configuration parameters. However, this is not sufficient information to directly compare the efficacy of the heat exchanger compared to a radiator heat rejection system when coupled to a FSPS because the different heat rejection systems will result in different optimal cycle parameters and therefore different thermal efficiency which in turn will result in different optimal heat rejection parameters. Therefore, in order to complete the analysis, the optimization model is integrated into the existing Sondelski thermal cycle optimization code [10] in place of the radiator. As mentioned above, the Sondelski model results in very low mass estimates compared to other Mars FSPS sizing studies due to the core design, the assumed lack of shielding and other component mass estimates, but is used here because the scaling relationships between the heat rejection system and overall system masses are still useful for illustrating the relative impact of using forced convection heat rejection. For systems that do consider shielding mass and use a more conventional core model, the relative effect of changing the heat rejection method may be reduced somewhat.

The Sondelski model is implemented in MATLAB and determines the optimal cycle mass for a given compressor inlet pressure, turbine outlet temperature, desired power, ambient temperature, and various material parameters, and specifies that the radiator pressure drop will be 1% of the compressor inlet pressure. A full explanation of the model can be found in Sondelski [10] but in brief, the model first guesses a value for the radiator area and recuperator conductance and solves for the states at the compressor inlet, compressor exit, reactor inlet, turbine inlet, turbine outlet, and radiator inlet. The cycle model then determines the radiator outlet temperature by calculating the heat rejection power based on the radiator inlet temperature, ambient temperature, and guessed radiator area. The resulting radiator outlet temperature is then compared to the guessed compressor inlet temperature. The guess values are updated until the radiator outlet converges to the compressor inlet temperature. This process is used to determine the Brayton cycle thermal efficiency for a given set of conditions. The mass flow rate is varied until the net power output of the cycle equals the specified desired power output. The reactor model includes a reactivity constraint to support a 10 year operation and uses separately-developed k_{eff} correlations for the core geometry and fuel fraction to determine the reactor mass. The assumed geometry is a cylinder of HEU fuel with coolant channels throughout and reflectors for reactivity control [48]. The total system mass at this operating point is then determined using correlations for each system component. The recuperator conductance is then increased and this process is repeated until the system mass no longer decreases. A final outer loop is then employed to find the optimal radiator area, resulting in the overall minimum mass for the system with the given input parameters.

To incorporate the heat exchanger model into the thermal cycle model, the model is first modified so that it accepts as inputs the ambient temperature and pressure and the heat exchanger material. The fan power is accounted for when calculating the total core power output. New functions are written to replace the radiator model in order to calculate the total heat exchanger rejected power. In accordance with how the model functions as described above, first a heat exchanger mass is guessed instead of a radiator area and the resulting rejected power is calculated for each iteration of the model while the coolant flow rate and heat exchanger inlet temperature are optimized.

Estimates for the atmosphere-side cooling capacity and the heat exchanger conductance, as well as the fan power, are obtained from by developing a reduced order model of the heat exchanger as it would be too computationally intensive to call the detailed heat exchanger model for each condition tested by the cycle optimizer. To derive the reduced order model the heat exchanger model is run for a large array of cases. For a given set of cycle operating parameters, three relevant input parameters: the rejected heat power $\dot{Q}_{HX}$, coolant inlet temperature $T_{h,in}$ and the coolant temperature drop through the heat exchanger ΔT_h, were varied and the optimal required fan power $\dot{W}_{fan}$, specific conductance UA_{spec}, and atmosphere-side capacity rate $\dot{C}_c$ were determined for each combination of inputs for the stainless steel, aluminum, and titanium candidate heat exchanger materials. Based on its superior performance, only the staggered tube configuration with $R_p = 2$ was considered. From this dataset, best-fit correlations for the three outputs were derived using MATLAB's built-in nonlinear fit solver. To facilitate integration with the cycle model, only inputs available to the radiator model were used. These included the

coolant inlet temperature, rejected heat load, pressure drop, the heat exchanger mass, and the ambient conditions. The correlations are in the following form:

$$UA_{spec,pred} = C_{U6} + C_{U1}\left(\bar{T}_h - T_{c,in}\right)^{C_{U2}} \dot{Q}_{HX}^{C_{U3}} \Delta P_h^{C_{U4}} \mathrm{m}_{\mathrm{HX}}^{C_{U5}} \quad (77)$$

$$\dot{W}_{fan,pred} = C_{P6} + C_{P1}\left(\bar{T}_h - T_{c,in}\right)^{C_{P2}} \dot{Q}_{HX}^{C_{P3}} \Delta P_h^{C_{P4}} \mathrm{m}_{\mathrm{HX}}^{C_{P5}} \quad (78)$$

$$\dot{C}_{c,pred} = C_{C6} + C_{C1}\left(\bar{T}_h - T_{c,in}\right)^{C_{C2}} \dot{Q}_{HX}^{C_{C3}} \Delta P_h^{C_{C4}} \mathrm{m}_{\mathrm{HX}}^{C_{C5}} \quad (79)$$

Figure 8 compares the fan power, specific conductance, and capacity rate predicted by the above correlations vs the values directly from the heat exchanger model for a titanium heat exchanger operating at an ambient temperature and pressure of 260K and 600 Pa respectively, and a coolant pressure of 9 MPa. The correlations adequately predict the model-derived values for most cases.

The coolant outlet enthalpy is guessed and the corresponding outlet temperature is used to calculate the average coolant temperature and coolant temperature drop needed in the reduced order models above. The outlet enthalpy resulting from this guess value is calculated using the effectiveness-NTU equations:

$$h_{out} = h_{in} - \frac{\epsilon_{HX}}{\dot{m}_h} \dot{C}_{min}(T_{h,in} - T_{c,in}) \quad (80)$$

where the heat exchanger effectiveness is given by Equation 41. The error between the guessed and resulting enthalpies is minimized to determine the true outlet enthalpy for the given conditions. The total heat rejected to the environment is then calculated as

$$\dot{Q}_{HX} = \dot{m}_h(h_{out} - h_{in}). \quad (81)$$

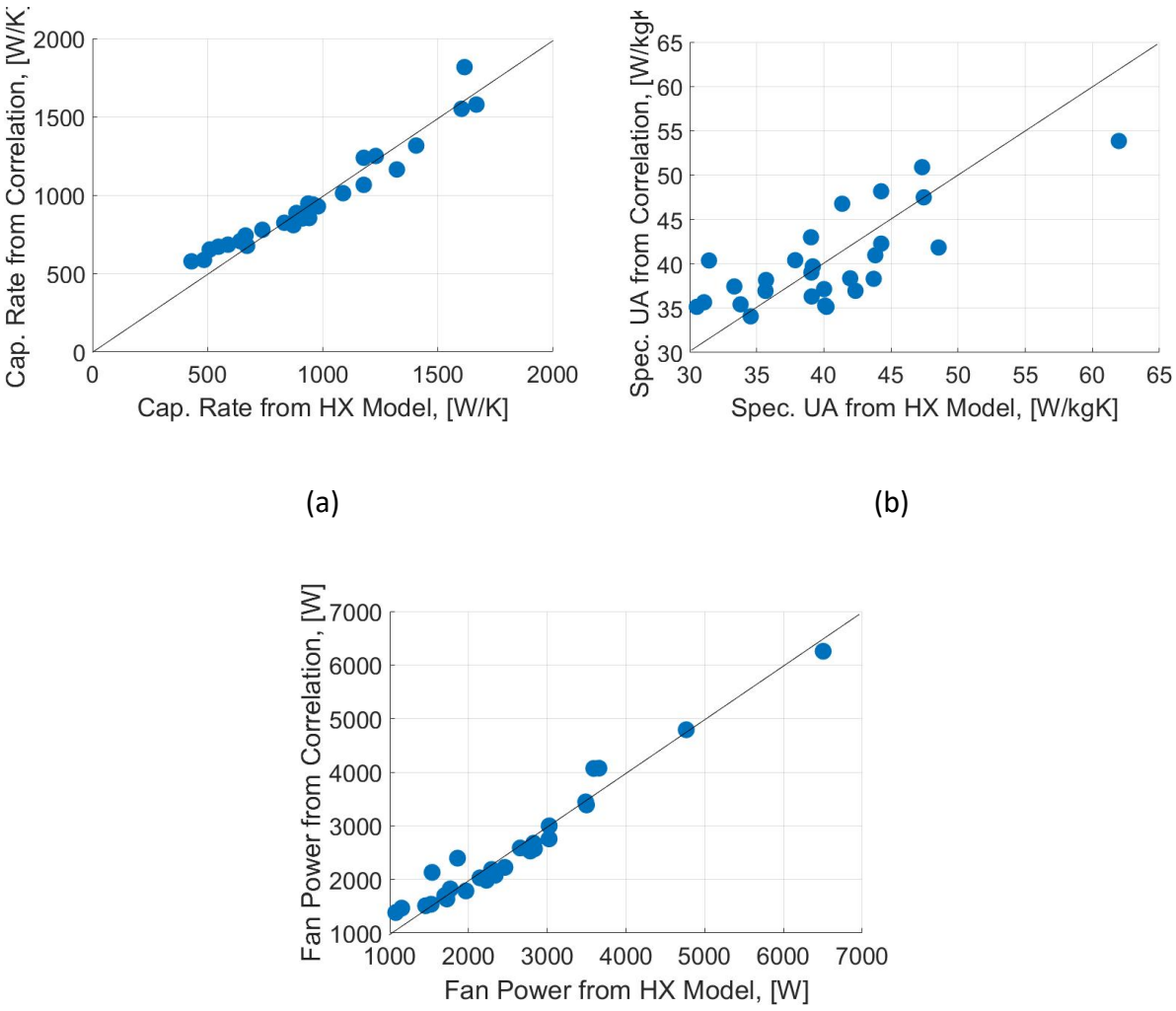

Figure 8: Comparison of the heat exchanger model results to the reduced order models used in the cycle modeling

The required fan power is calculated using the reduced order model and both this value and the rejected heat are returned. The fan power is subtracted from the net cycle power to account for the additional required power from the reactor.

2.4 Cryocooler Modelling

To determine how the use of a forced-convection heat exchanger benefits an ISRU cryocooler cycle, a single-stage recuperated reverse Brayton cycle cryocooler is modeled in Julia. The cycle is assumed to liquefy oxygen from 300 K to the saturation point at 1 bar. Neon is used as the working fluid. A T-s diagram and schematic of the cycle is shown in Figure 9.

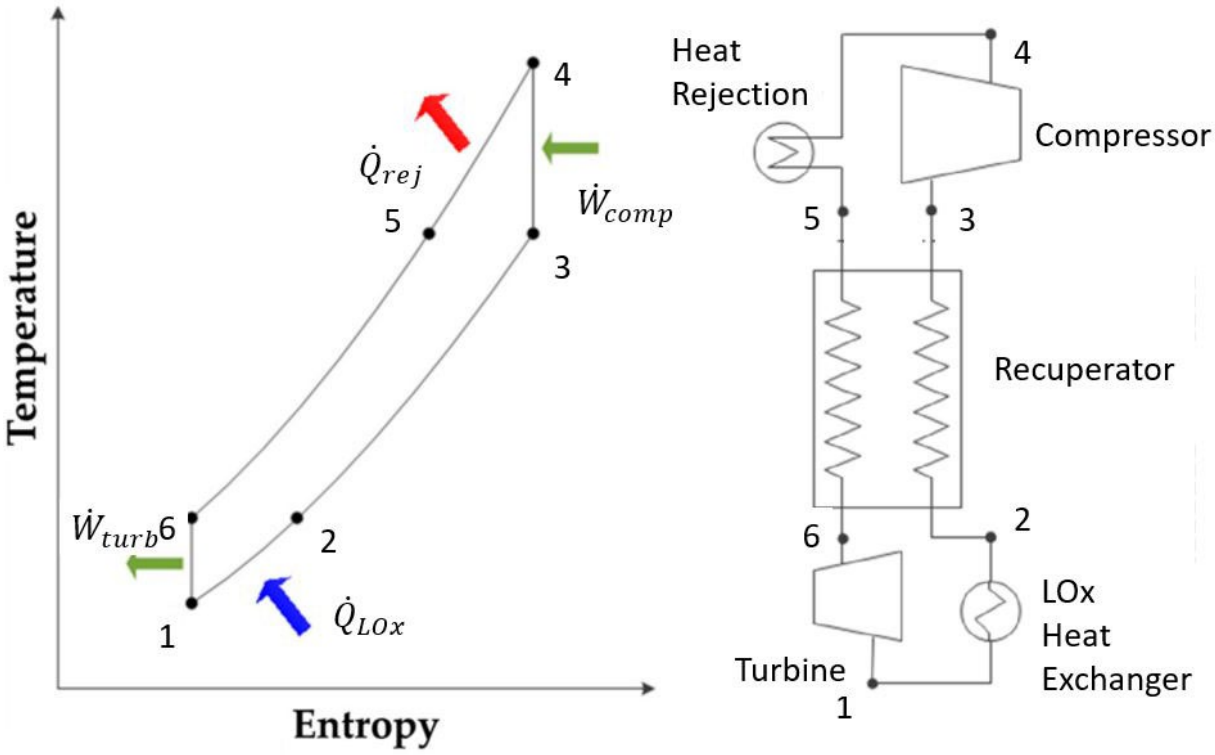

Figure 9: Cryocooler TS diagram and cycle schematic, adapted from Lee et al. [49]

$\dot{Q}_{rej}$ is the rejected heat load out of the cycle, $\dot{W}_{comp}$ is the power required by the compressor, $\dot{W}_{turb}$ is the turbine power output, and $\dot{Q}_{LOx}$, the heat removed from the oxygen to liquefy it, is calculated as

$$\dot{Q}_{LOx} = \dot{m}_{LOx}\left(h_{LOx,in} - h_{LOx,sat}\right) \quad (82)$$

where $h_{LOx,in}$ and $h_{LOx,sat}$ are the inlet and saturation LOx specific enthalpies respectively.

Mass modelling of the cryocooler is taken from Plachta and Kittel [50]:

$$m_{cryo} = 0.2\dot{Q}_{LOx}^{0.7}\left(\frac{T_4 - T_1}{T_1}\right)^{1.45} \quad (83)$$

where T_1 and T_4 are the temperatures at locations 1 and 4 on Figure 9b. The value for the specific recuperator conductance, taken from Niblick et al. [51], is set as $UA_{spec,cryo} = 3.125\frac{kgK}{kW}$. The efficiencies of the compressor and turbine are set to $\eta_{comp} = 0.5$ and $\eta_{turbine} = 0.75$ based on values used in Zaragola et al. [52] A power mass penalty accounting for the compressor in the cryocooler and the heat exchanger fan is calculated based on a range of power source specific power values representing different types of power sources that will be discussed subsequently. The heat rejection heat exchanger mass is based on the updated modelling described above. The radiator has an area specific mass of $\rho_{rad,cryo} = 3.86\frac{kg}{m^2}$, an emissivity of $\epsilon_{rad,cryo} = 0.9$ based on the lightweight radiator proposed by Morrison et al. [11], and is assumed to reject heat to a $T_{surr} = 200\ K$ background temperature.

The compressor inlet pressure and pressure ratio, the peak cycle temperature T_4, the LOx mass flowrate to be cooled $\dot{m}_{LOx}$, the ambient temperature and pressure, the recuperator conductance, and the power source power-specific mass, α, are supplied to the model as inputs. As the cryocooler requires significant electrical power and can be used with any type of power source, the mass penalty of the additional electrical power required to drive the heat exchanger fan is important and depends strongly on the power source used.

The working fluid enthalpies at states 1 and 4 are calculated based on the known temperatures and pressures at these points. The enthalpies at states 3 and 6 are calculated based on the pressure ratio and isentropic efficiencies of the turbine and compressor respectively. To solve for the remaining states, the working fluid mass flowrate, $\dot{m}_r$, must be known. A system of equations governing the cycle is solved to determine this value. The enthalpy at state 2, the cold-side heat exchanger outlet, is calculated as

$$h_2 = h_1 + \frac{\dot{Q}_{LOx}}{\dot{m}_r}.$$

(84)

The enthalpy change on both sides of the recuperator are equal, so the heat rejection outlet temperature is

$$h_5 = h_6 + h_3 - h_2$$

(85)

while the heat transfer rate across the recuperator is

$$\dot{Q}_{rec} = \dot{m}_r(h_3 - h_2).$$

(86)

The effectiveness-NTU method is used to determine the effectiveness of the recuperator. The working fluid flow rate can be determined from the above equations using a root-finding algorithm. The rate of heat rejected from the working fluid in the heat rejection system is

$$\dot{Q}_{rej} = \dot{m}_r(h_4 - h_5).$$

(87)

The compressor power required to drive the cycle is defined as

$$\dot{W}_{comp} = \dot{m}_r(h_4 - h_3).$$

(88)

The power extracted by the turbine is defined as

$$\dot{W}_{turbine} = \dot{m}_r(h_6 - h_1).$$

(89)

Contrary to typical Brayton cycle operation in power generation applications, for simplicity cryocoolers often reject the turbine power to the heat sink instead of using it to drive the compressor, so the total heat load that must be rejected is

$$\dot{Q}_{rej,tot} = \dot{Q}_{rej} + \dot{W}_{turbine}$$

(90)

Now that the heat rejection load is known, the mass of the heat rejection system can be determined for both a radiator and a forced-convection heat exchanger. The required radiator

mass can be determined from the radiator inlet and outlet temperatures and area specific mass, from Juhasz [53], as

$$A_{rad} = \frac{\dot{m}_r c_p \left[\ln\left(\frac{(T_4 - T_{surr})(T_5 + T_{surr})}{(T_5 - T_{surr})(T_4 - T_{surr})}\right) - 2\left(\tan^{-1}\left(\frac{T_4}{T_{surr}}\right) - \tan^{-1}\left(\frac{T_5}{T_{surr}}\right)\right)\right]}{4\sigma\epsilon_{rad,cryo}T_{surr}^3}$$

(91)

A mass estimate for the heat exchanger is derived from the heat exchanger modelling in the same manner as described in the section above; a reduced order model for the heat exchanger mass is fit to data obtained from running the model under a range of conditions relevant to cryocooler operation using the terms available in the cryocooler model. The result is

$$m_{HX,cryo} = 0.1199 + 0.0609(\bar{T}_r - T_{amb})^{-0.9289}\dot{Q}_{rej,tot}^{0.9874}\dot{m}_r^{0.0187}\Delta T_r^{-0.0199}$$

(92)

where $\bar{T}_r$ is the median refrigerant temperature in the heat exchanger, i.e.

$$\bar{T}_r = \frac{T_4 + T_5}{2}$$

(93)

and ΔT_r is the refrigerant temperature drop through the heat exchanger, i.e.

$$\Delta T_r = T_4 - T_5.$$

(94)

The model assumes an aluminum, staggered-tube $R_p = 2$ heat exchanger and only accounts for the physical mass of the heat exchanger and fan and not the power mass penalty or pressure drop penalty, which are accounted for separately. The fan power is similarly estimated as

$$\dot{W}_{fan,cryo} = 8.701 + 1.1299(\overline{T}_r - T_{amb})^{-1.0961}\dot{Q}_{rej,tot}^{1.0654}\dot{m}_r^{-0.1005}\Delta T_r^{0.1515}$$

(95)

and the heat exchanger frontal area is estimated as

$$A_{HX,cryo} = 0.0224 + 0.0174(\overline{T}_r - T_{amb})^{-0.747}\dot{Q}_{rej,tot}^{0.946}\dot{m}_r^{0.0508}\Delta T_r^{-0.143}$$

(96)

The power mass penalty, the additional power generation mass required to run the cryocooler, is

$$m_{pow,cryo} = \alpha\left(\dot{W}_{fan,cryo} + \dot{W}_{comp}\right)$$

(97)

For the radiator, the fan power is omitted as no fan is required. Finally the recuperator mass is

$$m_{rec} = UA * UA_{spec,cryo}$$

(98)

And the total system mass is

$$m_{tot,cryo} = m_{cryo} + m_{pow,cryo} + m_{rec} + m_{rej}$$

(99)

where the heat rejection mass, m_{rej}, either equals the radiator mass or heat exchanger mass depending on the type of heat rejection used.

Similar to the heat exchanger model, the cryocooler model determines the mass of the cryocooler for a given set of input parameters and optimization variables and then this mass is minimized by optimizing the operating conditions for the desired cycle. The optimized terms are

the pressure ratio, the peak cycle temperature T_4, and the recuperator conductance. The input parameters are the LOx flowrate, the power source specific power, the compressor inlet pressure, the ambient conditions, and the type of heat rejection system, either a radiator or a forced-convection heat exchanger. The same open-source MINLP optimizer is used to find the optimal cycle mass for a given set of input parameters.

3. Experimental Euler Number and Nusselt Number Correlation Validation

3.1 Experimental Goals

While the preliminary optimization model predicts very promising heat exchanger performance compared to a radiator, the model was built using existing correlations for low-Reynolds-number heat transfer and pressure drop that were either generated in air at 100 kPa absolute pressure [29], firmly in the continuum flow regime, or from numerical simulations that have not been validated experimentally [30], and so may not accurately predict the behavior in low-pressure CO_2 near the transition to the slip flow regime. The model also included an assumption of uniform axial flow into the heat exchanger which would not be true if the fan is situated directly upstream of the heat exchanger. To collect the heat exchanger performance data necessary to validate the modelling approach, a prototype heat exchanger and experimental facility were designed and constructed at the University of Wisconsin Thermal Hydraulics Lab. The heat exchanger was designed to replicate the geometry of the mass-optimized heat exchanger for a 40 kW_e FSPS based on a preliminary version of the model described above. The experimental facility consists of an open-cycle wind tunnel within a vacuum chamber to attain

and measure flowrates and ambient pressures relevant to operation in the Martian environment while the heat exchanger is sized based on the results of the preliminary optimization modelling The exterior of the facility is shown in Figure 10a while the interior is shown in Figure 10b.

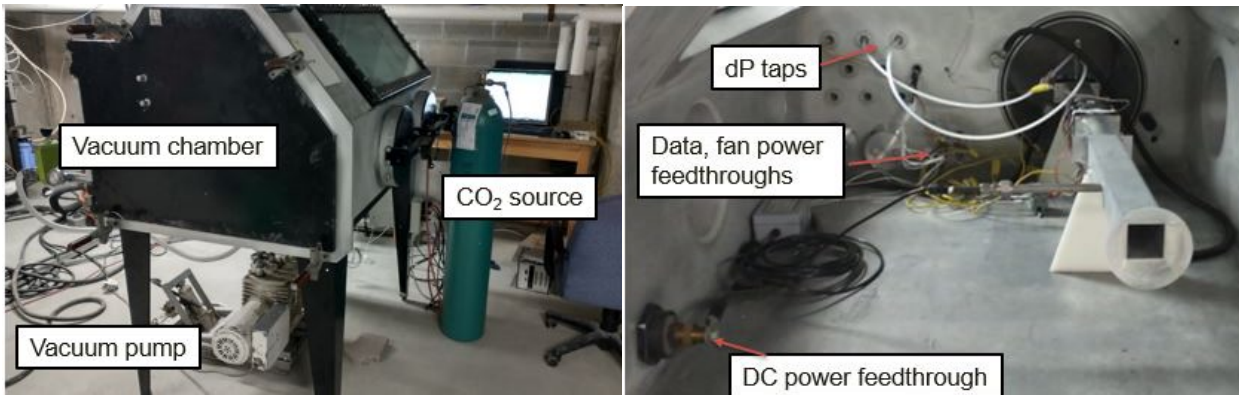

(a) (b)

Figure 10: Annotated views of the a) exterior and b) interior of the experimental facility.

The heat exchanger was operated at a variety of heat fluxes and gas flow rates and the conductance and pressure drop were measured and compared to predictions based on existing correlations. The ambient pressure was varied to discern the effect of the Knudsen number on the performance ranging from continuum flow to slip flow. The effect of the fan-induced flow irregularity was investigated by varying the fan position relative to the heat exchanger and either including or removing a flow straightener to create either axial or vortical flow conditions, respectively. Additionally, by conducting tests both in CO_2 and in air, the effects of gas composition on the experimental results can be controlled for by comparing the resulting dimensionless parameters obtained in each gas.

3.2 Heat Exchanger Design

3.2.1 Preliminary Model Results

A preliminary version of the model described in Section 2 above was used to estimate the design parameters of the optimal heat exchanger for a 40 kW_e Mars FSPS to provide a baseline for designing the experimental heat exchanger. The preliminary model used a Nusselt number correlation from the Engineering Sciences Data Unit [54] that did not account for Knudsen number, the HEDH [29] correlation for the Euler number, employed a fan efficiency model that did not account for Mach effects, and did not account for fan cooling requirements, tube internal roughness, the fan-induced vorticity at the inlet, or the laminar developing region along the fins. The results shown here should therefore not be considered representative of expected heat exchanger performance but were solely used to size the experimental heat exchanger.

The preliminary heat exchanger model was incorporated into Sondelski's FSPS thermal cycle model as described in Section 2.3 above. A staggered, $R_p = 2$ tube arranged was used. As shown in Figure 11, this arrangement resulted in the lowest mass predictions for a wide range of conditions. Higher pitch-to-diameter ratios were not studied in the preliminary or final versions of the model as the correlations used did not provide predictions for these geometries. It is therefore possible a higher value would result in slightly lower mass but the difference between ratios of 1.5 and 2 was very small so the optimal mass is not expected to be significantly lower at higher ratios.

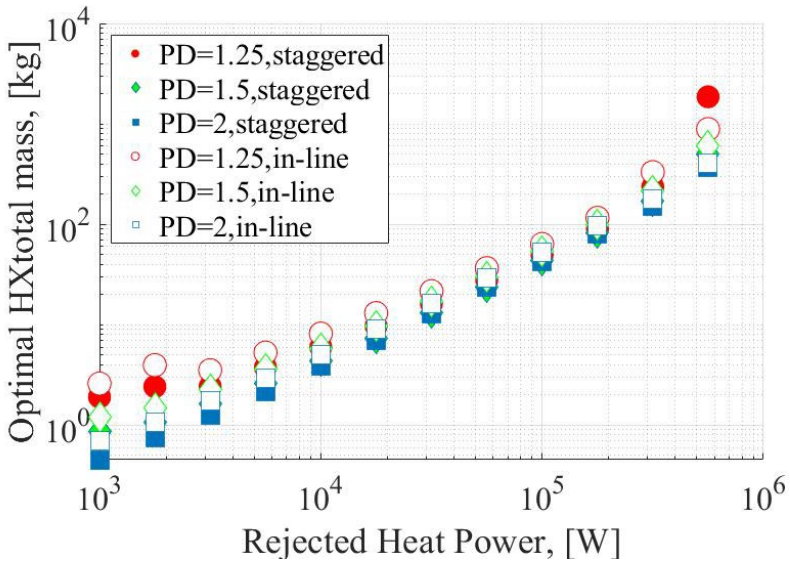

Figure 11: Comparison of the optimal Heat exchanger mass using various tube configurations with Steel tubes. PD here refers to the pitch-to-diameter ratio.

3.2.2 Preliminary Optimal Heat Exchanger Design Parameters

Table 1 compares the optimal cycles for a 40 kW_e FSPS with a turbine inlet temperature of 900 K, compressor inlet pressure of 9 MPa, and pressure ratio of 2 using both the radiator and a Steel heat exchanger. The use of a forced-convection heat exchanger reduced the predicted optimal cycle mass for a 40 kW_e power system operating at an ambient temperature of 220 K by 80%, from 782 kg to 159 kg, both by reducing the mass of the heat rejection system and by reducing the mass of the recuperator by decreasing the heat rejection temperature.

The heat exchanger cycle has a 85 K lower minimum cycle temperature, increasing thermal efficiency from 27% to 36%. The heat exchanger masses significantly less than the radiator, and the frontal area of the heat exchanger is 94% less than the required radiator surface area, eliminating the need for complex deployment mechanisms. The geometry of the optimal heat exchanger is shown in Table 2. The required fan power in this case is approximately 1 kW_e,

the atmosphere-side pressure loss is approximately 12 Pa, and the gas velocity through the heat exchanger is 12 m/s.

Table 1: Comparison of the optimal cycle mass for a radiatively-cooled and convectively-cooled system generating 40 kW_e at an ambient pressure of 600 Pa and an ambient temperature of 220 K using the preliminary heat exchanger model

Parameter	Radiator	Convective HX
Mass Flow Rate [kg/s]	1.14	0.664
Heat Rejection Temperature [K]	404	362
Minimum Cycle Temperature [K]	414	329
Cycle Efficiency	0.27	0.36
Recuperator Mass [kg]	111	29.8
Radiator/Convective HX Mass [kg]	570	26.8
Reactor Mass [kg]	101	102.5
Total Cycle Mass [kg]	782	159
Heat Rejection Area [m^2]	84	5.29 (frontal area)

The design of the experimental heat exchanger largely mirrors the optimal heat exchanger design predicted by the model. The smaller-tube heat exchanger consists of 2 columns of 0.51 mm (0.02”) diameter tubes arranged in a staggered, $R_P = 2$ arrangement between two header plates and containing no fins. The length and height of the heat exchanger flow area are 44.5 mm (1.75”), therefore the heat exchanger will consist of 43 tubes per column. This is sufficient to minimize the impact of edge effects, which typically become significant below 10 tubes.

Table 2: Preliminary geometry and performance of the optimal-cycle 40 kW_e heat exchanger

Optimal HX Geometry	Value
Atmospheric Pressure [kPa]	0.6
Heat Load [kW]	71
High-Pressure Inlet Temperature [K]	394
High-Pressure Outlet Temperature [K]	324
High-Pressure Mass Flow Rate [kg/s]	0.664
Atmosphere-side Inlet Temperature [K]	220
Atmosphere-side Outlet Temperature [K]	318
Atmosphere-side Mass Flow Rate [kg/s]	0.953
Length [mm]	1485
Tube Rows	3100
Tube Diameter [mm]	0.57
Height [mm]	3528
Tube Columns	2
Atmosphere-side Pressure Drop [Pa]	11.95
Atmosphere-side Frontal Velocity [m/s]	12.6
Fan Power [W]	1039
Optimal HX Mass [kg]	26.8

With the total heat power appropriately scaled by the frontal surface area, the heat exchanger will experience the same heat flux as the optimized Mars heat exchanger and therefore should experience the same local flow conditions and the same pressure drop and conductance per unit area. The required heat power is

$$\dot{Q}_{exp} = \dot{Q}_{HX,optim} \frac{A_{exp}}{A_{HX,optim}} = 26.4W \quad (100)$$

3.2.3 Heat Exchanger Construction

The largest difference between the experimental and the modelled heat exchanger is that the experimental heat exchanger will be resistively heated while the modelled heat exchanger was heated by passing hot fluid through the tubes. This change was made to obviate the need for a complex fluid heating and pumping system in the vacuum chamber and to allow for easier temperature measurement in the tubes without disturbing the gas flow by threading thermocouples through the tubes. Due to the slender geometry of the tubes, the temperature profile is axially uniform, which reduces the sensitivity of the performance to thermocouple placement. The difference between the measured tube centerline temperature and the approximate tube surface temperature, ΔT_{wall}, calculated as

$$\Delta T_{wall} = \frac{\dot{Q}_{HX} \ln\left(\frac{D_t}{D_{t,in}}\right)}{2N_{rows}N_{cols}k_{wall}\pi L_t} \quad (101)$$

is at most 0.05 K during operation due to the thin tube walls and high thermal conductivity. Although the temperature profile along the tubes will differ from the modelled heat exchanger, it will still be possible to measure the conductance and calculate average Nusselt number, which should not depend significantly on temperature distribution.

The tube array has an electrical resistance of approximately 6 mΩ, based on the length and cross sectional area of the tubes and the temperature-dependent bulk electrical resistivity of stainless steel [55]. Due to this very low electrical resistance, it is essential to minimize the electrical resistance in the header plates and current leads in order to avoid significant additional

heat generation in these areas that could bias the measurements or even damage the heat exchanger. Laser welding and electrically-conductive epoxy were also investigated but found to produce too much resistance.

The heat exchanger tubes are made from 304 stainless steel welded tube stock. The specified uncertainty in the tube diameter from the supplier is less than 12.7 μm and the as-inspected diameter is 0.51 mm with no variation measurable by the author. The surface roughness was not measured, however roughness is not considered to greatly affect the flow characteristics of a cylinder in laminar flow. Although aluminum generally resulted in lower heat exchanger mass in the preliminary modeling, 304 stainless steel was chosen due to its commercial availability in the required diameter and its relative ease of soldering. Steps involved in the construction of the experimental heat exchanger are shown in Figure 12 below. The tubes stock was cut to lengths of 50.8 mm (2”) on a diamond saw (fig. 12a) and deburred with 600 grit abrasive paper. The heat exchanger header plates are constructed from 25.4 mm x 3.2 mm (1”x1/8”) 303 Stainless Steel bar stock. This alloy is chosen for its machinability among Stainless Steels. To construct the small-tube heat exchanger, a 1.6 mm (1/16”) deep channel is milled into the headers and 0.53 mm (0.021”) diameter through-holes are drilled into the headers within the channel in a pattern matching the desired tube arrangement. The channel is required to minimize the required hole depth to ease manufacturing and to aid in soldering when the heat exchanger is assembled. Due to their small size, the through-holes were drilled by hand using a micro-drill press (fig. 12b and 12c) and a microscope. Threaded holes are also drilled into the ends of the headers to facilitate mounting them on the soldering jig described below, as well as on the header faces to attach one header to the heat exchanger frame with machine screws and a sprung

support to the other end to allow for thermal expansion without causing the tubes to buckle, and to attach Copper standoffs to evenly distribute electrical power to the heat exchanger tubes. The standoffs and sprung supports are shown in Figure 13a below while Figure 13b shows the assembled heat exchanger prior to soldering.

The soldering jig consisted of 2 Aluminum plates. These plates were used to precisely hold the headers in place during heat exchanger fabrication and soldering, ensuring accurate alignment of the tubes. Aluminum has a very strong oxide layer and so will not become soldered to the heat exchanger during the soldering process. The jigs enclosed the channel on the header to form a pocket into which the solder will be applied. The headers and tubes were first cleaned in an ultrasonic cleaner in acetone to remove surface contamination. The headers were attached to the jig (fig. 12d) and the tubes were each inserted into aligned pairs of through-holes such that the tube ends were even with the header faces to prepare the heat exchanger for soldering (fig. 12e and 12f).

StayBrite Lead-free solder, consisting of 96% Sn/4% Ag with a melting point of 221°C, high enough to avoid melting during heat exchanger operation, is used. A strong acid flux is used to remove the oxide layers. Slanted Aluminum parts of the soldering jig were attached to the header being soldered to prevent the solder from spilling out of the sides of the channel and to ease application. A soldering oven was constructed by wrapping a heater tape around a section of 4” diameter steel tube. A thermocouple welded to the tube surface and a PID controller provided temperature control. A large Aluminum cylinder provided a level surface to place the heat exchanger on and a thermal mass to prevent the side of the heat exchanger not being soldered from heating above the solder melting point.

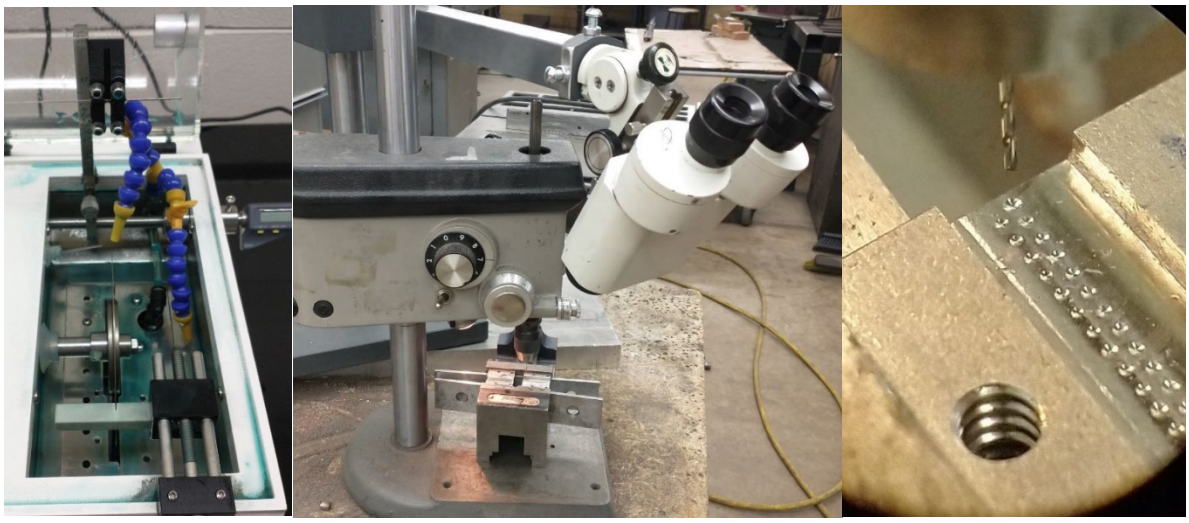

(a) (b) (c)

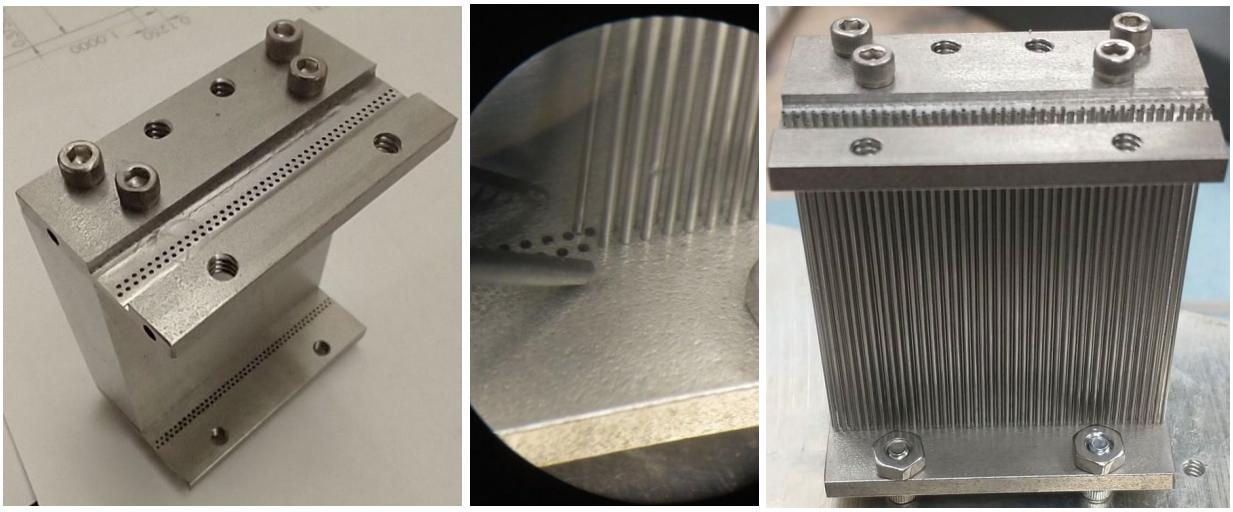

(d) (e) (f)

Figure 12: Photographs of the heat exchanger fabrication process. A) The tubes are cut to length. B) A microscope and micro-drill are used to drill the holes. C) Microscope view of drilling. D) The heat exchanger headers on the soldering jig. E) Microscope view of tube alignment process. F) Assembled heat exchanger ready to be soldered

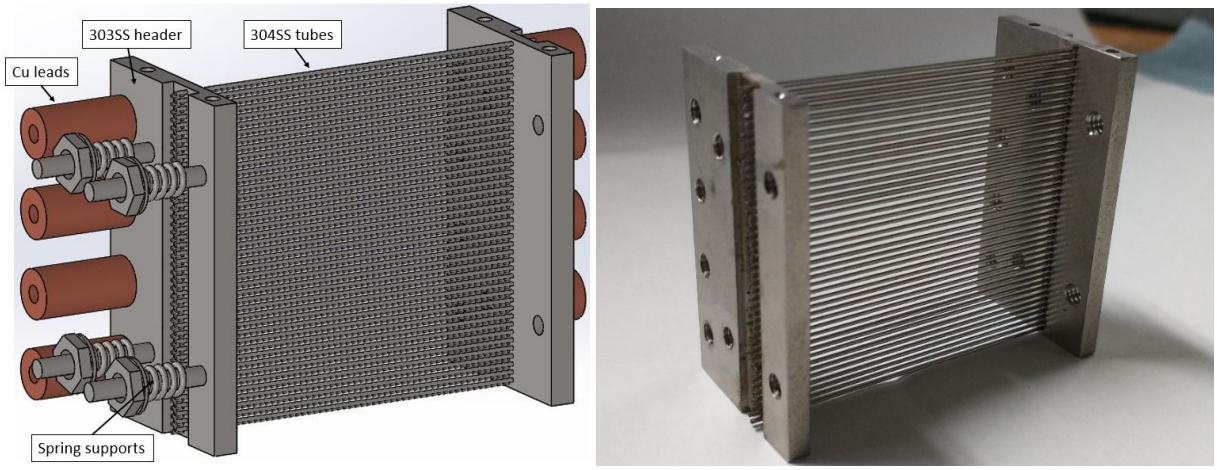

(a) (b)

Figure 13: (a) An annotated render of the heat exchanger assembly. (b) A photograph of the assembled heat exchanger headers and tubes

One header is soldered at a time. To maximize the solder contact area, the entire space between the tubes and the header within the channel is filled with solder. The header being soldered is oriented upwards and flux is applied to the header and tube ends. The steps involved in soldering the heat exchanger components together are shown in Figure 14. Solid solder wire of a volume sufficient to fill the channel is laid into the channel and the heat exchanger is placed in the solder oven (fig. 14a), which is preheated to 300°C. A heat gun is applied to the header until the solder melts and more flux is applied to ensure to solder flows between the tubes and wets all the surfaces. Additional solder is applied by hand to fill voids. The heat exchanger is then removed from the oven (fig. 14b), allowed to cool, and rinsed with a basic solution to neutralize the flux residue. The process is repeated on the other header. Some tube warping was observed due to the different thermal expansion of the tubes and the soldering jig, but this disappeared when the jig was removed. Finally, excess solder is removed by placing the heat exchanger on an autopolisher until the solder is flush with the header face (fig. 14c).

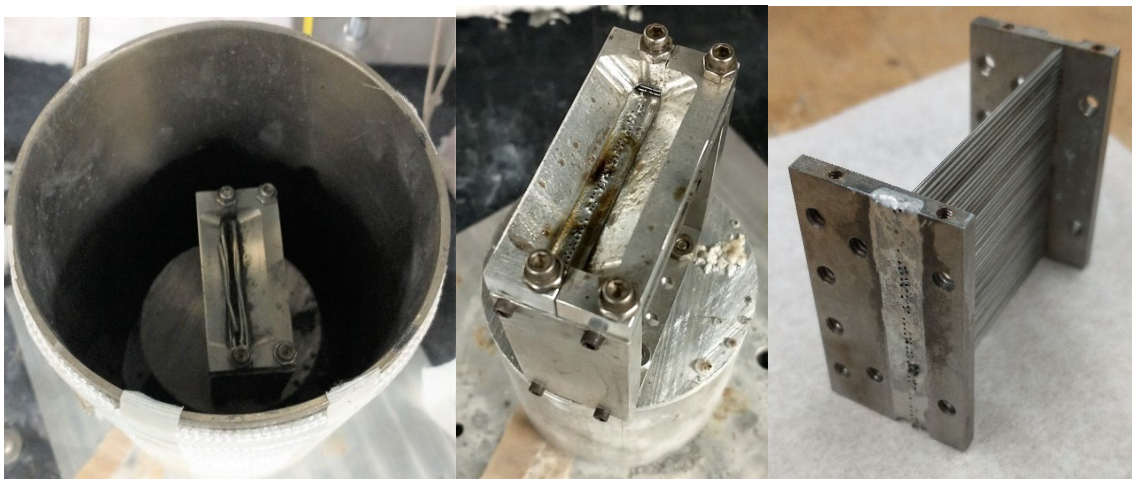

(a) (b) (c)

Figure 14: A) heat exchanger and solder in the solder oven. B) heat exchanger after soldering. C) Excess solder is removed to ensure that tube ends are open

To measure the tube centerline temperature, 40 gauge type K single-strand PFA-insulated thermocouples are threaded through 1 tube in each tube column approximately halfway between the upper and lower ends of the heat exchanger. To create the thermocouple junction, the wire ends are stripped and spot-welded together. The bare junction is then repeatedly dipped in a Boron Nitride solution and dried in an oven to create an insulation layer. This insulation is necessary to obtain accurate temperature readings while power is applied to the heat exchanger. The thermocouples are then inserted into the tubes so that the junctions align approximately with the center of the channel. The completed heat exchanger is shown in Figure 15. Note that during operation only two thermocouples were used due to limitations on the available thermocouple feedthroughs in the vacuum chamber. The uncertainties of these thermocouples and those used to measure the gas temperatures are discussed in a later section.

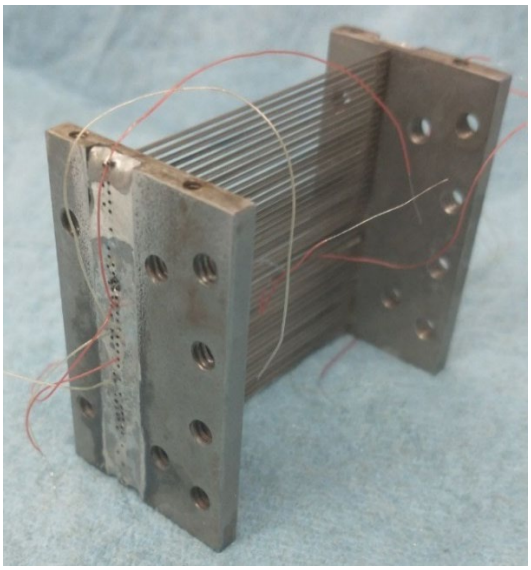

Figure 15: Experimental heat exchanger with 6 K type thermocouples inserted into 6 of the tubes to measure tube centerline temperature

To verify the quality of the electrical connection between the tubes and headers, the total resistance between the headers is measured using a high-accuracy HP 3458A multimeter and found to be approximately 6.8 mΩ, slightly higher than the predicted resistance of the tube bank itself. Figure 16 shows a FLIR image of the heat exchanger while a voltage is applied to the tubes and while the wind tunnel fan is running in ambient air. The image shows a uniform temperature distribution across the tube array and that no significant heat generation is occurring within the headers or the header-tube junctions.

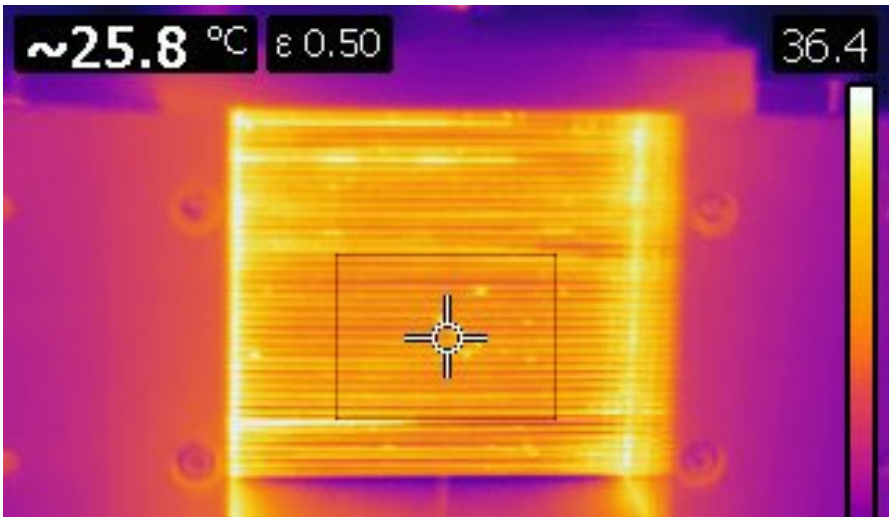

Figure 16: FLIR image of heat exchanger showing even temperature distribution while under load

Finally, voltage leads are laser-welded to each header plate to measure the voltage across the heat exchanger. Because the current across the heat exchanger and across the tube bank are the same, the voltage across the tubes is then calculated to be

$$V_{tubes} = V_{HX} \frac{R_{e,tubes}}{R_{e,HX}(\bar{T})}$$

(102)

where $R_{e,tubes}$, the electrical resistance across the tube bank, is calculated from the tube temperature, the temperature-dependent bulk electrical resistivity, and the tube geometry. The parameter $R_{e,HX}$ is the total electrical resistance across the heat exchanger and is directly measured using the multimeter over a range of tube temperatures prior to experimental data collection and interpolated based on the average tube temperature. These measurements are interpolated to find the resistance during operation at a given the tube temperature. As the two columns act as parallel paths, the electrical resistance across the tube bank is calculated from:

$$R_{e,tubes} = \frac{1}{\sum_{i=1}^{2} \frac{N_{rows} N_{cols} A_{t,xs} / L_t}{\rho_e(\bar{T})}}$$

(103)

Where A_t, xs is the tube cross-sectional area, the resistivity in each column is determined by the tube temperature in that column and the temperature-dependent resistivity $\rho_e(\bar{T})$ [55]. The electrical resistance across the headers is determined from:

$$R_{e,head} = R_{e,tot}(\bar{T}) - R_{e,tubes}$$

(104)

In all cases, the header resistance is approximately 10% of the tube resistance.

3.3 Heat Exchanger Frame Design

The heat exchanger frame holds the test heat exchanger in place in relation to the test section and provides pressure taps to measure the pressure drop across the heat exchanger. Type K thermocouples situated upstream and downstream of the heat exchanger measure the inlet and outlet gas temperature. The thermocouples are threaded through holes in the top and bottom plates so that the junctions are aligned with the center of the channel. The junctions are bare to minimize thermal resistance between the gas flow and the thermocouples and the 40 gauge wires are slender enough to neglect conduction losses. The thermocouples are approximately 13 mm upstream and 38 mm downstream of the heat exchanger tubes. The downstream distance of approximately 70 tube diameters and the nearly-uniform tube temperature distribution minimize non-uniformities in the downstream temperature distribution. Figure 17 shows an annotated view of the heat exchanger frame containing the heat

exchanger. The frame is primarily built from 6.35 mm (¼") MICA sheet to provide electrical insulation between the heat exchanger and the test section. Machine screws are used to join the parts of the frame together to ease assembly and disassembly as the frame must be partially disassembled to insert the heat exchanger. The MICA top and bottom sheet ensure that the heat exchanger headers are not in electrical contact with each other except through the tube array. The vertical MICA sheets provide attachment points to mount the frame to the test section. The ends of the frame are machined from 6.35 mm (¼") thick aluminum sheet due to the complex geometries required and because these faces do not require electrical insulation as they are only in contact with the heat exchanger header. On one side, through-holes in the end face allow machine screws to fix the heat exchanger header in place while on the other end, the spring posts for the sprung support penetrate the frame. The sprung support consists of four threaded rods sticking out from the header that pass through the heat exchanger frame while a washer and nut on the end compress four springs against the outside of the frame to provide tension while the spring posts prevent lateral or vertical motion. The expected thermally induced motion at 423 K is:

$$\Delta L = L_t \alpha_{SS} \Delta T = 0.095mm \qquad (105)$$

where α_{SS} is the thermal expansion coefficient of 304 stainless steel. AA-77 compression springs with a maximum deflection of 1.5 mm and a maximum load of 37.4 N were used to ensure sufficient tension could be applied to the tubes while under thermal strain.

On the fixed side, a 3.2 mm (1/8"), 25.4 mm (1") wide deep channel is installed so that the flow-facing side of the heat exchanger header is made flush with the flow-facing side of the

frame to reduce pressure loss not caused by the tubes. On the sprung side, a 4.8 mm (3/16”) channel is installed so that the sprung header similarly sits flush but has room to move when the tubes are heated. Each end face also has a hole that is aligned with the center of the tube bank to allow the tube thermocouples and the heat exchanger voltage leads to pass through. Pressure taps are located approximately 12.7mm upstream and downstream of the heat exchanger to measure the pressure drop; the taps consist of a 6.35 mm (¼”) steel tube epoxied to a hole drilled through the MICA sheet. Flexible hoses attached to the pressure taps are passed through vacuum chamber feedthroughs to a low-range, vacuum-compatible differential pressure sensor, detailed below.

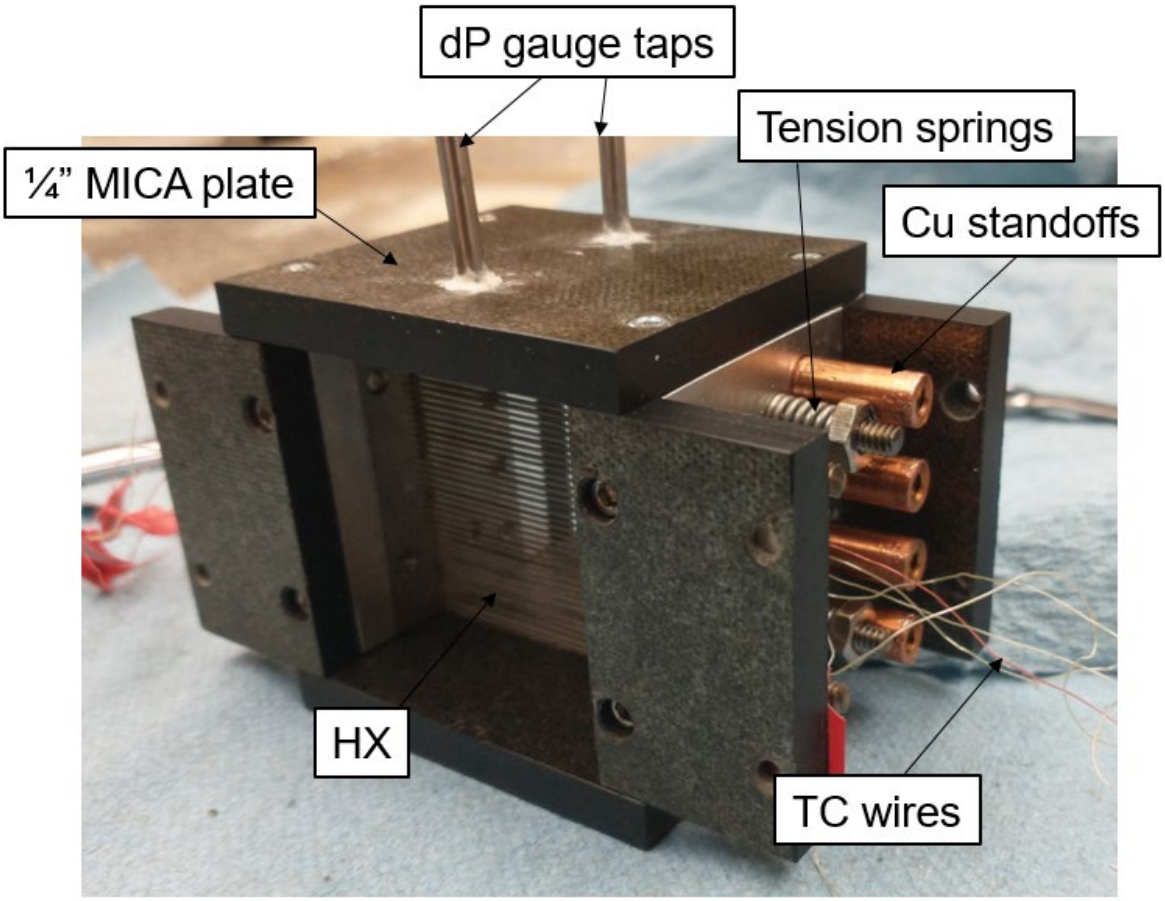

Figure 17: Annotated photograph of the heat exchanger and frame

3.4 Test Section Design

The experimental test section is essentially an open cycle wind tunnel placed within the vacuum chamber. The body of the test section consists of a 44.5mm (1.75”) square aluminum tube. An annotated photograph of the test section configured to produce axial flow is shown in Figure 18. Note that during operation three fans were required to achieve the flow rates. The test section size and heat exchanger size were chosen to maximize the heat exchanger frontal area while maintaining six hydraulic diameters of length upstream and downstream of the anemometer to minimize flow non-uniformity within the confined space of the vacuum chamber. Even so, the flow is still developing as it encounters the anemometer so an appropriate velocity peaking factor is applied as discussed in the anemometer calibration section below. 3D-printed inlet and outlet flares reduce overall pressure losses and flow non-uniformity. Plastic legs support the test section and prevent electrical contact with the chamber floor. The test section components are connected using custom aluminum brackets to allow for precise alignment to reduce pressure loss and easy assembly and reconfiguration into either the axial flow, vortical flow, or anemometer calibration configuration. Foam gaskets limit flow leaks in the joints between components.

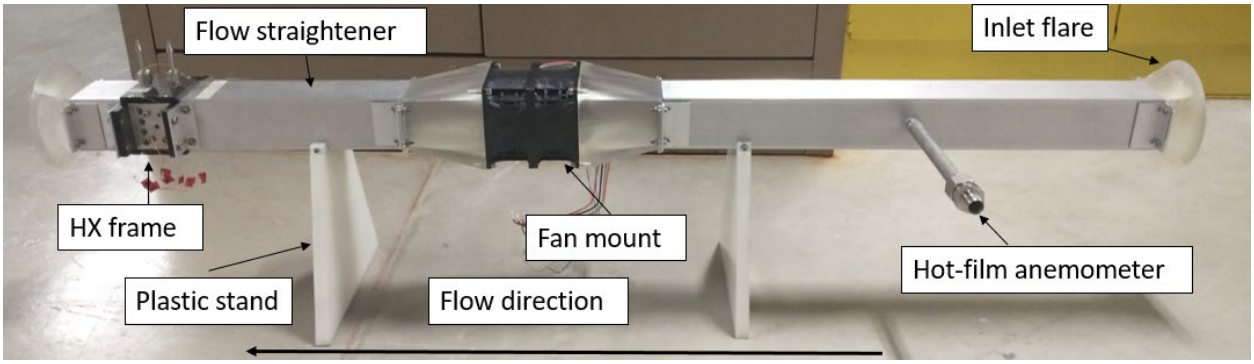

Figure 18: Annotated view of the test section in the axial flow configuration

3.4.1 Anemometer Section

Downstream of the test section inlet, the anemometer mount holds a TSI Model 8455 air velocity transducer probe in position so that the probe head is aligned with the centerline of the channel. The mount consists of a 12.7mm (½") diameter tube attached to the test section channel at a right angle. The probe is inserted into this tube and a Swagelok connector on the probe shaft seals the tube end and holds the probe in position. The probe is a hot film anemometer type velocity sensor. The anemometer has a variable range from 0-1 m/s to 0-10 m/s and an uncertainty of 0.5% of the selected range. The range used in all experimental runs was 0-1.5 m/s so the absolute uncertainty was 0.0125 m/s. This type of flowmeter is chosen in order to minimize pressure drop in the system (required since the fans used to energize the system produce relatively low pressure rise) as well as its relatively low cost and ease of use. The anemometer is calibrated in standard air by the manufacturer and therefore must be recalibrated prior to data collection. The calibration process is described below. The anemometer is situated upstream of any flow-disturbing element, e.g. the fans, heat exchanger, or the flowmeter calibration setup, to improve measurement reliability.

3.4.2 Fan Selection and Fan Section Design

Proper fan selection for this project was challenging due to the limited data available on fan performance in relevant conditions. According to the classical fan scaling laws, pressure rise increases with fluid density and with the square of rotational speed and fan diameter, therefore in order to generate sufficient pressure rise in the low-density fluid, rotational speed should be as high as possible for a given fan size and airfoil shape. However, the speed of sound on Mars is

lower than on Earth, approximately 270 m/s, and compressibility effects have been found to significantly erode fan efficiency at tip Mach numbers great than 0.7 [8], limiting the maximum feasible fan speed and therefore blade Reynolds number. Finally, tests on fan performance at low blade Reynolds number, defined in Equation 55 above, have shown that below a value of roughly 20,000, the fan scaling laws overpredict pressure rise by as much as 25% [44]. For the operational heat exchanger, assuming a fan diameter equal to the tube length of 1 m and a tip Mach number of 0.4 (based on a typical optimal heat exchanger width and required flowrate from the preliminary modelling), and a mid-span chord equal to the blade length, the blade Reynolds number would be approximately 23,000. Therefore the typical fan scaling laws should still apply albeit at reduced efficiency. Employing the correlations developed by Quin et al. [44] for fan performance at low Reynolds number for the fan blade design used in a typical commercial high-flowrate axial fan, a single ducted fan of this design should produce 37 Pa of pressure rise at a flow speed of 12 m/s through the heat exchanger, and Neustein [45] predicts an efficiency of approximately 0.45 at this Reynolds number and flow coefficient, indicating that fan performance should be sufficient to meet the flow requirements of the optimal heat exchanger geometry.

However, due to its much smaller radius, fan performance in the experimental test section may differ considerably from that expected by simply applying the fan scaling laws as the fan will operate in an unusual low (~1000-2000) Reynolds number, high Mach number regime, for which scarce experimental data exists. This unavoidable discrepancy between the flow regimes of the experimental and operational fans precludes the possibility of collecting fan performance data relevant to the full scale device, but also allows for more relaxed experimental

fan selection criteria as the only requirement is that it be able to generate sufficient flow rate and pressure rise to match that required by the optimal heat exchanger.

Veisman et al. [36] describe the construction of a low-density multi-fan wind tunnel for testing the Mars Ingenuity helicopter using an array of off-the-shelf Delta Electronics GFM0812DUB7S contra-rotating axial fans. This model fan was used for this project as it is the only fan of appropriate size and cost demonstrated to operate at the test conditions. The authors report a decrease of the head coefficient, of 40% at test conditions compared to STP conditions. Based on the manufacturer-provided $\Delta P - \dot{V}$ curve for this fan, the estimated pressure rise at the desired flow rate in test conditions is 13 Pa. However, in practice 3 fans in series were required to generate sufficient flow through the heat exchanger at 1 kPa ambient pressure to reach the minimum tube Reynolds number of 7 for which the existing correlations were valid.

The fans are PWM controlled using a 25 kHz signal and output a tachometer signal that pulses once per revolution. Due to the low-density environment limiting available convective cooling, the fans were prone to overheating. A type K thermocouple was bonded to the fan casing in order to monitor fan temperature. The fans were turned off and allowed to cool down once they reached 40°C to prevent overheating. 3D-printed transition sections between the square test section channel and the round fan housing minimized pressure loss and flow disturbance upstream and downstream of the fan section.

3.4.3 Flow Straightener and Outlet Sections

Downstream of the fan section, a 3D-printed flow straightener ensures that the flow entering the heat exchanger is largely axial and uniform without producing excessive pressure

loss. The flow straightener consists of a grid of 16 equally-sized square channels. The channel length to hydraulic diameter ratio is 6, a value typically used in wind tunnel flow straighteners to significantly reduce vorticity [56]. To measure the heat exchanger performance in vortical flows, the section containing the flow straightener is removed so that the fan section directly precedes the heat exchanger section.

Downstream of the flow straightener, the heat exchanger frame holds the heat exchanger in line with the flow. Finally, the outlet section consisting of a straight section of square channel and a 3D-printed flare identical to that on the inlet side is connected to the outlet side of the heat exchanger frame. The downstream gas thermocouple is located here, approximately 38 mm downstream of the heat exchanger at the center of the channel.

3.4.4 Vortical Flow Configuration

Due to its modular construction, the test section could be rearranged to produce vortical flow at the heat exchanger inlet in addition to axial flow. Figure 19 shows an annotated photograph of the test section in the vortical flow configuration. The flow straightener section is placed downstream of the heat exchanger and the fan section is placed directly upstream of the heat exchanger. The upstream section containing the hot-film anemometer remains unchanged so no re-calibration of the anemometer was necessary.

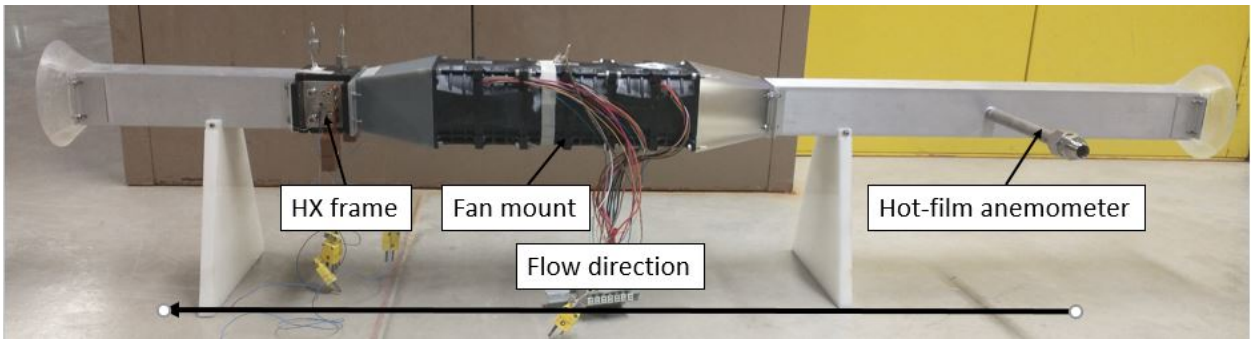

Figure 19: Annotated view of the test section in the vortical flow configuration

3.5 Test Facility Design

The experimental test facility was placed within a roughly 1 m^3 vacuum chamber glovebox. The chamber has large glass laminate windows for observation and a large door at one end for easy access to the test section. Numerous ½" and ¼" NPT ports allow for the installation of thermocouple, pressure tap, electrical data, and electrical power feedthroughs. A high-current welding feedthrough, rated for 150 Amps, is also installed as well as large vacuum line ports for evacuating the chamber.

The heat exchanger will dissipate approximately 26 W of heat during testing, calculated in Equation 100 above, and the walls of the facility have an area of approximately $A_{wall,vc} = 3.6\ m^2$ and consist of steel plates of thickness $t_{wall,vc} = 1.27\ cm$. Approximating the natural convection heat transfer coefficient in the lab as $\bar{h}_{nc,out} = 12\ W/m^2K$ the natural convection heat transfer on the inside of the chamber walls as $\bar{h}_{nc,out} = 1\ W/m^2K$, and assuming the gas temperature within the facility is uniform, a reasonable assumption given the high volumetric flowrate through the heat exchanger, the temperature difference between the CO_2 in the test facility and the ambient room temperature is

$$\Delta T_{amb} = \left(\frac{1}{\bar{h}_{nc,out} A_{wall,vc}} + \frac{t_{wall,vc}}{k_{wall,vc} A_{wall,vc}} + \frac{1}{\bar{h}_{nc,in} A_{wall,vc}} \right) \dot{Q}_{HX,exp} = 7.98\ K \quad (106)$$

Therefore it is not expected that active cooling measures will be required to maintain a constant temperature within the chamber.

An MKS absolute piezo pressure transducer with a relative accuracy of 1% is used to measure the pressure within the vacuum chamber while a type K thermocouple measures the temperature far from the test section. For the CO_2 test runs a syphon bottle of industrial grade (99%) CO_2 is provided to the chamber through a pressure regulator to maintain the target pressure and composition during operation. A Digiweight DWP121 digital scale measures the mass of the CO_2 bottle to ensure sufficient gas supply during operation. A typical test run consumed approximately 1 kg of CO_2. An Aalborg GFC17 thermal mass flowmeter controls the flowrate from the bottle to the vacuum chamber and allows for PID control of the flowrate up to 500 mL/min N_2. A bypass is also installed to allow for rapid filling of the vacuum chamber after a Trivac D30AC vacuum pump is used to evacuate the chamber prior to operation.

The gas pressure drop through the heat exchanger is measured using a Mercoid 3100D vacuum-rated differential pressure gauge with a range of 0-75 Pa and an accuracy of 0.75% FS, which equates to an absolute uncertainty of 0.5625 Pa. This extremely low range and high accuracy are required to minimize the measurement error because the predicted pressure drop at the lowest-pressure conditions is approximately 12 Pa. While this gauge was the lowest-range and highest-accuracy gauge that was available within the project budget, the relative error from

the differential pressure measurement of 4.7% at 12 Pa dP is still quite high. Additionally, as described below, the differential pressure gauge is used to take the laminar flow meter measurements required to calibrate the anemometer. Therefore, the accuracy of this gauge strongly affects the uncertainty of the computed measurements.

An HP6681A 8V, 580A DC power supply is used to provide the current needed to resistively heat the tubes in the heat exchanger. The power supply is PID controlled to maintain a constant heat exchanger tube temperature by varying the output voltage. Current is passed through the welding feedthrough to the heat exchanger through a 2/0 gauge insulated conductor, and the negative side of the heat exchanger is grounded to the vacuum chamber inner wall. The conductor leads are bolted to a large copper bus bar on each end of the heat exchanger to evenly distribute the current across the tube array. A conductor ties the vacuum chamber outer wall to the negative terminal of the power supply, providing grounding for the system.

A 24VDC power supply provides power to the mass flowmeter and differential pressure gauge, while a 12 VDC power supply provides power to the fans, vacuum gauge, and the anemometer. A National Instruments SCXI1000 chassis, containing an SCXI1325 analog input/output module and an SCXI 1303 thermocouple input module, is connected to a lab computer via a PCI-6281 card to enable data collection and system control via a custom Labview VI. The power supplies and SCXI chassis are mounted and grounded to the vacuum chamber wall. A CO_2 monitor next to the vacuum chamber monitors ambient CO_2 concentrations during operation for safety.

3.5.1 Data Acquisition and Control Setup

A Labview VI is written to control the system and record data. The system monitors the vacuum chamber ambient pressure are temperature, the fan temperature, the voltage and pressure drop across the heat exchanger, the tube temperatures and CO_2 temperatures on the upstream and downstream sides of the heat exchangers, and the uncalibrated anemometer reading. Each of these data is recorded once per second. A screenshot of the LabVIEW interface is shown in Figure 20. Transients exhibited during a change in fan duty cycle are shown. The anemometer reading and heat exchanger pressure drop immediately rise, while the tube temperatures and gas outlet temperatures initially drop due to the higher mass flowrate. The PID-controlled heat exchanger voltage then rises in response until the downstream tube temperature again reaches the setpoint. Meanwhile. The ambient pressure and temperature remain largely constant and the fan temperature slowly rises. At each steady state condition, data are recorded for approximately 45 seconds and the mean value and standard deviation are later calculated. Recorded data are continuously appended to an excel file and saved during operation to prevent data loss.

The VI controls the fan speed by outputting a 25 kHz PWM signal at a desired duty cycle. The output voltage of the high-current DC power supply is PID controlled to hold a desired downstream tube temperature. The thermal mass flowmeter is PID controlled to hold a desired chamber pressure. The vacuum pump throttle valve is manually adjusted so that the flowmeter steady state flowrate is sufficient to ensure a 98% CO_2 composition during operation, based on the measured leak rate after initial pump down.

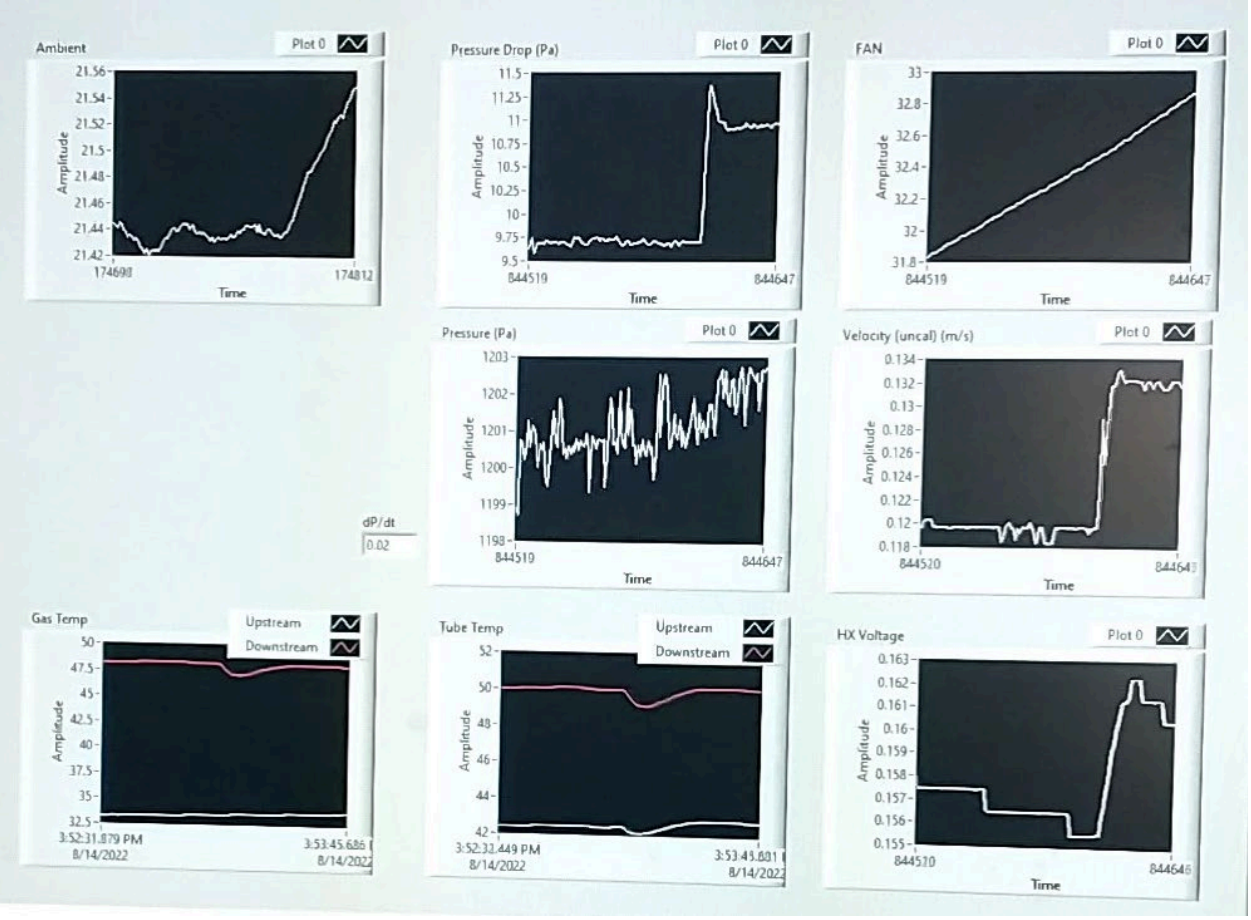

Figure 20: Layout of the data acquisition interface. From top to bottom and left to right: ambient temperature, pressure drop, fan housing temperature, ambient pressure, anemometer reading, gas inlet and outlet temperatures, upstream and downstream tube temperatures, and the voltage across the heat exchanger.

3.6 Anemometer Calibration

The hot film anemometer must be calibrated at the test conditions to accurately measure the flow rate. The hot film anemometer operates by applying a known heat flux to a roughly 1 mm^2 flat plate aligned parallel to the flow. Increasing the flow rate of gas over the plate increases the heat transfer coefficient between the plate and the flow. By measuring the power required to maintain a certain film temperature, the Nusselt number on the plate can be calculated. By assuming fluid properties of the gas, the flow rate required to produce that Nusselt number can

be determined based on Nusselt number correlations for laminar flow over a flat plate. In practice, the anemometer is calibrated by measuring the signal output at various known velocities and this calibration factor is used to display the measured air velocity to the user. However, in principle the anemometer should work the same way in a different gas as long as the flow across the plate remains laminar provided that appropriate correction factors for the physical properties of the gas are applied. It is assumed that the Nusselt number on the plate follow the correlation given by Churchill and Ozoe [57] and so the heat transfer coefficient is:

$$\bar{h}_{anem} = \frac{k_c}{L_{anem}} \overline{Nu}_{anem} = \frac{0.6774 k_c Pr^{\frac{1}{3}} Re_{anem}^{\frac{1}{2}}}{L_{hfa}\left[1 + \left(\frac{0.0468}{Pr}\right)^{\frac{2}{3}}\right]^{\frac{1}{4}}} = C_{props} u_{anem}^{1/2}$$

(107)

where $\bar{h}_{anem}$, L_{anem}, $\overline{Nu}_{anem}$, and Re_{anem} are the heat transfer coefficient, characteristic length, Nusselt number, and Reynolds number of the hot film anemometer heated section respectively. For simplicity, the terms corresponding to the physical properties of the gas are combined and denoted as C_{props}.

In a given gas flow, the anemometer will report the velocity of the calibration gas, air at 1 bar, that is required to produce the same heat transfer coefficient on the plate. Therefore equating the heat transfer coefficient of the measured flow to the heat transfer coefficient of a flow of standard air at the anemometer-reported velocity provides an estimate the relationship between the actual experimental flow velocity and the velocity reported by the anemometer:

$$u_{exp} \propto \left(\frac{C_{props,cal}}{C_{props,exp}}\right)^2 u_{anem}$$

(108)

Additionally, because the anemometer is intended for operation in free flows and not a small channel, a centerline velocity peaking factor, K_{peak}, for a given flow condition must be calculated based on the Reynolds number and development length in the square channel upstream of the anemometer using tables given by Han [58]. This peaking factor relates the velocity measured by the anemometer at the center of the channel to the average velocity across the whole channel.

The above relationship provides a theoretical description of how to relate the actual velocity to the anemometer reading. In this work, the anemometer is calibrated directly to the gas of interest using these equations as a guide to develop the calibration equation. A laminar flowmeter, consisting of a bundle of identical circular tubes fixed to two header plates and inserted into the flow path downstream of the anemometer, is designed and built to measure the flowrate at various conditions and fan settings at the same time that anemometer readings are taken in order to generate a calibration curve between the anemometer reading and the actual gas flow rate. The calibration procedure was carried out for each gas of interest, in this work for both CO_2 and air. By measuring the pressure drop across the meter the actual flow rate can be calculated based on well-established laminar flow relations. The laminar flowmeter cannot be used during the heat exchanger data collection because the fan section cannot generate enough head to drive flow through both the heat exchanger and laminar flowmeter together at the desired flowrates.

3.6.1 Test Section Calibration Configuration

Figure 21 shows an annotated view of the test section calibration configuration. The inlet and anemometer sections are unchanged to minimize the differences between the flow conditions experienced by the anemometer in the two cases. Downstream of the anemometer section, a 3D-printed transition section connects the square channel to a 75 mm diameter acrylic tube housing the laminar flowmeter. Pressure taps upstream and downstream of the flowmeter connect to the same differential pressure meter that is used in subsequent testing to measure the heat exchanger pressure drop. The fans are placed downstream of the laminar flowmeter to provide the necessary flowrate through the meter without disrupting the flow distribution.

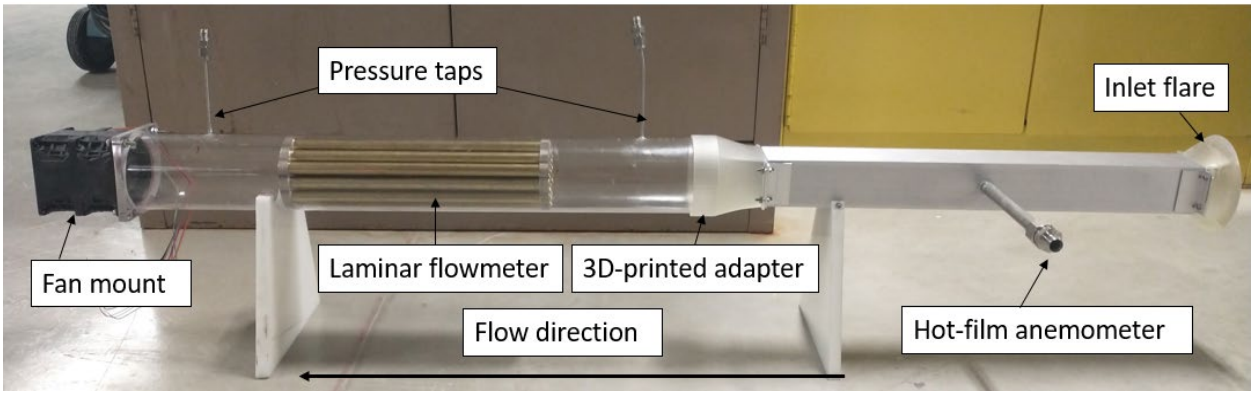

Figure 21: Annotated view of the anemometer calibration configuration of the test section.

3.6.2 Laminar Flowmeter Design

The laminar flowmeter consists of a tube bundle and two header plates positioned within a circular tube, as shown in Figure 21 above. The tubes are sized to achieve the best balance between generated pressure drop which increases measurement accuracy and overall flowmeter length which is constrained by the space available in the vacuum chamber. The total pressure drop across the laminar flowmeter is:

$$\Delta P_{lfm} = \Delta P_{t,lam} + \Delta P_{loss}$$

(109)

where $\Delta P_{t,lam}$, the pressure drop in a circular pipe under developing and fully-developed laminar flow, is given by Shah and London [59] as

$$\bar{f}_{lfm} = \frac{4}{Re_{t,lfm}}\left[\frac{3.44}{\sqrt{L^+}} + \frac{\frac{0.3215}{L^+_{lfm}} + 16 - \frac{3.44}{\sqrt{L^+_{lfm}}}}{1 + \frac{0.00021}{\left(L^+_{lfm}\right)^2}}\right]$$

(110)

$$\Delta P_{t,lam} = \frac{\bar{f}L}{D_{t,lfm}}\frac{\rho u^2_{t,lfm}}{2}$$

(111)

where L^+_{lfm}, the dimensionless length for a hydrodynamically developing internal flow, is defined as

$$L^+ = \frac{L}{D_{t,lfm} Re_{t,lfm}}$$

(112)

and $D_{t,lfm}$, $u_{t,lfm}$, and $Re_{t,lfm}$ are the inner diameter, velocity, and Reynolds number of the tubes in the laminar flowmeter. ΔP_{loss}, the pressure loss from the inlet contraction and outlet expansion of the flowmeter, is approximated using the circular tube bundle header loss functions given by Webb [60].

The tubes are arranged in a hexagonal pattern to optimize packing density and reduce the degree of flow contraction. The number of tubes that comprise the flowmeter is given by:

$$N_{t,lfm} = 1 + 3\,floor\left(\frac{D_p}{2D_{t,lfm}} - 0.5\right)\left[1 + floor\left(\frac{D_p}{2D_{t,lfm}} - 0.5\right)\right]$$

(113)

where D_p is the diameter of the circular pipe within which the laminar flowmeter is positioned. To determine the optimal flowmeter geometry for calibrating the anemometer at the test conditions, the number of tubes is determined for tube diameters ranging from 3.2 to 25.4 mm (0.125" to 1") and the flowmeter length for each tube size is determined by setting the desired flowmeter pressure drop to 14 Pa and the volumetric flowrate to 0.024 m^3/s. The above equations are solved to determine the tube length necessary to generate the desired pressure drop at the desired flowrate. This combination of pressure drop and flow rate were chosen based on the optimized flow conditions from the heat exchanger modelling. The tube size that resulted in the optimal geometry, subjectively determined by considering the length, materials costs and ease of construction, was 12.7 mm (1/2"), which yields a flowmeter that is 27.9 cm long comprised of 19 tubes, spaced on 15.2 mm (0.6") centers. In this configuration, the expected pressure drop within the tubes at the desired flowrate is 12.61 Pa and the pressure loss from the headers is 1.39 Pa.

The flowmeter was constructed from brass tubing and 12.7 mm acrylic plates for the headers. A hexagonal hole pattern was drilled into each header plate and the tubes were cut to length and then inserted into the headers. The tube ends were aligned with the header faces to reduce header losses.

3.6.3 Calibration Approach

The test section in the anemometer calibration configuration is installed into the vacuum chamber. The anemometer and pressure taps are installed into the test section. The first calibration run is performed in standard pressure air. As the anemometer is calibrated for this condition, by measuring the laminar flowmeter pressure drop, calculating the expected velocity to produce that pressure drop given the ideal geometry of the laminar flowmeter, and comparing that velocity to the velocity measured by the anemometer, a correction factor to correct for the specific geometry and flow conditions of the flowmeter, K_{lfm}, is produced. The laminar flowmeter correction factor is calculated as

$$K_{lfm} = \frac{u_{anem}}{u_{lfm} K_{peak}}$$

(114)

The average value of K_{lfm} over the range of anticipated Reynolds numbers was 1.03 and does not vary significantly with Reynolds number indicating that both the anemometer and the laminar flowmeter are operating as expected.

Once the laminar flowmeter correction term is calculated, calibration data at the experimental conditions are collected. To achieve the target pressure, the vacuum chamber door is sealed and the vacuum pump is used to remove air from the chamber. Once the chamber reaches 800 Pa, the pump is shut off and an initial leak check is performed to ensure a good seal was achieved. If so, CO_2 is admitted into the chamber using the bypass line until the internal pressure reaches 80 kPa, i.e. once the internal composition is roughly 98% CO_2. The pump is again turned on and the pressure reduced to 800 Pa, the lowest target pressure. A second leak rate

test is performed to ensure adequate CO_2 concentration can be maintained for the duration of testing.

Once the target pressure was reached, the fan duty cycle was set to the lowest value that produced a measurable reading on the anemometer. Once the laminar flowmeter pressure drop stabilized, the anemometer, laminar flowmeter pressure drop, ambient pressure and temperature were recorded for approximately 45 seconds. The duty cycle was then increased and more data collected until the fan reached its maximum speed. The pressure was then increased to the next target pressure and the above process was repeated. Calibration data were also collected in low pressure air.

From the calibration data, the flowrate through the laminar flowmeter was calculated using the same pressure drop relations described in the laminar flowmeter design process. The ratio of the calculated flowrate to the anemometer reading, corrected by the centerline peaking factor and normalized by the fluid properties, is:

$$K_{anem} = \frac{u_{lfm}}{K_{peak}\left(\frac{C_{props,cal}}{C_{props,test}}\right)^2 u_{anem}}$$

(115)

Figure 22 shows the calculated anemometer correction factors K_{anem} for each of the test pressures as a function of the Reynolds number in the channel at the anemometer location for CO_2. For most conditions tested, the uncertainty of K_{anem} was below 5%, however for the lowest-velocity cases, i.e. the low Reynolds, high pressure cases, the uncertainty reached 20% driven largely by the low pressure drop across the laminar flowmeter.

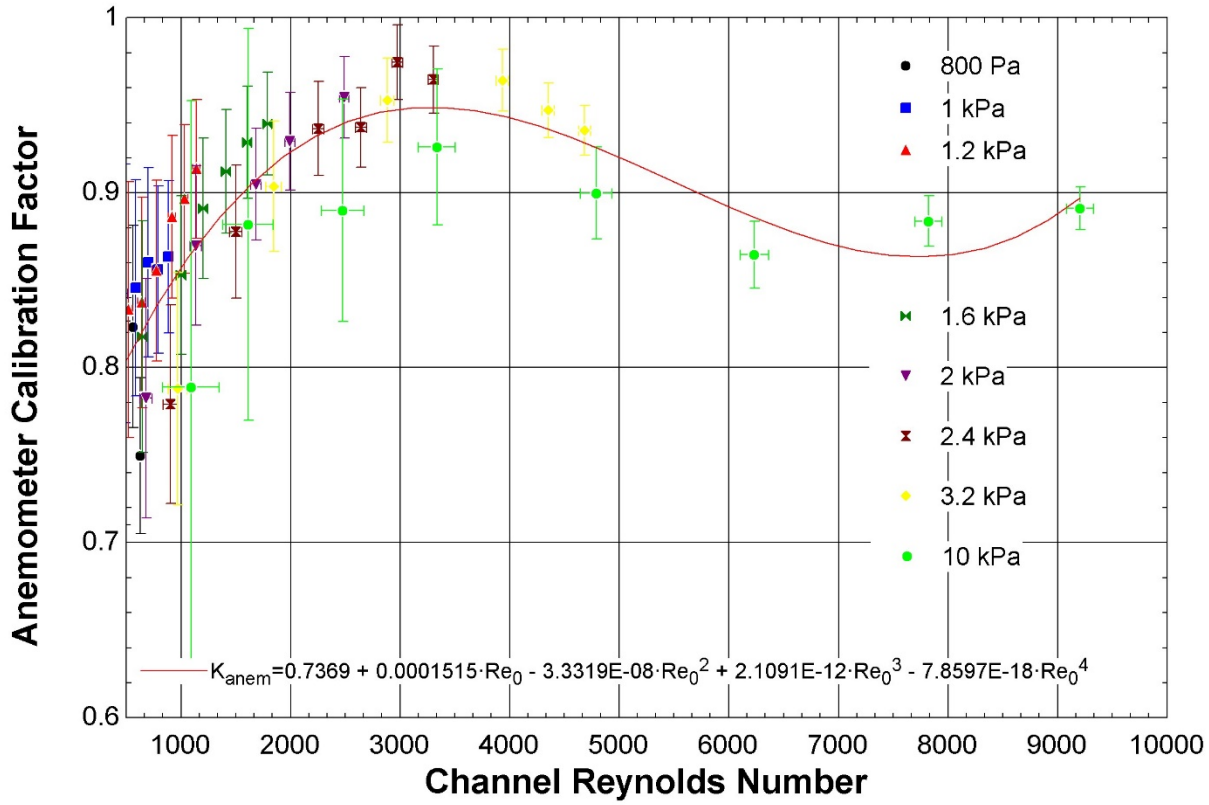

Figure 22: The anemometer calibration factor as a function of Reynolds number within the anemometer section

Data from each pressure follow approximately the same relationship with respect to the Reynolds number, suggesting that the fluid properties scaling approach was sound. A 4th order polynomial fit was generated and used to approximate K_{anem} when analyzing the experimental data. While all of the data at the lower pressures could have been approximated more simply, the flow at the higher pressures exhibited signs of transition in the laminar flowmeter, notably the decrease in K_{anem}, at higher Reynolds numbers. Importantly, while the maximum Reynolds number in the channel was approximately 9000, this equates to a Reynolds number in the laminar flowmeter tubes of only 2000. Therefore, the reduction in K_{anem} occurs at a tube Reynolds

number of roughly 750. The range of channel Reynolds numbers during experimental testing was 500-7000. The correlation shown above fit the data well across the range of Reynolds numbers studied herein. For 75% of the observed data points, the entire uncertainty range fell within 7.5% of the estimated value from the correlation. To determine the absolute uncertainty to apply to the K_{anem} approximation, the root mean square error is calculated to be 0.0607, considering both the maximum and minimum ranges of the error bars of each data point. The final expression for the estimated flow velocity at the anemometer location is then:

$$u_{exp} = K_{lfm}K_{anem}K_{peak}\left(\frac{C_{props,cal}}{C_{props,exp}}\right)^2 u_{anem} \quad (116)$$

3.7 Thermocouple Calibration

The four thermocouples used to measure the heat exchanger tube temperatures and the gas inlet and outlet temperatures were calibrated to reduce the associated error in the Nusselt number calculations. To reduce the risk of compromising the experimental heat exchanger, this step was performed after all experimental data was collected. First, a separate type K thermocouple was calibrated using a Fluke 9100S dry-well thermocouple calibrator at temperatures from 40-90°C. This thermocouple, the gas inlet and outlet thermocouples, and the entire heat exchanger with the tube thermocouples still inside were then submerged in a DI water bath on a hot plate and containing a stirrer bar. The tube thermocouples were left within the heat exchanger to more accurately replicate their conditions during operation and to avoid potential damage associated with removing them. Kaowool insulation was wrapped around the bath to reduce thermal gradients. Figure 23 shows the thermocouple calibration setup without

the Kaowool insulation. The bath was placed within the vacuum chamber so that each thermocouple could be plugged into the same leads that were used during data collection. The bath temperature was held at steady temperatures from 40-90°C based on the calibration thermocouple for 1 minute while thermocouple data were recorded at 1Hz. The mean and standard deviation of each thermocouple readout time series during the data collection at each condition was computed. Figure 24 shows plot of the mean difference between each experimental thermocouple and the calibration thermocouple vs the thermocouple reading at each set point. The error bars shown are the root-sum-square (RSS) of the sample standard deviations for the calibrated thermocouple and each experimental thermocouple.

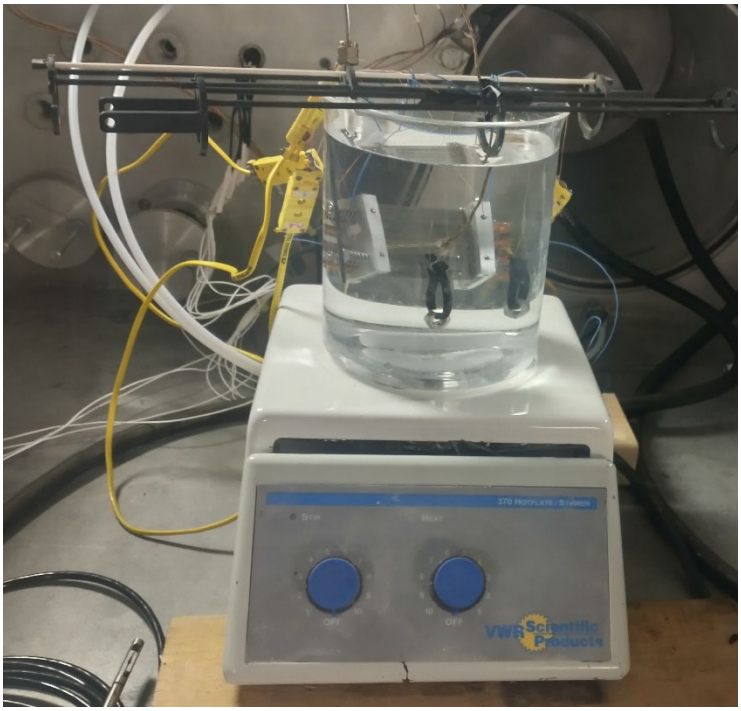

Figure 23: Thermocouple calibration setup. The Kaowool insulation is removed for visualization

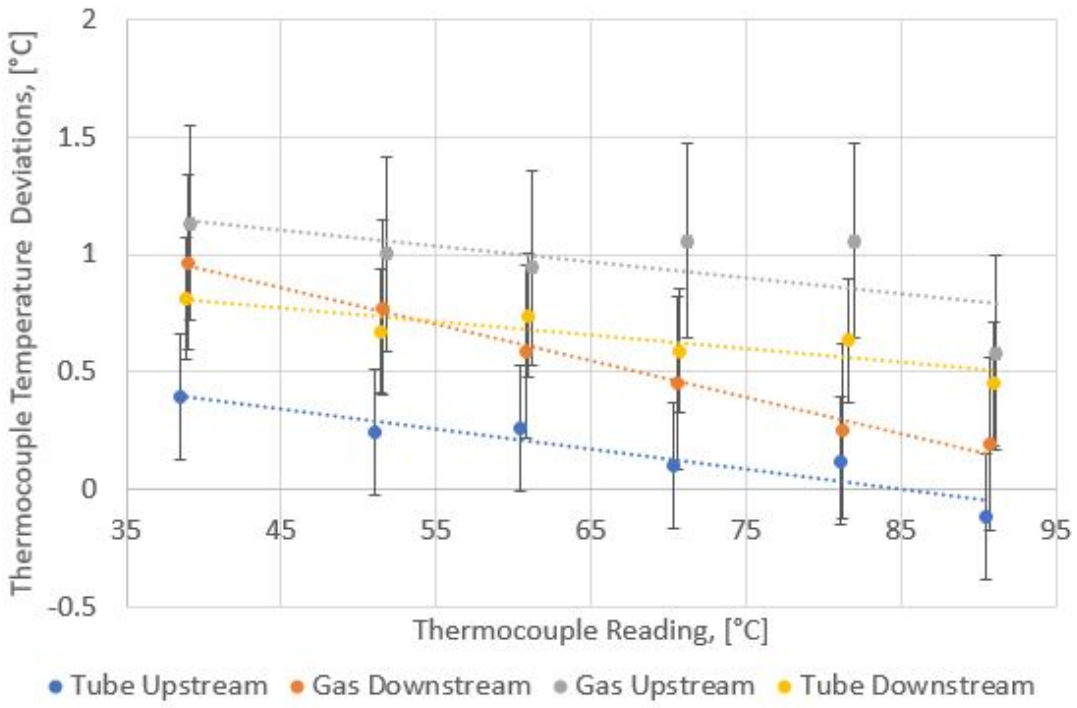

Figure 24: The difference between the experimental thermocouple readings and the calibrated thermocouple vs the experimental thermocouple reading is shown

Linear regressions for the difference between each experimental thermocouple mean reading and the calibrated thermocouple mean reading were derived. The regressions took the form:

$$\Delta T_i(T_{raw}) = a_i T_{raw,i} + b_i \quad (117)$$

Where ΔT_i is the offset for the ith thermocouple, $T_{raw,i}$ is the raw thermocouple reading for the ith thermocouple, and a_i and b_i are the regression constants. The uncertainty of the predicted temperature offset is calculated as the RSS of the average uncertainty of each measured temperature delta and the residual standard deviation of the regression. The regressions are then

applied to the measured temperatures in the experimental data to correct for the offsets inherent to the thermocouples in the following manner:

$$T_i = T_{raw,i} - \Delta T_i\left(T_{raw,i}\right)$$

(118)

3.8 Experimental Procedure

To collect the experimental heat exchanger performance data in axial flow, the test section is assembled in the axial flow configuration, described above. The same steps as described in the anemometer calibration section are followed to attain the target chamber pressure and composition. Data was collected in air at 2 kPa, 4 kPa, and 1 bar and in CO_2 at 1, 1.2, 2, 3.2, and 10 kPa. Once at the target condition, the fan is turned on and set to the lowest duty cycle that produces measureable flow on the anemometer. The heat exchanger power supply is then turned on. The current is limited to 150A to prevent damage to the conductors or feedthrough. The output voltage of the power supply is PID-controlled to maintain a target downstream tube temperature. Tube temperatures of 50, 100, and 150°C were investigated at each flowrate unless the current required to reach that temperature exceeded 150A which occurred in some cases at 10 kPa, or if a measureable flowrate was not achieved as the Euler number tended to increase at higher tube temperatures, limiting flowrate. After waiting for the temperatures to stabilize, data was collected on all sensors at 1 Hz for approximately 45 seconds. The fan duty cycle was then increased and the next data point was collected until the maximum fan speed was reached. The tube temperature was then increased to the next target temperature and the process repeated. These steps were repeated for all combinations of tube temperature,

ambient pressure, and composition within the experimental matrix, shown in Table 3. The minimum fan duty cycle was determined by increasing the duty cycle from 0.05 until a flowrate measurable by the anemometer was induced. This value decreased with increasing pressure.

Table 3: Experimental Parameters for the axial flow data collection

Parameter						
Ambient Pressure [Pa]	1000	1200	2000	3200	10000	1 bar
Minimum Downstream Tube Temperature, [K]	50	50	50	50	50	50
Maximum Downstream Tube Temperature, [K]	100	150	150	150	100	50
Minimum Fan Duty Cycle	0.999	0.6	0.4	0.4	0.05	0.05
Maximum Fan Duty Cycle	0.999	0.999	0.999	0.999	0.5	0.09
Composition 1	Air	Air	Air	Air	Air	Air
Composition 2	>98% CO_2	>98% CO_2	>98% CO_2	>98% CO_2	>98% CO_2	-

To collect heat exchanger performance data in vortical flow conditions, the test section is reconfigured by removing the flow straightener and the same data collection steps are followed. Only data in CO_2 was collected in this configuration. The test matrix is the same as that shown in Table 3. To quantify the vorticity of the flow, it is necessary to measure the rotational speed of the fan. This was not possible during the heat exchanger testing due to the lack of an appropriate data feedthrough. Therefore, following the heat exchanger testing and with the test section still in the vortical flow configuration, the DAQ system was reconfigured so that the fan tachometer output was transmitted through the feedthrough to an HP54616B oscilloscope. The fan was operated at each duty cycle and pressure in the vortical flow experimental matrix and the relationship between duty cycle and RPM was determined (there was no discernable effect of pressure). The fan diameter was also measured to determine the fan tip speed at a given RPM.

3.9 Experimental Results

3.9.1 Uncertainty Analysis

To analyze the experimental data, the mean and standard deviation of each set of sensor data for each condition are computed. For all experimental data sets, the uncertainties propagated through the calculations were the RSS of the uncertainty derived from the sensor specifications and twice the sample standard deviation for the dataset. For each sensor, the sensor specification significantly outweighed the dataset variance for each run as the system was very stable during operation. For the thermocouple data, the uncertainty is the RSS of twice the sample standard deviation for the dataset and the calculated uncertainty of ΔT_i for each thermocouple i. The ambient temperature thermocouple was not similarly calibrated and so the uncertainty is the standard uncertainty for K-type thermocouples in this temperature range of 2.2 K.

For the anemometer calibration factor K_{anem}, the uncertainty is derived by calculating the residual standard deviation of the dataset containing the endpoints of each error bar of the calibration data relative to the trendline shown in Figure 22. The absolute uncertainty of K_{anem} was 0.06072, or approximately 8%, and accounted for approximately 40% of the total uncertainty in the results below for most conditions. The uncertainty in the total heat exchanger resistance, $R_{e,tot}(\bar{T})$, is found in a similar manner. The absolute uncertainty of $R_{e,tot}(\bar{T})$ was 20.2 μΩ and did not significantly contribute to the overall uncertainty. Table 4 shows the value and uncertainty of each measurement, and K_{anem}, as well the fraction of the total uncertainty of each dimensionless value of interest; the Euler, number, Nusselt number, Reynolds number, and Knudsen number, for the axial flow, 1 kPa, $T_2 = 150\ °C$, $DC = 0.999$ case. This case was chosen

as it most closely represents the flow conditions during operation on Mars. By far the largest source of error in the two dimensionless measurements of heat exchanger performance, the Euler and Nusselt numbers, are the anemometer reading and the anemometer calibration factor. While the pressure drop measurements did not directly contribute to significant error in the derived parameters, roughly 27% of the error inherent in the anemometer calibration factor was due to the uncertainty in the pressure drop while performing the calibration because the pressure drops across the laminar flowmeter tended to be smaller than across the heat exchanger for similar conditions.

Table 4: Uncertainties of the measured parameters and their relative effects on the derived dimensionless parameters.

Parameter	Value	Uncertainty	% of σ_{Re}	% of σ_{Kn}	% of σ_{Eu}	% of σ_{Nu}
Pressure, [Pa]	996	9.98	0	95.94	0.1	0
Pressure Drop, [Pa]	14.81	0.564	0	0.31	1.5	0
HX Voltage, [V]	0.409	0.00133	0	0	0	2.64
Total HX Resistance, [μΩ]	720	20.2	0	0	0	2.56
Uncal. Anemometer Reading, [m/s]	0.144	0.0133	58.65	0	57.71	54.37
Anemometer cal. Factor, [-]	0.800	0.0667	39.70	0	39.06	36.80
Ambient Temperature, [K]	22.09	2.2	1.65	0	1.62	1.53
Gas Inlet Temperature, [K]	37.91	0.416	0	3.76	0	0.75
Gas Outlet Temperature, [K]	138.2	0.548	0	0	0	0
Upstream Tube Temperature, [K]	106.3	0.571	0	0	0	0.81
Downstream Tube Temperature, [K]	149.8	0.498	0	0	0	0.55

3.9.2 Data Processing Procedure

The mean sensor readings for each condition are imported into an EES [61] file to perform the data analysis. Because many of the velocity correction terms and correlations depend on the

Reynolds number which itself depends on the velocity, EES is used to solve the resulting implicit relationships simultaneously. The pressure at the heat exchanger inlet, used for calculating fluid properties in the heat exchanger, is estimated as the sum of the ambient pressure and the heat exchanger pressure drop while pressure drops in other parts of the test section are neglected. The thermocouple temperatures are adjusted based on the thermocouple calibration curves. The fluid properties are calculated at the test conditions using EES' built-in property functions and modelled as a real fluid. The gas velocity through the heat exchanger is calculated using the anemometer reading and the calibration procedure described in the previous section while considering the uncertainty from the anemometer reading and the correction factor calibration curves. The electrical resistivity of the tube material in each tube column are calculated based on the measured tube temperature and data on 304SS resistivity [55]. The header electrical resistance is calculated based on the tube temperature using the correlation described above and considering the uncertainty in the correlation and tube temperature. The power dissipated in each tube column can then be estimated as:

$$\dot{Q}_i = \frac{V_{tubes}^2}{R_{e,i}}; V_{tubes} = V_{HX}\frac{R_{e,i}}{R_{e,head} + R_{e,tubes}}$$

(119)

where the subscript i denotes the ith tube column. The Nusselt number on each tube column is then:

$$\overline{Nu}_{exp,i} = \frac{D_t}{k_{c,i}}\frac{\dot{Q}_i}{A_t\left(T_{wall,i} - T_{c,i}\right)}$$

(120)

where the tube wall surface temperature for the i[th] tube column, $T_{wall,i}$ is computed from the tube centerline temperature, the heat flux, and the thermal resistance associated with the tube wall. The bulk temperature used for the first row is the heat exchanger inlet temperature, $T_{c,in}$, and the bulk temperature for the second row is computed with an energy balance:

$$T_{c,2} = T_{c,in} + \frac{\dot{Q}_1}{\dot{m}_c c_{p,c}}.$$

(121)

The average Nusselt number for the entire heat exchanger is calculated as the average of the two columns, weighted by the heat flux, i.e.

$$\overline{Nu}_{exp} = \frac{\overline{Nu}_{exp,1}\dot{Q}_1 + \overline{Nu}_{exp,2}\dot{Q}_2}{\dot{Q}_1 + \dot{Q}_2}.$$

(122)

The Euler number is computed from the measured pressure drop across the heat exchanger and the measured velocity according to:

$$Eu_{exp} = \frac{\Delta P}{\frac{1}{2}\rho_{c,in} u_{max}^2 N_{rows}}$$

(123)

The Knudsen number is calculated for each data set using the heat exchanger inlet conditions. For the vortical flow data, the blade tip velocity is calculated from the fan speed and the blade radius. The ratio of the blade tip velocity to the gas axial velocity at the heat exchanger inlet, denoted as $u_{rat,b}$, is used to quantify the degree of vorticity in the flow into the heat exchanger.

$$u_{rat,b} = \frac{D_{fan}\omega_{fan}}{2u_{c,in}}$$

(124)

where $u_{c,in}$ is the gas velocity at the heat exchanger inlet. Assuming conservation of angular momentum, the tangential velocity of the flow at the heat exchanger inlet will equal the tangential at the fan blade because as the flow channel constricts from the fan face to the heat exchanger inlet, the angular speed of the gas will increase inversely with the radius. Therefore, this method can be used to estimate the vorticity at the heat exchanger inlet even though the tangential velocity is only measured at the fan.

3.9.3 Energy Conservation

To verify the validity of the anemometer calibration and data analysis approach, an energy balance on the heat exchanger is carried out for each run. By comparing the heat dissipated in the heat exchanger, calculated from the tube material resistivity and voltage drop, to the rate of energy deposited into the gas flowing through the heat exchanger, calculated from the flow rate and enthalpy change from inlet to outlet. Assuming minimal heat loss through the headers, these two values should be approximately equal provided that the gas flow rate values have been appropriately calibrated. Figure 25 shows the ratio of the rate of energy transfer to the CO_2, Q_{CO_2}, to the rate of electrical energy dissipated in the tubes, Q_{HX}, for both the axial CO_2 data and for the data taken in 1 bar air while Figure 26 shows the same for the vortical CO_2 data. In all cases, the ratio is near unity, suggesting that the anemometer calibration approach is valid and that heat loss through the header walls is minimal. The ratio tends to be above unity in the vortical cases and below unity in the axial cases which possibly indicates that the flows

downstream of the heat exchanger do not have spatially-uniform temperature distributions and these distributions are affected by the vorticity. However, as only one measurement was taken downstream of the flow at the channel center, this spatial distribution was not captured.

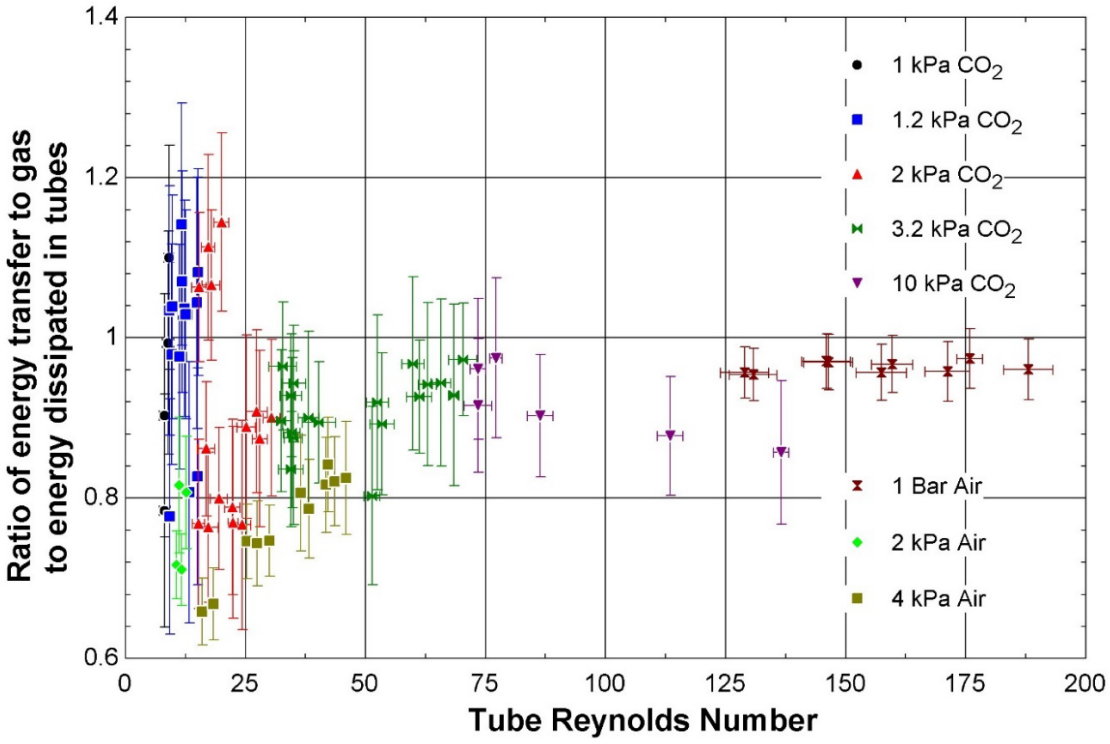

Figure 25: Energy balance for axial flow cases shows reasonable agreement between the heat dissipated by the tubes and the enthalpy rise of the gas flow

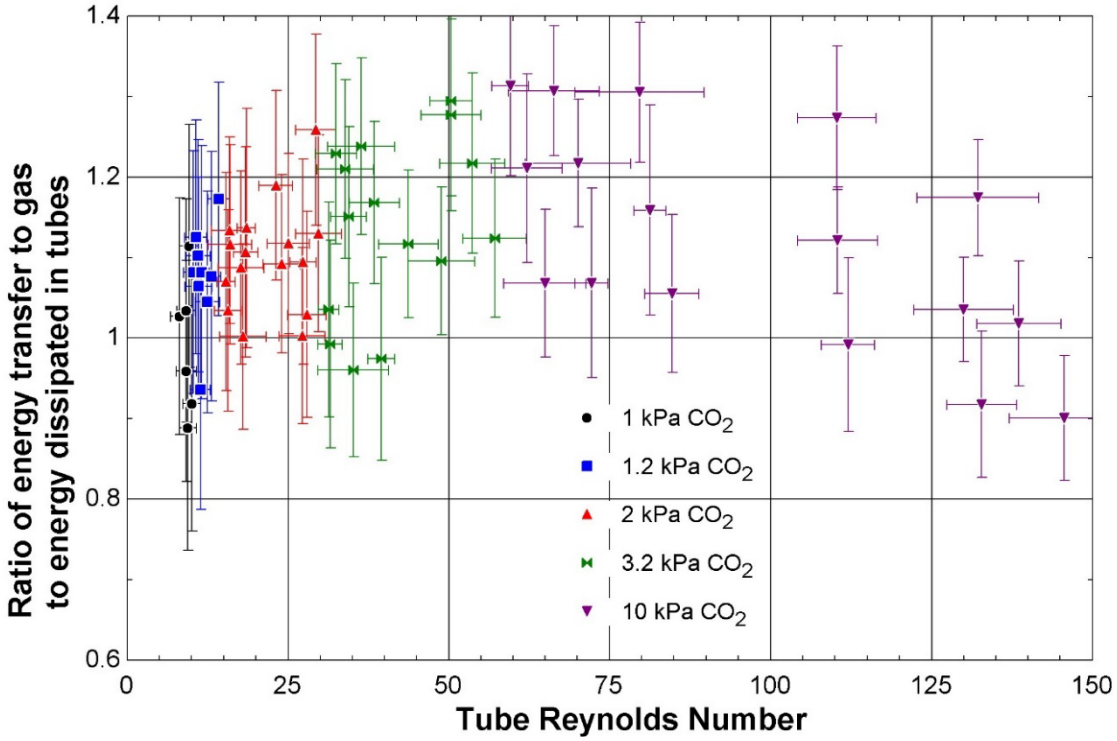

Figure 26: Energy balance for vortical flow cases also shows reasonable agreement

3.9.4 Pressure Drop

3.9.4.1 Axial Flow

Figure 27 plots the ratio of the measured pressure drop across the heat exchanger to the predicted pressure drop based on the HEDH correlation as a function of the Reynolds number for the axial flow, CO_2 test data and for 1 bar air. For Reynolds numbers above 75, the measured pressure drop matches the predicted pressure drop fairly well. As expected, the data taken using 1 bar air closely matches the correlation. For Reynolds numbers below 75 and above 7, the minimum Reynolds number range of the HEDH correlation [29], the measured pressure drop significantly exceeds the value predicted by the correlation, reaching 3 times the predicted value for the lowest Reynolds values. The correlation only provided entry length effect approximations for Reynolds numbers above 100, and in implementing the correlation, the entry length effect

correction factor for $Re_t = 100$ was used for all cases with a Reynolds number below 100. As the experimental heat exchanger consists of only 2 rows, entry effects may play a significant role in the pressure drop.

Figure 28 plots the same pressure drop ratio as a function of the Knudsen number. To separate out the effects of Reynolds, the data are binned by the Reynolds number instead of by the pressure. Within each range of Reynolds number, there appears to be a very slight positive effect of the Knudsen number on the pressure drop. As expected, the data in 1 bar air closely matches the correlation.

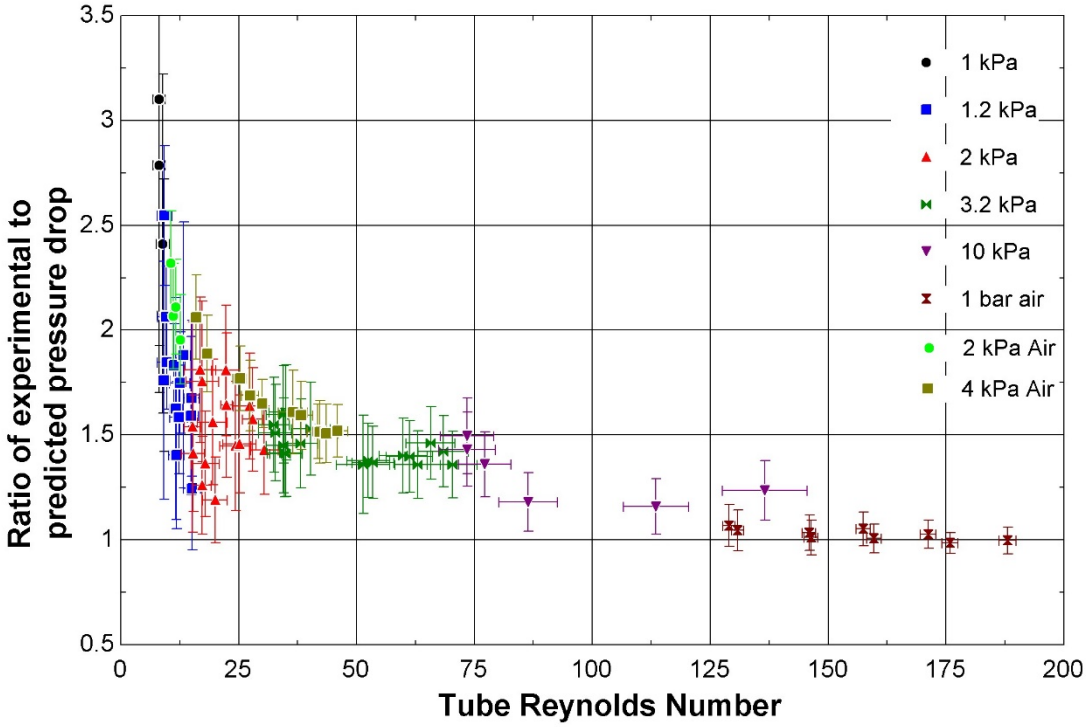

Figure 27: The measured pressure drop exceeds the predicted pressure drop at low Reynolds numbers

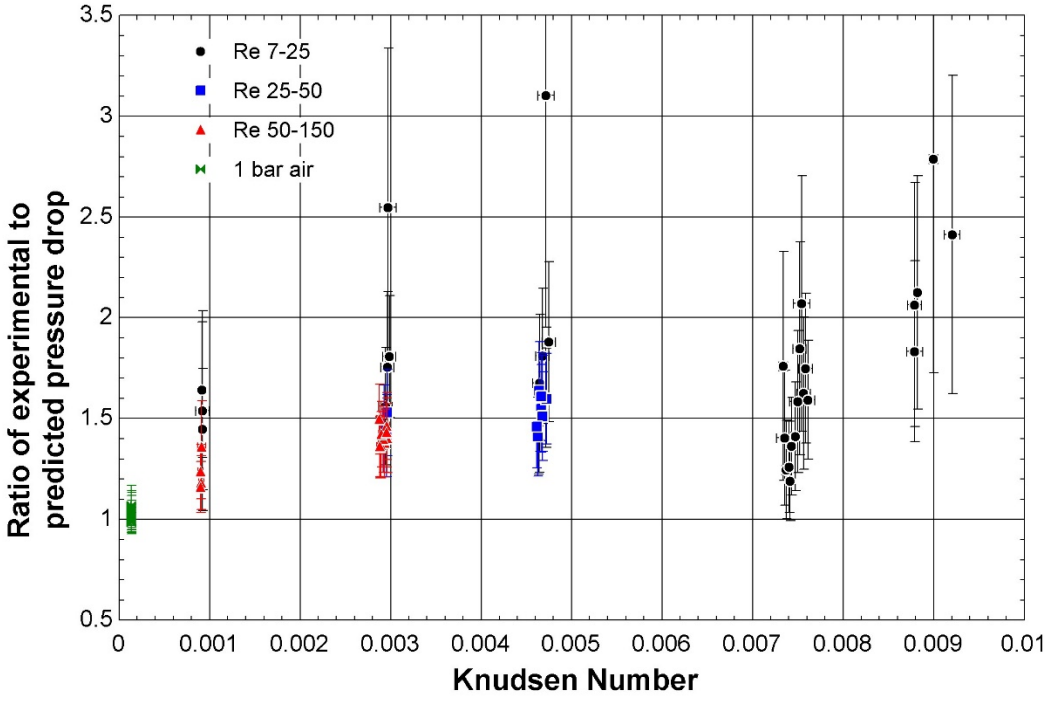

Figure 28: The ratio of measured-to-predicted pressure drop does not appear to depend on Knudsen number in this range

3.9.4.2 Vortical Flow

Figure 29 plots the Euler number in vortical and axial flow CO_2 as a function of the Reynolds number and illustrates the effect of vorticity. It is apparent that the presence of vorticity in the flow increases the pressure drop across the heat exchanger. To quantify the effect of the vorticity as well as the impact of the Reynolds and Knudsen numbers, a nonlinear regression was performed to determine the best-fit approximation of the experimental Euler number in terms of the vorticity, the Reynolds number, the Knudsen number, and the existing HEDH correlation. A power-law fit of the form

$$Eu_{est} = Eu_{HEDH}\, C_1 Re_t^{C_2} Kn^{C_3} \left(1 + u_{rat,b}\right)^{C_4}$$

(125)

is fit to both the axial and vortical data. For the axial data the blade velocity ratio is set to zero. The best-fit correlation is:

$$Eu_{est} = Eu_{HEDH}\, 3.2326 Re_t^{-0.2084} Kn^{0.0066} \left(1 + u_{rat,b}\right)^{0.0943}.$$

(126)

As expected, there is only a very weak correlation with the Knudsen number in the regime studied. The increasing velocity ratio increases the Euler number relative to the HEDH model while the increasing Reynolds number decreases it. Figure 30 plots the measured pressure drop against the estimated pressure drop using the above correlation for each axial and vortical CO_2 flow case. The correlation matches the experimental data within 10% in 73% of cases and within 20% in 89% of cases across the conditions studied. The range of experimental conditions over which this correlation is valid is Reynolds numbers from 7-150, Knudsen numbers from 0.0009-0.009, and blade velocity ratios of 0 and from 3-13.5. The maximum blade tip Mach number was 0.447. At the highest blade velocity ratios studied, this correlation predicts, and the data reflects, an Euler number increase of 28% over a purely axial case, closely matching the deviation measured by Moore et al. [31] in a finned tube bank at much higher Reynolds numbers and lower Knudsen numbers.

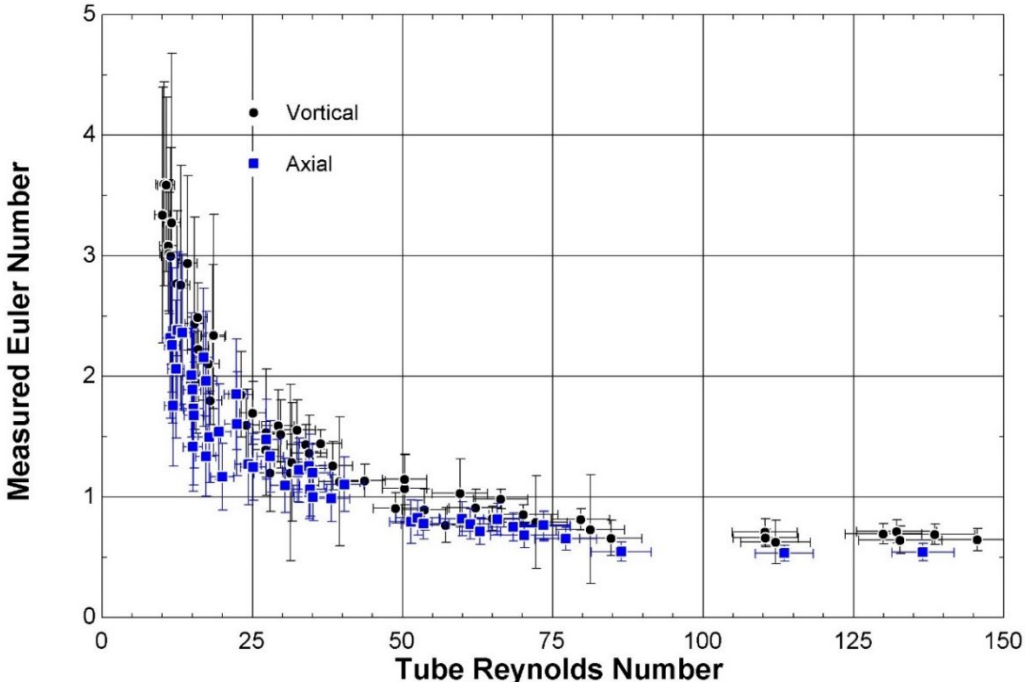

Figure 29: The Euler numbers in the vortical flow cases exceed those in the axial cases for a given Reynolds number

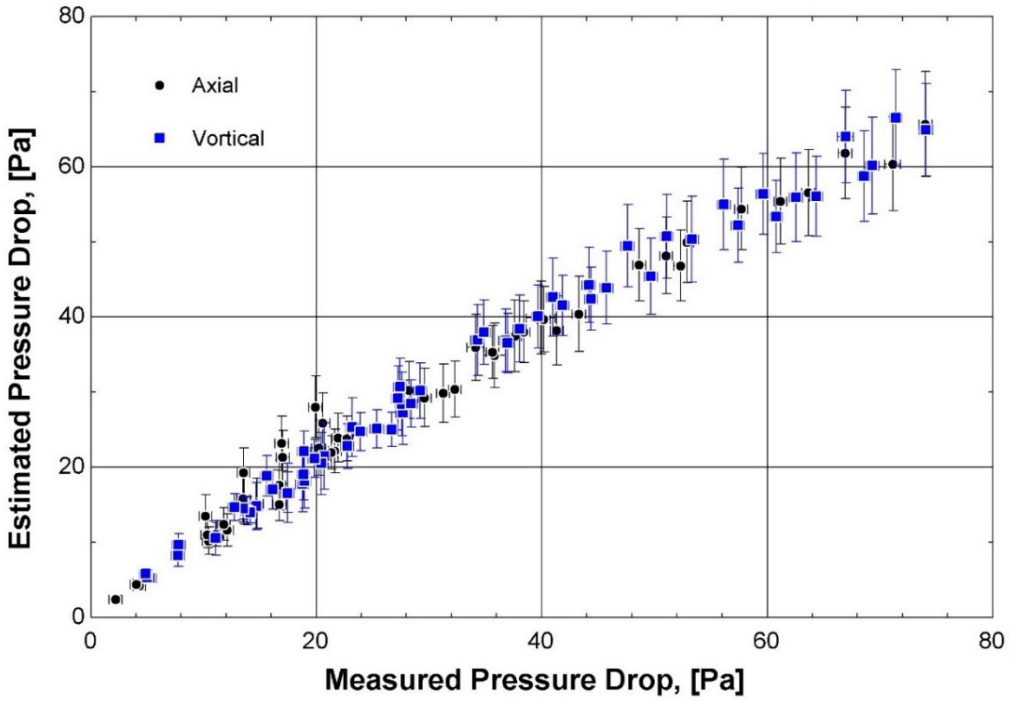

Figure 30: The derived correlation closely matches the axial and vortical flow measured pressure drops

3.9.5 Nusselt Number

3.9.5.1 Axial Flow

Figure 31 illustrates the ratio of the measured Nusselt number to the Nusselt number predicted by the Tariq et al. [30] correlation vs the Reynolds number for axial flows of both CO_2 and air at a range of pressures. For the range of Reynolds numbers studied here, there is a slight negative trend with respect to Reynolds number at low Reynolds numbers, but the correlation seems to agree reasonably well with the experimental data, with the largest deviation from the predicted value being approximately 70% at the minimum Reynolds number (where uncertainty in the data is large), and all values above a Reynolds number of 30 being within 25% of the correlation.

Figure 32 plots the same Nusselt number ratio vs the Knudsen number, binned by Reynolds number. Again for the Knudsen number range studied, there is no clear trend in the Nusselt number ratio beyond what is predicted by the existing correlation, although at lower Knudsen numbers, the low-Reynolds-number cases slightly exceed the correlation while at higher Knudsen numbers they more closely match the prediction. As the Tariq correlation already predicts a slight decrease in the Nusselt number with increasing Knudsen number, these data seem to affirm this effect in tube banks. Whereas the Tariq et al. correlation was developed purely from numerical modelling of flow through a porous medium, this study demonstrates that it accurately predicts the Nusselt number in low-Reynolds, low-to-moderate Knudsen number tube banks.

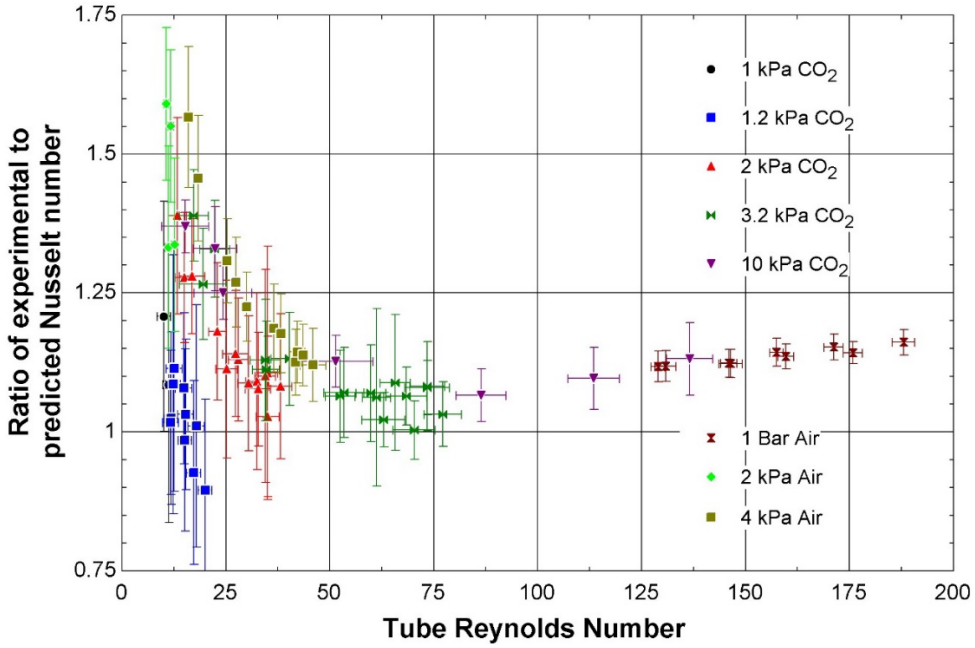

Figure 31: The measured Nusselt number slightly exceeds the predicted Nusselt number at low Reynolds numbers

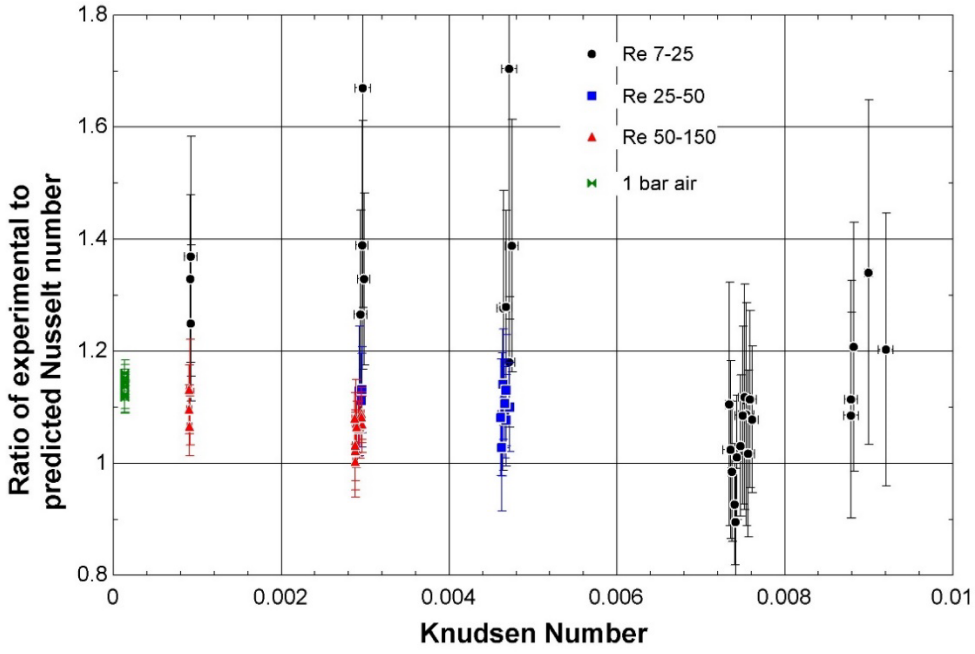

Figure 32: The measured-to-expected Nusselt number ratio does not appear to depend strongly on Knudsen number in this range

3.9.5.2 Vortical Flow

Figure 33 plots the Nusselt number in vortical and axial flow CO_2 vs Reynolds number and Knudsen number to illustrate the effect of vorticity. It is apparent that the presence of vorticity in the flow decreases the Nusselt number within the heat exchanger. Interestingly, the vortical data is very well-predicted by the Tariq et al. correlation, with all measured values within 25% of the predicted values. Following the same approach as for the pressure drop, a correlation for the Nusselt number with respect to the Reynolds number, the vorticity, the Knudsen number, and the value predicted by the Tariq et al. correlation is derived and is given as

$$Nu_{est} = Nu_{Tariq} 0.9757 Re_t^{-0.1132} Kn^{-0.0937} \left(1 + u_{rat,b}\right)^{-0.0434}. \quad (127)$$

This correlation differs by no more than 12% from the Tariq et al. correlation over the range of conditions tested here and shows a very weak dependence on the vorticity, therefore the Tariq et al. correlation without modification exhibits reasonable agreement with the experimental data and is suitable for predicting the Nusselt number for vortical as well as axial flow. Figure 34 plots the Nusselt number values predicted by this correlation vs the experimentally-measured values. The correlation predicts the experimental result within 10% for 84% of cases and within 20% for 97% of cases over the investigated range. That the vorticity does not significantly affect the Nusselt number matches the observations of Moore et al. [31] of finned tubes at much higher Reynolds numbers.

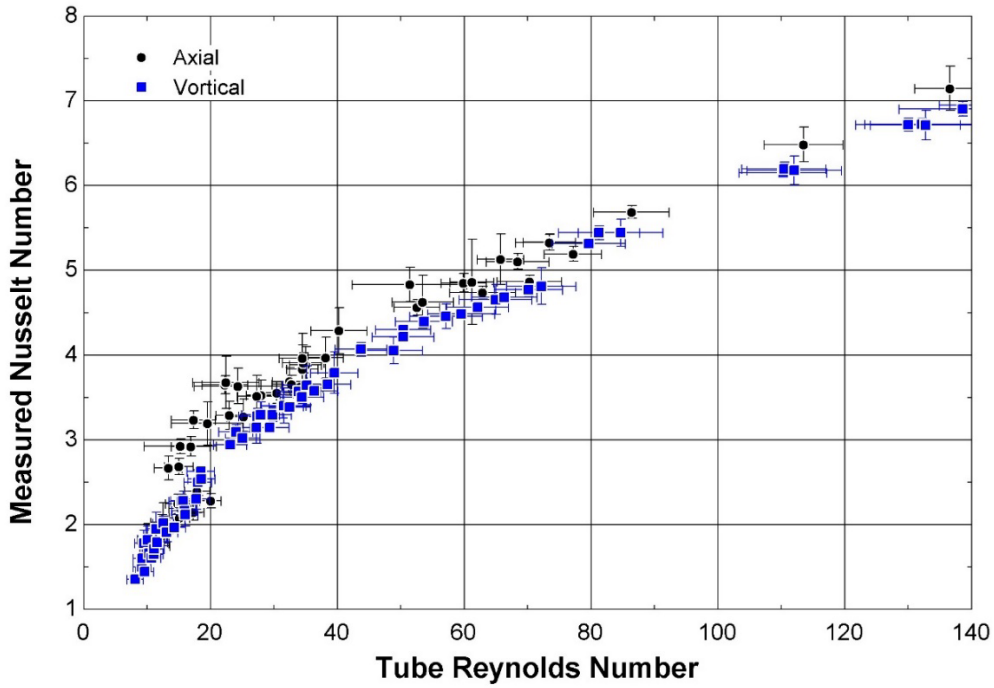

Figure 33: The vortical flow cases tend to result in lower Nusselt numbers than the axial flow cases for a given Reynolds number

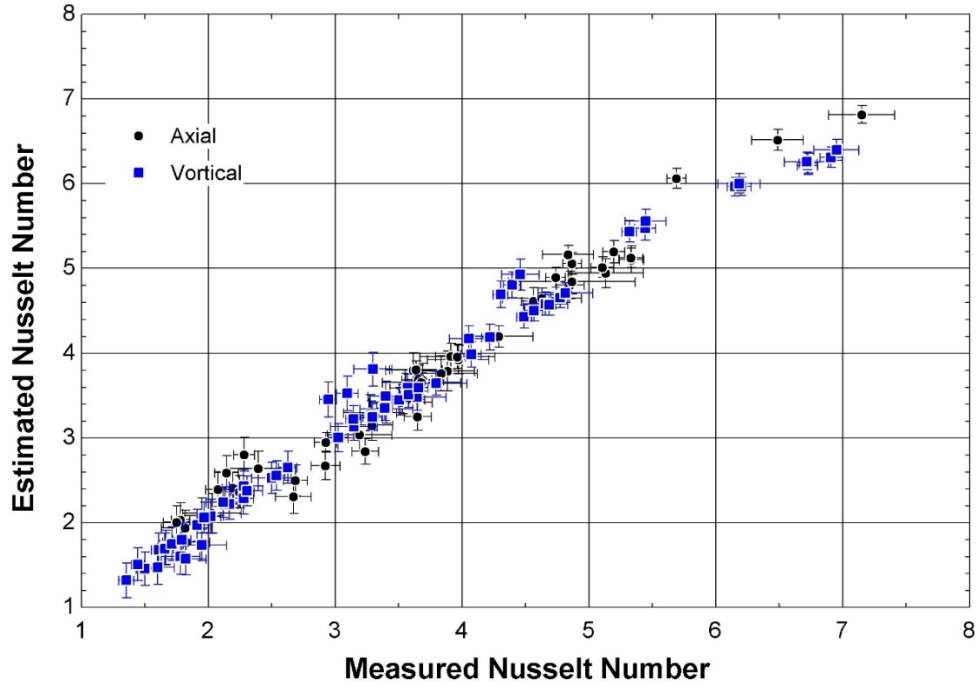

Figure 34: The derived Nusselt number correlation accurately predicts the axial and vortical flow Nusselt number

4. Modelling Results

The modified HEDH Euler number correlation derived from the experimental data, shown in Equation 126 above, is incorporated into the analytical heat exchanger model described in Section 2.1 above. The unmodified Tariq et al. Nusselt number correlation is used instead of the modified version, shown in Equation 127 above, because at the optimal operating conditions and geometries described below, the two correlations differ by less than 5% and because coupling the Nusselt number, which is used to solve for the gas velocity as described in Section 2.1.3, to the fan speed and thus to the pressure drop and fan efficiency calculations described in Sections 2.1.4 and 2.1.5 respectively, would significantly increase the computational demand of the model.

4.1 Typical features of Mars HX

The heat exchanger model is run over a wide variety of Martian conditions, tube configurations and materials, and thermal loads and some general observations are reported here. A defining aspect of the optimal heat exchanger design across all input conditions is a low atmosphere-side pressure drop. While the total system mass is sensitive to tube length and diameter, fin pitch, and the number of tubes as these parameters directly contribute to the heat exchanger mass, the required fan power increases rapidly at high pressure drops and flow rates and this increase in fan power increases the total mass because of the larger motor required and the power mass penalty. Features that contribute to a high pressure loss are a small fin pitch, a large number of tube rows, and a high flow velocity which can result from a low total surface area that then requires a high average heat transfer coefficient. Figure 35 demonstrates the

sensitivity of the optimal mass to the HX length, height, number of tube columns, and fan pressure rise. It can be seen that as the rejected heat power increases, the overall HX height and length both increase, the pressure drop stays below 15 Pa, and the optimal mass rises linearly. However once the height and length reach their upper limits, the fan pressure rise increases sharply as the flow velocity and the number of tube rows increase. Consequently the mass rises significantly due to the increased required fan power and increased tube mass. Therefore, all of the optimal geometries determined for various input conditions tended to have very few tube rows and a large number of small tubes to maximize surface area while minimizing pressure drop. It is important to note that as the increase in required pressure drop is caused by reaching the HX size constraints, if more than 250 kW of heat rejection are required, multiple heat exchangers

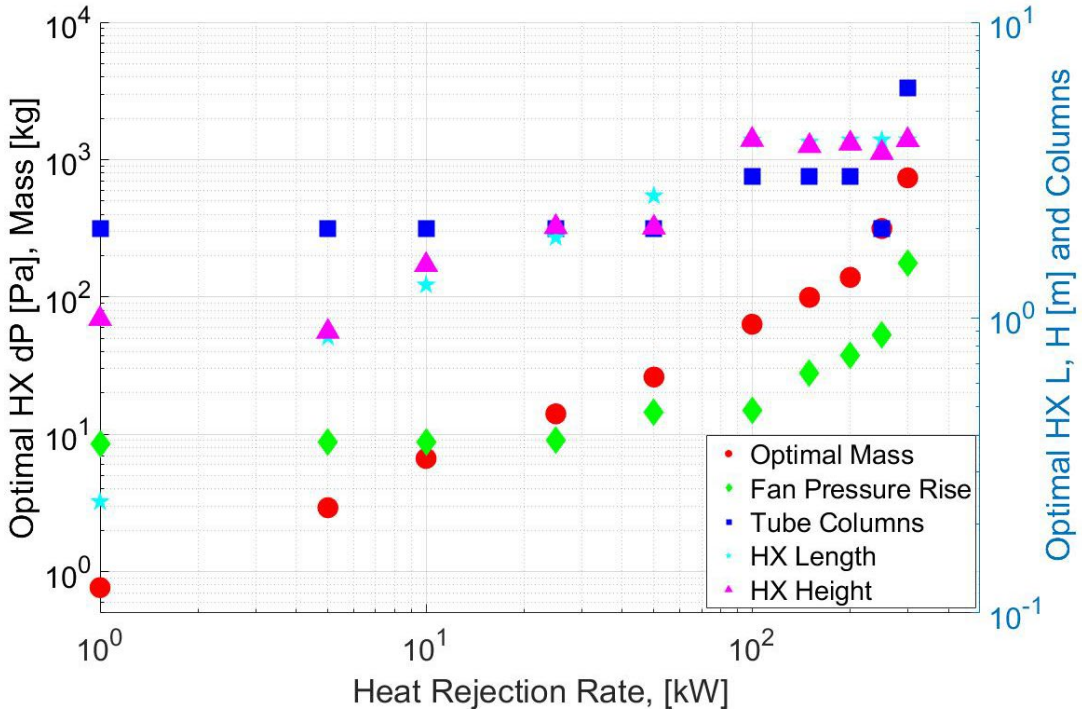

Figure 35: Variation of the optimal heat exchanger geometry, mass, and pressure drop with rejected heat power for an Aluminum heat exchanger at conditions optimal for FSPS heat rejection, described below.

could be deployed and the heat rejection load split among them, which would also increase redundancy in the case of heat exchanger damage.

When aluminum is the heat exchanger material, most optimal geometries had fin pitches of approximately 2-4 mm, but for the other materials nearly all cases had no fins. As shown by the convergence testing, the model consistently finds the same optimal mass for a given case. However, due to the tolerances associated with the velocity-finding routine, and because the fin density does not seem to strongly affect the optimal mass, running the model for the same input conditions sometimes resulted in geometries with different fin pitches but essentially the same mass. This behavior makes it difficult to determine the optimal fin pitch for the aluminum heat exchanger; all other materials optimize to a bare tube bank. This results from the fins' lower heat transfer coefficient in the low Reynolds number flow and the optimization for mass instead of volume. As the fan pressure rise strongly affects the optimal mass, the mass increase resulting from the increased pressure drop caused by the fins outweighs the potential mass savings from the added heat transfer area reducing the required tube length. Furthermore, because the heat exchanger effectiveness is already fairly high without fins, adding them does not significantly decrease the required CO_2 flow rate through the heat exchanger. This behavior is noticeably different than typical heat exchanger design in standard atmospheric conditions where pressure drop is less of a concern. These heat exchangers tend to have many tube columns and many closely spaced fins to minimize cross-sectional area. To confirm this observation, the geometries and masses of 4 steel heat exchangers at low pressure optimized for a range of power levels are compared to those of an 800 kW heat exchanger operating in 100 kPa CO_2. The results are shown in Table 5; note that the length and height of each heat exchanger is limited to 1 m. The heat

exchanger optimized for 100 kPa has 10 tube columns and a fin pitch of 0.36 mm which corresponds to a typical finned-tube compact heat exchanger design. The Mars-optimal heat exchangers all have small tube diameters, large fin pitches and few rows, likely due to the greater sensitivity to pressure drop and the lower heat transfer coefficients necessitating more tube surface area. Figure 36 illustrates the typical sizes of the optimal HX geometries given below with humans for scale.

Table 5: Comparison of optimal HX geometries for various conditions and heat loads for a steel HX

Parameter	**Value**				
Atmospheric Pressure [kPa]	0.6	0.6	0.6	0.6	100
Heat Load [kW]	1	10	100	200	800
Inlet Temperature [K]	402	402	402	402	402
Outlet Temperature [K]	334	334	334	334	334
Length [mm]	198	1241	3796	3999	985
Tube Rows	844	476	1363	1461	318
Tube Diameter [mm]	0.603	1.427	1.467	1.350	1.50
Height [mm]	1017	1358	3998	3946	948
Tube Columns	2	2	2	2	10
Fin Pitch [mm]	1908	234	514	2.226	0.43
Fan Power [W]	42.03	410.9	3977	14694	10465
Optimal HX Mass [kg]	0.931	8.278	80.781	203.686	195.7

Figure 37 shows the optimal heat exchanger mass for each combination of tube configuration (pitch to diameter ratio and in-line or staggered) for a steel heat exchanger as a function of rejected heat. For all cases the staggered, $R_p = 2$ configuration resulted in the lowest mass as this tended to produce the lowest pressure drops while still allowing adequate heat transfer. This configuration is used in all results going forward.

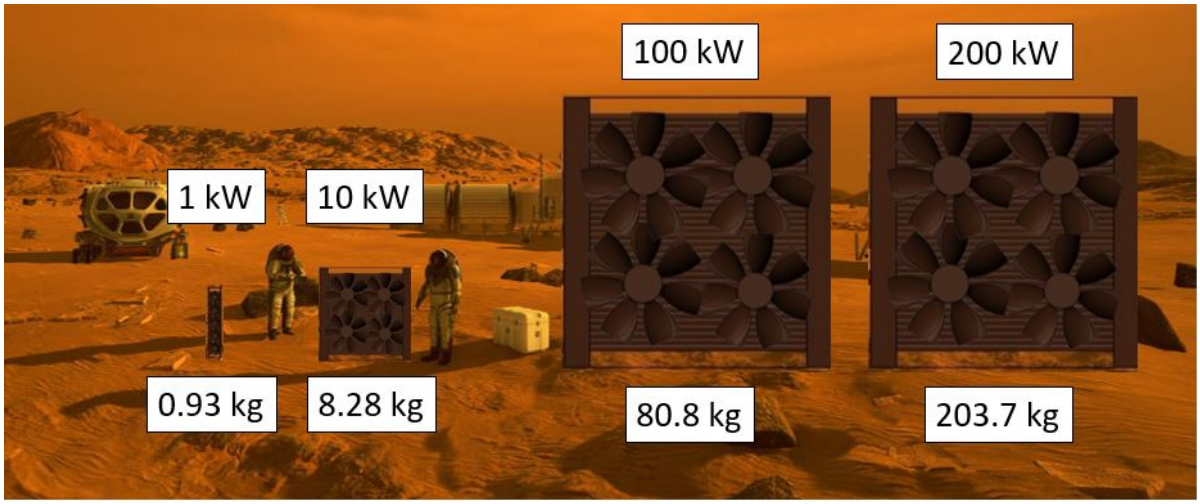

Figure 36: Illustration of various capacity heat exchangers on Mars with humans for scale. The 100 kW and 200 kW heat exchangers are the maximum geometrical size allowed by the modelling, the increased mass of the latter is due to the higher required fan power.

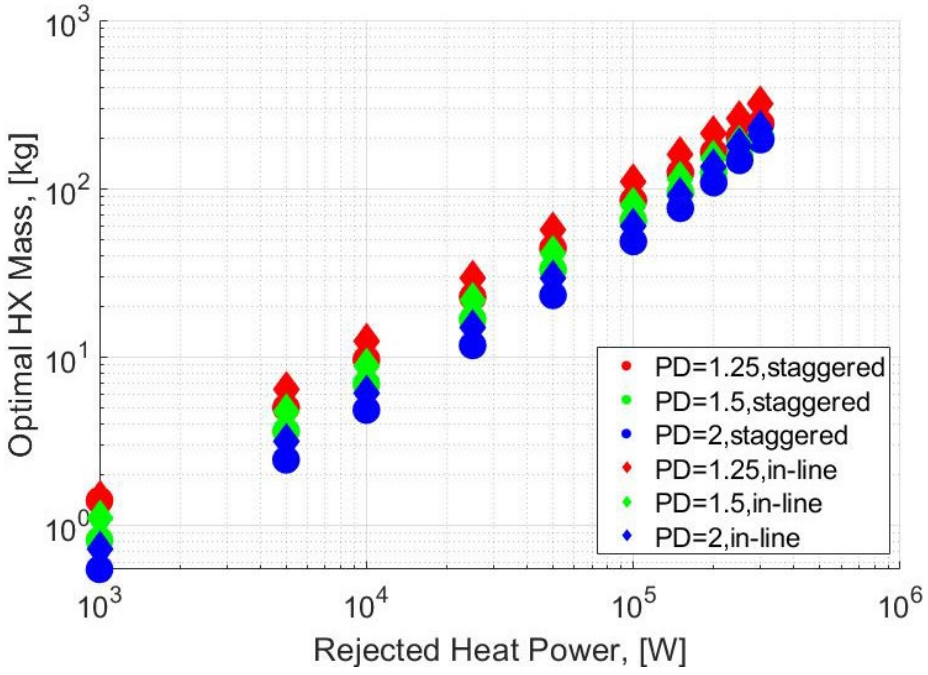

Figure 37: Comparison of the optimal HX mass using various tube parameters for a Steel, 100 kW HX. PD refers to the pitch-to-diameter ratio

The effect of coolant inlet temperature is shown in Figure 38 for each heat exchanger material. At temperatures below 550 K aluminum results in the lowest optimal mass while at higher temperatures, where aluminum's yield stress decreases resulting in thicker tube walls and more massive tubes, titanium becomes the lowest-mass material. As overall cycle thermal efficiency decreases with increasing heat rejection temperature, an FSPS optimized to use a convective HX for heat rejection tended to have a low rejection temperature around 400 K, as discussed below, therefore aluminum will result in the lowest-mass HX for these systems.

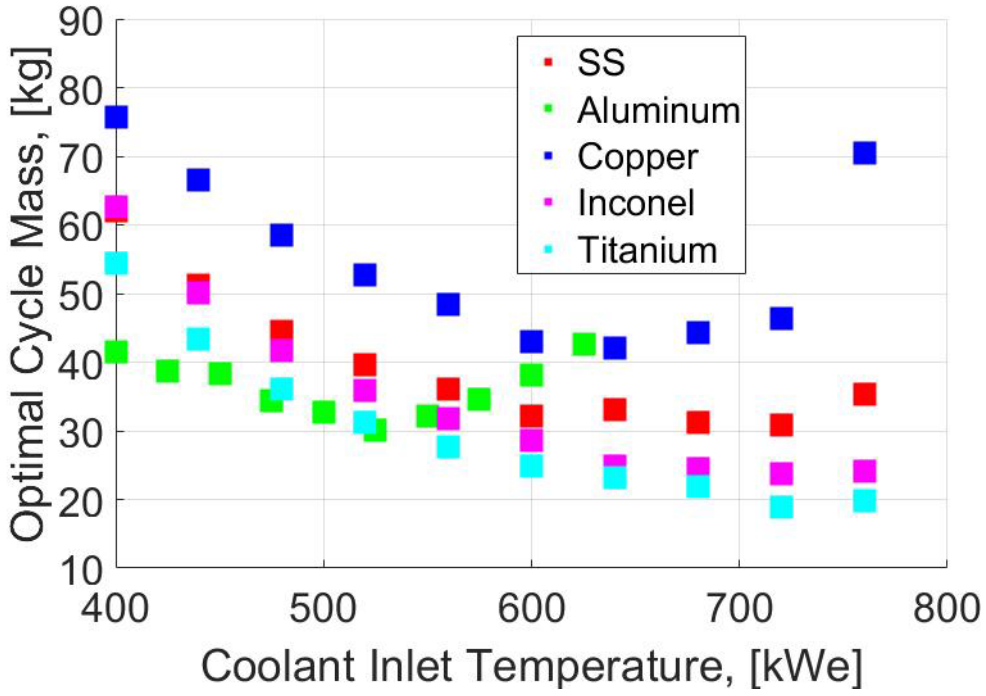

Figure 38: Optimal HX mass vs coolant inlet temperature for various tube materials. For each case the coolant temperature drop is 100 K and the rejected power is 100 kW.

For high-temperature applications such as cooling for high-temperature processes, titanium may be the preferred material. Although not shown in the figure, using helium as the high-pressure fluid decreases the optimal mass compared to sCO_2 by less than 1% because the dominant

thermal resistance is on the environment-side, although using helium as the heat transfer fluid in the power block may lower the optimal cycle pressure, leading to thinner heat exchanger walls.

4.2 Effect of ambient conditions

The effect of ambient pressure and temperature on the optimal HX mass is shown in Figure 39. This plot shows the optimal mass of an aluminum heat exchanger optimized to reject 100 kW at the given pressure and temperature. As the pressure decreases, the Nusselt number tends to decrease requiring more surface area and a higher flow velocity. However, even at 400 Pa, a pressure corresponding to an altitude of 5 km above the datum, significantly above NASA's feasible landing site altitude requirement [2], adequate cooling performance is achieved with a low system mass. While future bases at high elevation may require radiators due to the thin air,

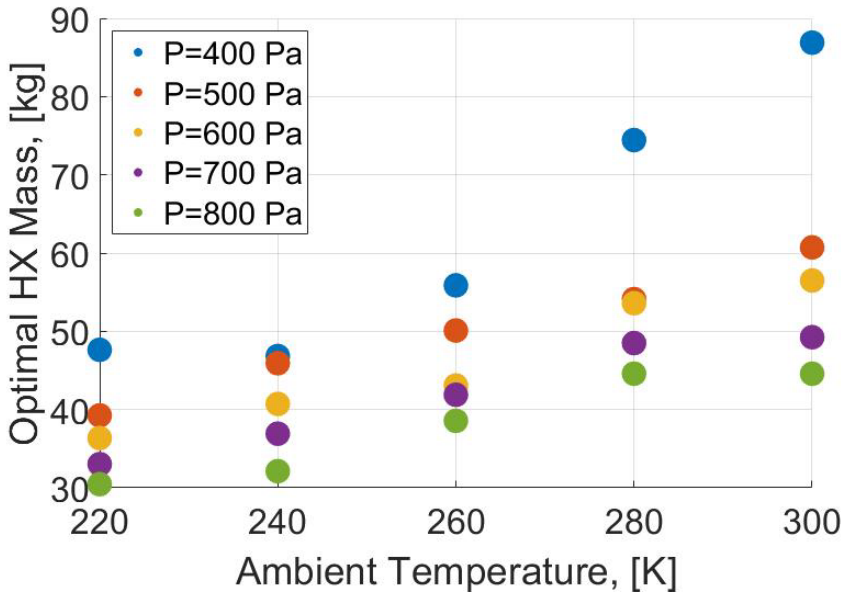

Figure 39: Optimal HX mass vs ambient temperature and pressure for a 100 kW Aluminum HX operating at a coolant inlet and exit temperature of 450K and 375 K respectively. The optimal mass decreases with increasing pressure and decreasing temperature

the convective HX is capable of providing sufficient cooling at the range of feasible initial landing site altitudes with a lower mass than a radiator.

4.3 Power cycle results

4.3.1 Comparisons to Radiator cycle

The Sondelski model is used to estimate the total FSPS cycle mass over a range of desired output powers while using a radiator and while using heat exchangers made of steel, aluminum, and titanium, which are shown in Figure 40. The turbine inlet temperature is 900 K, the ambient conditions for the heat exchanger are 600 Pa and 260 K, and the background sky temperature for the radiator is 200 K. Because the fan motor mass is set by the required fan power, it was decided to optimize the cycle for the peak daily temperature instead of the mean temperature as the fan will have to work harder at higher ambient temperatures due to the higher required flow rate to

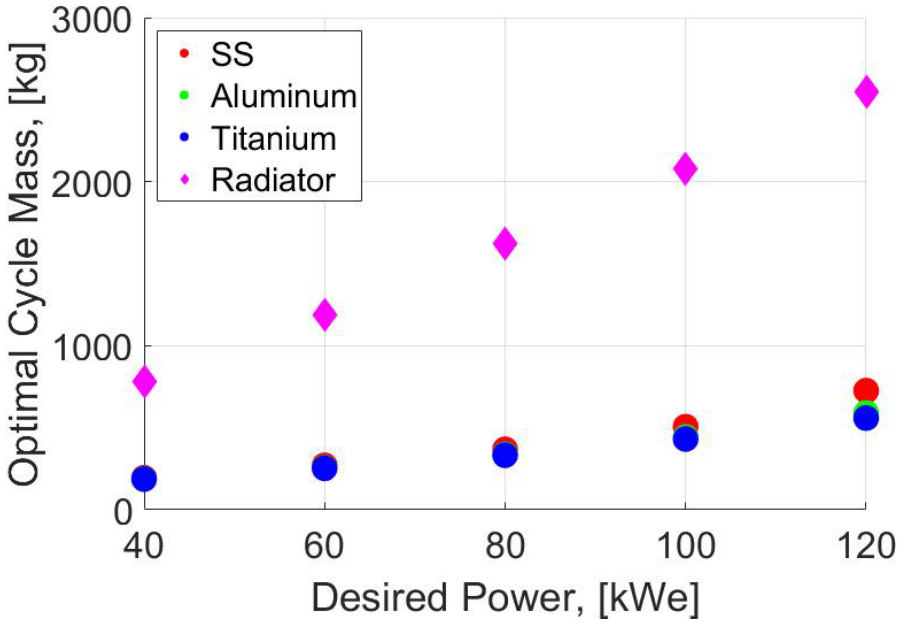

Figure 40: Optimal cycle masses for a range of desired powers at ambient conditions of 260K, 600 Pa. The heat exchanger outperforms the radiator in each case.

maintain steady cooling conditions for the reactor. For all heat exchanger materials, significant mass savings are predicted when compared to the radiatively-cooled system, but the aluminum heat exchanger resulted in the lowest mass.

4.3.2 HX features of optimized cycle

Table 6 compares key performance and mass parameters of the optimal 40 kWe cycle for both a radiator and an aluminum heat exchanger. The use of the heat exchanger reduces optimal cycle mass by 78% from 782 kg to 175 kg, both by reducing the waste heat rejection system mass and by reducing the optimal heat rejection temperature which increases thermal efficiency and reduces the required recuperator mass.

Table 6: Comparison of the optimal cycle parameters for a radiatively- and convectively-cooled 40 kWe FSPS

Parameter	Radiator	Convective HX
Mass Flow Rate [kg/s]	1.14	0.740
Heat Rejection Inlet Temperature [K]	495	412
Minimum Cycle Temperature [K]	414	341
Cycle Efficiency	0.27	0.341
Recuperator Mass [kg]	111	36.0
Radiator/Convective HX Mass [kg]	570	37.0
Reactor Mass [kg]	101	102.2
Total Cycle Mass [kg]	782	175.2
Heat Rejection Area [m^2]	84	11.76

The heat exchanger cycle has a 73 K lower minimum cycle temperature, increasing thermal efficiency from 27% to 34%. The heat exchanger mass is significantly less than the

radiator, and the frontal area of the heat exchanger is 86% less than the required radiator surface area, reducing the need for complex deployment mechanisms. The geometric and performance parameters of the optimal heat exchanger are given in Table 7. The required fan power in this case is approximately 1.806 kWe, the atmosphere-side pressure loss is approximately 8.07 Pa, and the gas velocity through the heat exchanger is 11.39 m/s.

Table 7: Geometric and performance parameters of the heat exchanger for the optimal FSPS cycle given above

Parameter	Value
Heat Load [kW]	75.5
High-Pressure Inlet Temperature [K]	412
High-Pressure Outlet Temperature [K]	341
Atmosphere-side Outlet Temperature [K]	322
Atmosphere-side Mass Flow Rate [kg/s]	1.46
Length [mm]	2972
Tube Rows	954
Tube Diameter [mm]	2.07
Height [mm]	3955
Tube Columns	2
Atmosphere-side Pressure Drop [Pa]	8.07
Atmosphere-side Axial Velocity [m/s]	11.39
Fan Power [W]	1806
Tube Reynolds Number	35.4
Fan Velocity Ratio	6.00
Knudsen Number	0.00465

4.3.3 Response to varying ambient conditions

Figure 41 shows the required fan power for an optimized 40 kWe FSPS operating at 260 K, 600 Pa ambient conditions when varying the ambient conditions across a range of expected conditions throughout a Martian year. The required fan power stays below 10% of the output power except at 280 K ambient conditions. It may be preferable to reduce the reactor power output during periods of extremely high ambient temperature rather than oversize the fan motor for these conditions as they are expected to occur infrequently. As the fan is sized for 260 K ambient conditions, at times of lower temperatures less fan power would be required, or the reactor could be run at a higher power output or a higher thermal efficiency depending on the mission requirements.

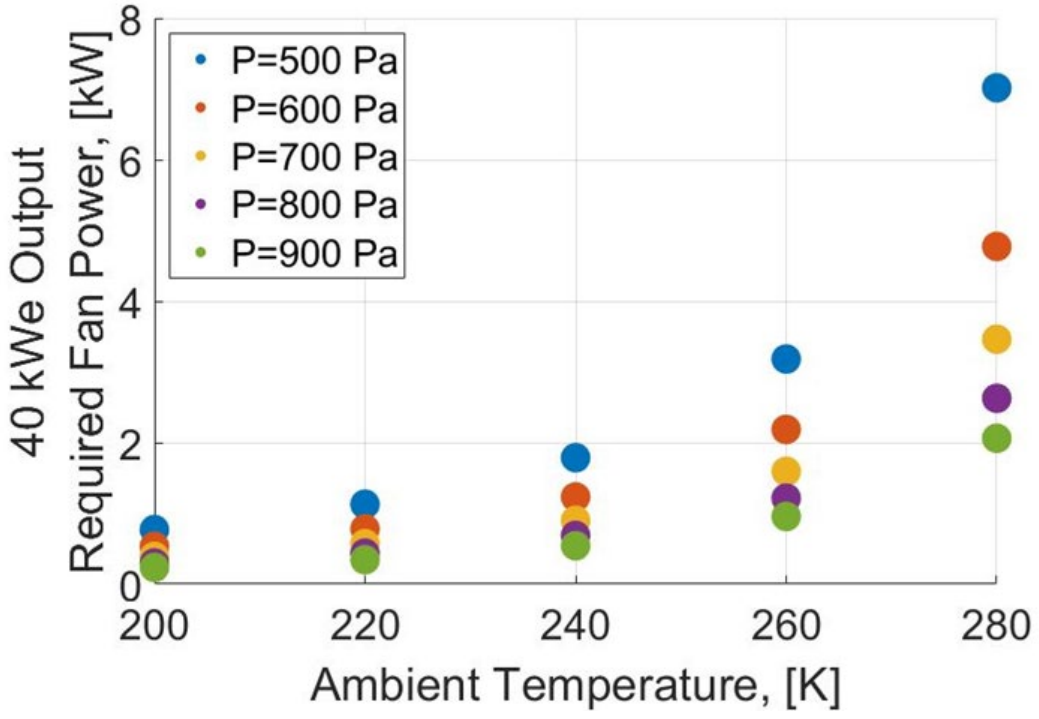

Figure 41: Variation in the required fan power for various ambient conditions

4.4 Cryocooler modeling results

Figure 42 shows the optimal mass of a cryocooler liquefying oxygen at a rate of 100 W using both a radiator and a heat exchanger as a function of the heat rejection temperature for three power specific mass values; 350 kg/kW$_e$ represents a typical photovoltaic/fuel cell combination [62], 180 kg/kW$_e$ represents a FSPS similar in design to NASA's KiloPower concept [62], and 10 kg/kW$_e$ represents a HTGR FSPS similar to that described in the FSPS optimization section above. The actual value resulting from the modelling above was 4.4 kg/kW$_e$ but as the Sondelski model does not include shielding, 10 kg/kW$_e$ was considered more representative of an operational HTGR FSPS. The radiator rejects heat to a 200 K background for each case.

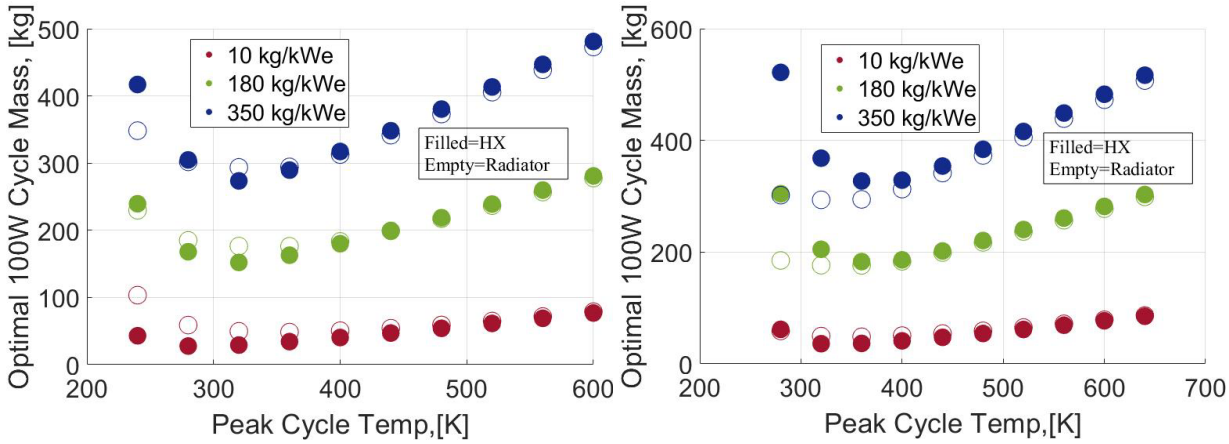

Figure 42: Comparison of the optimal cryocooler system mass using a radiator and HX vs the peak cycle temperature T_4 for various power source specific powers, at an ambient pressure of 600 Pa and temperature of a) 220K and b) 260K.

For an ambient temperature of 220 K, the heat exchanger results in a 43% lower optimal mass for the 10 kg/kWe case, a 14% lower mass for the 180 kg/kWe case, and a 7% lower mass

for the PV/fuel cell option. However, at a 260 K ambient temperature, only for the highest-density power source does the heat exchanger outperform the radiator. As the system mass becomes more sensitive to the required fan power at higher power specific masses, a passive cooling option like a radiator becomes more desirable.

The optimal heat rejection temperature is lower when using a heat exchanger, improving the cycle thermal efficiency. The heat exchanger performance is sensitive to ambient temperature as shown in Figure 43. At 220 K, i.e. the average surface temperature, the heat exchanger outperforms the radiator even for very high-specific-mass power systems across a range of power levels, but at 260 K, a typical summertime peak temperature, the heat exchanger only results in a lower overall mass when coupled with an FSPS. The heat exchanger also becomes more favorable at higher cooling loads. In general, the ratio of the optimal mass using a heat exchanger compared to a radiator decreases as the power source density increases because the total mass is increasingly driven by the required power generation mass and thus the required power. For the radiator cycle, the peak cycle temperature T_4 tends to decrease with increasing α to minimize the required compressor power due to the increasing proportion of the total mass allocated to power generation. The heat exchanger cycle however sees a slight increase in T_4 as α is increased due to the opposing objectives of minimizing compressor power and heat rejection fan power, so the radiator cycle optimizes for lower power usage at high values of α.

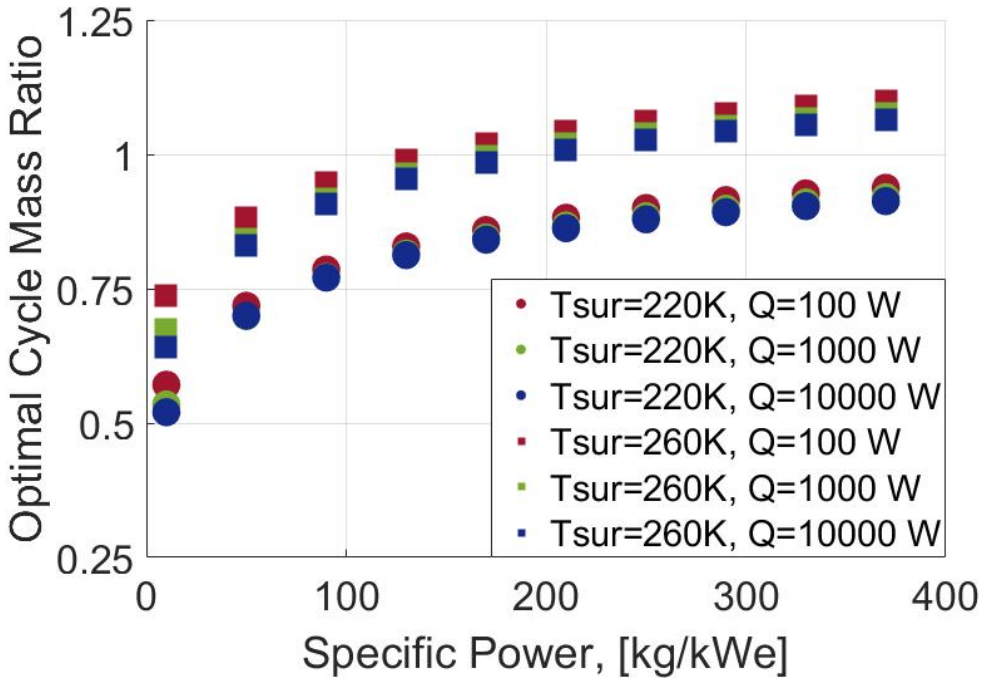

Figure 43: Ratio of the optimal cycle mass using a radiator and heat exchanger vs specific power for ambient temperatures of 220 and 260 K and cooling loads of 100, 1000, and 10000 W.

Interestingly, due to the increased cycle thermal efficiency, the heat exchanger cycle requires less total power than the radiator cycle at 220 K for the lowest specific mass cases even when accounting for the fan power, as shown in Figure 44. While the required power dependence is largely explained above, at the lowest α and Q_{LOx} value the cryocooler itself constitutes the majority of the total system mass and so the mass-optimized system is more strongly driven by the rejection temperature, leading to a higher required fan power for the heat exchanger system.

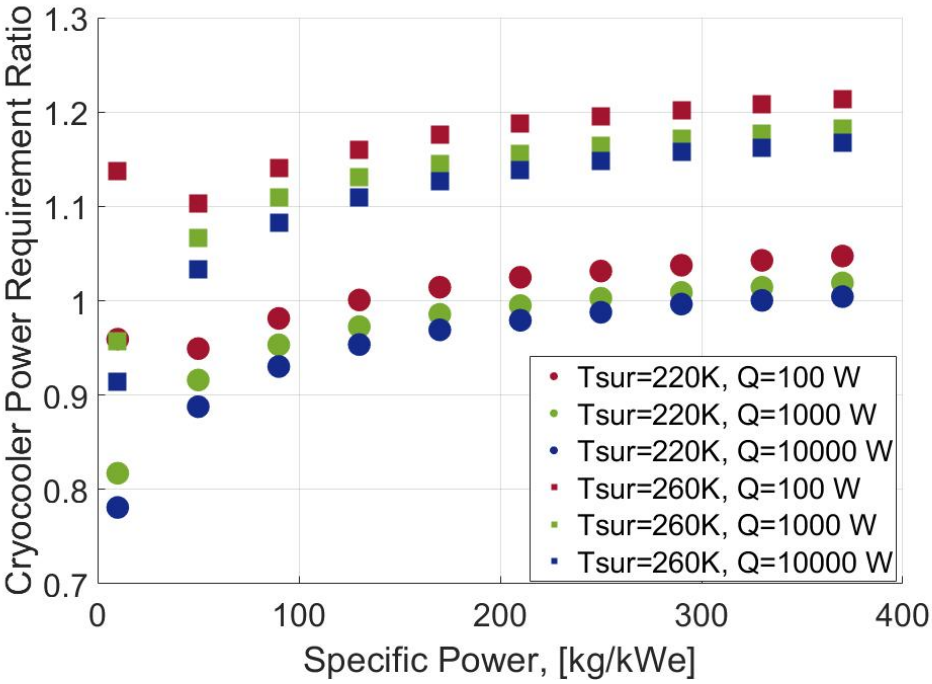

Figure 44: Ratio of the optimal cycle required power using a radiator and heat exchanger vs specific power for ambient temperatures of 220 and 260 K and cooling loads of 100, 1000, and 10000 W.

Using the average temperature for this analysis makes sense though as the LOx flowrate could be varied to take advantage of the cooler ambient temperatures at night and throttled during times of peak temperature and still attain the target average production rate, although the turbomachinery and heat exchangers would have to be sized for the higher peak production rate. Finally, for both ambient temperatures, the heat exchanger area is much less than the radiator area for all specific powers making the entire system more compact, as shown in Figure 45.

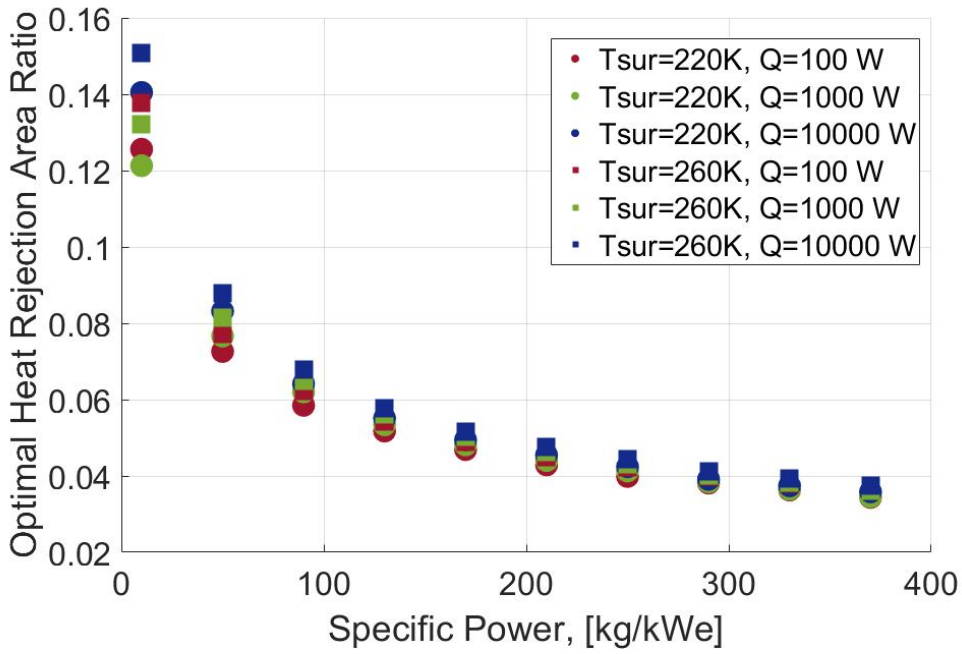

Figure 45: Ratio of the optimal cycle heat rejection area using a radiator and heat exchanger vs specific power for ambient temperatures of 220 and 260 K and cooling loads of 100, 1000, and 10000 W.

5. Conclusions

Nuclear fission power systems are increasingly being investigated as power sources for future Mars applications with high power demands, particularly crewed missions. These power systems are strongly mass-limited and require significant waste heat rejection capacity to operate, however they are typically designed using a radiative heat rejection system due to existing flight heritage and a lack of existing data on forced-convection heat transfer performance in Mars-like conditions. This goal of this dissertation was to demonstrate the feasibility of forced-convection systems on Mars for heat-rejection applications.

To this end, an analytical model of a crossflow, finned-tube heat exchanger has been developed to predict the mass, size, and power requirement of a forced-convection heat

exchanger in Mars surface conditions and is described in Section 2.1. The model first determines the required gas flowrate through the heat exchanger using an existing Nusselt number correlation and the effective-NTU method. Then the required fan power is determined using an existing Euler number correlation and fan efficiency correlation. The mass of the heat exchanger is determined based on the heat exchanger material and geometry and the fan mass is determined based on the fan power, size, and an estimate for the fan specific mass. Finally, mass penalties for the required fan power and the coolant pressure drop are determined to account for the additional load on the FSPS.

An optimization model is also developed to determine the optimal heat exchanger geometry to minimize the total mass for a given set on heat rejection parameters, ambient conditions, and the tube material and layout and is described in Section 2.2. The heat exchanger model and optimizer were used to generate reduced order models of the optimal heat exchanger specific conductance, gas-side capacity rate, and required fan power. These models were integrated into Sondelski's Mars FSPS thermal cycle optimization model to determine the effect of using a forced convection heat exchanger for waste heat rejection rather than a radiator, as described in Section 2.3.

Liquid Oxygen cryocooling may also be a useful application of forced-convection waste heat rejection on Mars. The in-situ production at a high rate LOx for use as an oxidizer for rocket propulsion could enable significantly more down-mass capability or shorter trip times on future Mars missions by obviating the need to bring oxidizer from Earth for the return journey. A single-stage recuperated reverse Brayton cycle cryocooler model was developed to determine the minimal-mass cryocooler to produce a given LOx production rate using both a radiator and forced

convection heat exchanger and described in Section 2.4. For a given compressor pressure ratio, peak cycle temperature, recuperator conductance, and LOx production rate, the model first solves for the required working fluid mass flowrate, and subsequently finds the required compressor power and total rejected heat load. Reduced order models based on the rejected heat load, temperature, and ambient conditions are used to determine the required heat exchanger mass and power. The total system mass is then determined using mass models for the cryocooler, recuperator, and a supplied electrical power source specific mass.

The modelling effort relied on existing correlations for the Euler and Nusselt number to predict the heat exchanger performance. These correlations have not been benchmarked in relevant Mars-like conditions, namely in low Reynolds, moderate Knudsen, vortical flow. To validate the modelling predictions, an experimental prototype heat exchanger and a low-pressure test facility were designed and constructed to gather data on the performance of a tube bank crossflow heat exchanger in Mars-like conditions. Experiments were carried out to measure the pressure drop and Nusselt number of the heat exchanger under a range of pressures, heat fluxes, and gas flowrates, in CO_2 and in air, and under both axial flow and vortical flow conditions. Correlations for the Euler number and Nusselt number for a staggered tube bank in axial and vortical crossflow have been developed for a Reynolds number range of 7-150, a Knudsen number range of 0.0009-0.009, and a vorticity, quantified by the blade tip velocity ratio, of 0-14.

The measured pressure drop for the axial flow case exceeded the HEDH correlation prediction significantly at Reynolds numbers from 7-75 and showed reasonable agreement above 75. There was a slight positive trend in the measured-to-predicted pressure drop with respect to Knudsen number. The vortical flow pressure drop slightly exceeded the axial flow values by a

degree approximately in line with Moore et al.'s findings in finned tubes in turbulent flows, suggesting this effect is insensitive to geometry and Reynolds number, but does depend on the degree of vorticity, represented here by the blade velocity ratio. A correlation was generated to predict the pressure drop in a 2 column staggered-tube heat exchanger that closely fits the experimental data. The axial flow Nusselt numbers slightly exceeded the predicted values based on the Tariq et al. correlation at Reynolds number below 30 but were well-predicted at higher Reynolds numbers. A slight negative trend in the measure-to-predicted Nusselt number with respect to the Knudsen number is observed. Combined with the negative trend in the Tariq et al. correlation with Knudsen number, this suggests that the Knudsen number does have an effect at values between 0.0009-0.009. The Tariq et al. correlation closely estimates the Nusselt number in the vortical cases studied, again suggesting the heat transfer findings of Moore et al. may be insensitive to geometry. A new correlation is also proposed to estimate the Nusselt number in low-Reynolds, moderate Knudsen vortical flows that accurately estimates the measured Nusselt number.

Overall, the experimental work presents heat exchanger pressure drop and heat transfer data for a staggered-tube array from a previously-unstudied regime of low Reynolds number, moderate Knudsen number crossflow in both axial and vortical flow. This regime is relevant to any attempts to design heat rejection systems capable of operating on Mars, high-altitude Earth platforms such as balloons, or other low-density environments.

The modified HEDH correlation derived from the experimental data was then incorporated into the analytical model to predict optimal heat exchanger geometries and performance in Martian conditions using experimentally-validated correlations for the Euler

number and Nusselt number. The optimal heat exchanger geometry for rejecting waste heat on Mars tends to consist of a staggered tube array with a pitch-to-diameter ratio of at least 2, tube diameter of approximately 1-2 mm, and a minimal number of tube rows in the streamwise direction. Using aluminum resulted in the lowest optimal mass for coolant temperatures below 550°C while titanium would be preferred for higher-temperature applications. For aluminum heat exchangers, the optimal fin pitch tended to be large, between 1-4 mm, while heat exchangers made of other materials performed best without any fins at all. In general the fin pitch did not have a strong effect on the optimal mass.

Overall, the modeling suggests that a forced convection heat exchanger is capable of fulfilling the waste heat rejection requirements of a fission power system over a range of electrical power levels and in the entire range of foreseeable landing site ambient conditions, while have a significantly lower mass and requiring less space than a radiator. The heat exchanger system also exhibits increasing cycle efficiency. The use of the heat exchanger reduces the optimal cycle mass by 78% from 782 kg to 175 kg, both by reducing the waste heat rejection system mass and by reducing the optimal heat rejection temperature which increases thermal efficiency and reduces the required recuperator mass. The heat exchanger cycle has a 73 K lower minimum cycle temperature, increasing thermal efficiency from 27% to 34%. The heat exchanger mass is significantly less than the radiator, and the frontal area of the heat exchanger is 85% less than the required radiator surface area, reducing the need for complex deployment mechanisms. The heat exchanger itself has a mass of only 37 kg, a frontal area of 11.3 m^2, and requires 1806 W of fan power to operate.

Using a forced convection heat exchanger to reject waste heat from an ISRU cryocooler would also result in significant mass and size reductions compared to a radiator-based system, although the benefit tends to be smaller and depends on the ambient temperature and power source density being used. A radiator may result in a lower mass system when a low-density power source like solar power is used in high temperatures due to the increased power requirement of the fan.

Overall, this technology offers significant performance advantages over radiative heat rejection systems for waste heat rejection applications on Mars, and may significantly benefit future crewed Mars missions by reducing the mass budget dedicated to power generation or ISRU systems and thus allowing for more scientific capabilities.

The largest remaining source of uncertainty in this modeling approach, and a possible topic of future work, is the fan efficiency. No experimental data could be found on axial fan performance in the high-head-coefficient, high-Mach, low-Reynolds regime and collecting such data requires the construction of a full-scale (~1 m diameter) fan and testing it within a Mars-like environment.

Bibliography

[1] "The Vision for Space Exploration," National Aeronautics and Space Administration, Washington, D.C., 2004.

[2] "Human Exploration of Mars Design Reference Architecture (DRA) 5.0," National Aeronautics and Space Administration, Washington, D.C., 2009.

[3] "Mars 2020 Perserveranec Rover Instruments Summary," National Aeronautics and Space Administration, [Online]. Available: https://mars.nasa.gov/mars2020/spacecraft/instruments/. [Accessed 1 December 2021].

[4] "NASA's Mars 2020 Project," NASA Office of Inspector General Office of Audits, 2017.

[5] L. Mason, "A Comparison of Fission Power System Options for Lunar and Mars Surface Applications," in *Space Technology and Applications International Forum*, 2006.

[6] S. D. Howe, T. Ring, D. Crawford and J. Navarro, "Economical Production of Pu-238," in *Nuclear and Emergent Technologies for Space*, Albuquerque, NM, 2013.

[7] P. L. Roggenkamp, "Pu-238 Production at the Savannah River Plant," in *American Nuclear Society Winter Meeting*, Los Angeles, CA, 1987.

[8] C. Willis, "Radiological Hazards Comparison of SNAP 9A to SNAP 10A," North American Aviation, 1963.

[9] G. Bennett, "Space Nuclear Power: Opening the Final Frontier," in *4th International Energy Convesion Engineering Conference and Exhibit*, San Diego, 2006.

[10] B. Sondelski, "Mass Optimization of a Supercritical CO2 Brayton Cycle with a Direct Cooled Nuclera Reactor for Space Surface Power," University of Wisconsin, Madison, WI, 2019.

[11] C. Morrison, "Temperature and Power Specific Mas Scaling for Commercial Closed-Cycle Brayton Systems in Space Surface Power and Nuclear Electric Propulsion Applications," *Nuclear Technology,* vol. 206, no. 8, pp. 1224-1239, 2020.

[12] R. N. Brown, "Fan Laws, the Use and Limits in Predicting Centrigual Compressor Off Design Performance," Texas A&M University Turbomachinery Laboratories, College Station, TX, 1991.

[13] J. Bezanson, A. Edelman, S. Karpinski and V. B. Shah, "Julia: A fresh approach to numerical computing," *SIAM Review,* vol. 59, no. 1, pp. 65-98, 2017.

[14] L. Mason, "Surface Nuclear Power for Human Mars Missions," in *Space Technology and Applications International Forum*, 1999.

[15] R. Sovie, "SP-100 Advanced Technology Program," in *22nd Intersociety Energy Conversion Engineering Conference*, Philadelphia, PA, 1987.

[16] G. Feller and R. Joyner, "Pratt & Whitney ESCORT Deriviative for Mars Surface Power," in *Space Technology and Applications International Forum*, 1999.

[17] L. Mason and D. Poston, "Fission Surface Power System Initial Concept Definition," National Aeronautics and Space Administration, Cleveland, OH, 2010.

[18] M. Gibson, S. Oleson, D. Poston and P. McClure, "NASA's Kilopower Reactor Development and the Path to Higher Power Missions," in *IEEE Aerospace Conference*, 2017.

[19] P. McClure, D. Poston, M. Gibson, L. Mason and R. Robinson, "Kilopower Project: The KRUSTY Fission Power Experiment and Potential Missions," *Nuclear Technology,* vol. 206, pp. S1-S12, 2020.

[20] A. von Arx and A. Delgado, "Convective Heat Transfer on Mars," in *AIP Conference Proceedings*, 1991.

[21] J. Breedlove, "Ultra-Compact Heat Rejection System for Fission Surface Power, Phase I," 2016. [Online]. Available: https://techport.nasa.gov/view/33318.

[22] A. Zukauskas, "Heat Transfer from Tubes in Crossflow," *Advances in Heat Transfer,* vol. 18, pp. 87-159, 1987.

[23] G. Gamrat, M. Favre-Marinet and S. Le Person, "Numerical Study of Heat Transfer Over Banks of Rods in Small Reynolds Number Crossflow," *International Journal of Heat and Mas Transfer,* vol. 51, pp. 853-864, 2007.

[24] H. Fugmann, L. Schnabel and B. Frohnapfel, "Heat Transfer and Pressure Drop Correlations for Laminar Flow in an In-Line and Staggered Array of Circular Cylinders," *Numerical Heat Transfer,* vol. 75, no. 1, pp. 1-20, 2019.

[25] R.-z. Jia, Y.-c. Wang, J. Guo, Z.-y. Yu and H.-f. Kang, "Research on the Heat Transfer and Flow Characteristics of Fin-Tube Heat Exchangers Under Low Pressure Environment," *Applied Thermal Engineering,* vol. 112, pp. 1163-1171, 2017.

[26] F. Xie, Y. Li, Z. Liu, X. Wang and L. Wang, "A Forced Convection Heat Transfer Correlation of Rarefied Gases Cross-Flowing Over a Circular Cylinder," *Experimental Thermal and Fluid Science,* vol. 80, pp. 327-336, 2017.

[27] R. Blevins, Flow-Induced Vibration, Van Nostrand Reinhold, 1990.

[28] Y. Peles, A. Kosar, C. Mishra, C.-J. Kuo and B. Schneider, "Forced Convection Heat Transfer Across a Pin Fin Micro Heat Sink," *Internationa Journal of Heat and Mass Transfer,* vol. 48, no. 17, pp. 3615-3627, 2005.

[29] Heat Exchanger Design Handbook, New York: Hemisphere, 1983.

[30] A. Tariq, P. Li, A. Xu and Z. Liu, "A Correlation for Nusselt Number of Slip Gas Flow in Confined Porous Media," *Journal of Heat Transfer,* vol. 142, 2020.

[31] J. Moore, R. Grimes, A. O'Donovan and E. Walsh, "Design and Testing of a Novel Air-Cooled Condenser for Concentrated Solar Power Plants," *Energy Procedia,* vol. 49, pp. 1439-1449, 2014.

[32] E. Gianolio and F. Cuti, "Heta transfer and Pressure Drop for Air Coolers with Different Numbers of Rows Under Induced and Forced Draft," *Heat Transfer Engineering,* vol. 3, no. 1, pp. 38-48, 1981.

[33] P. W. Eckels and T. J. Rabas, "Heat Transfer and Pressure Drop of Typical Air Cooler Finned Tubes," *Journal of Heat Transfer,* vol. 107, no. 1, pp. 198-204, 1985.

[34] B. White, B. Lacchia, R. Greeley and R. Leach, "Aeolian Behavior of Dust in a Simulated Martian Environment," *Journal of Geophysical Research,* vol. 102, pp. 629-640, 1997.

[35] J. Merrison, H. Bechtold, H. Gunnlaugsson, A. Jensen, K. Kinch, P. Nornberg and K. Rasmussen, "An Environmental Simulation Wind Tunnel for Studying Aeolian Transport on Mars," *Planetary and Space Science,* vol. 56, no. 3-4, pp. 426-437, 2007.

[36] M. Veismann, C. Dougherty, J. Rabinovitch, A. Quon and M. Gharib, "Low-Density Multi-Fan Wind Tunnel Design and Testing for the Ingenuity Mars Helicopter," *Experiments in Fluids,* vol. 193, no. 62, 2021.

[37] J. Merrison, H. Gunnlaugsson, P. Nornberg, A. Jensen and K. Rasmussen, "Determination of the Wind Inudced Detachement Threshold for Granular Material on Mars Using Wind Tunnel Simulations," *Icarus,* vol. 191, no. 2, pp. 568-580, 2007.

[38] I. Bell, J. Wronski, S. Quoilin and V. Lemort, "Pure and Psuedo-pure Fluid Thermophysical Property Evaluation and the Open-Source Thermophysical Property Library CoolProp," *Industrial & Engineering Chemistry Research,* vol. 53, no. 6, pp. 2498-2508, 2014.

[39] D. Rich, "The Effect of Fin Spacing on the Heat Transfer and Friction Performance of Multirow, Smooth Plate Fin Tube Heat Exchanger," *ASHRAE Transactions,* vol. 79, pp. 137-145, 1973.

[40] A. A. Zukauskas and R. V. Ulinskas, Heat Transfer in Tube banks in Crossflow, New York: Hemisphere, 1988.

[41] G. Nellis and S. Klein, Heat Transfer, New York, NY: Cambridge University Press, 2009.

[42] D. J. a. S. N. D. Zigrang, "Explicit Approximations to the Solution of Colebrook Friction Factor Equation," *AIChE Journal,* vol. 28, no. 3, 1982.

[43] Tubular Exchanger Manufacturers Association, "Standards of the Tubular Exchanger Manufacturers Association," Tubular Exchanger Manufacturers Association, Tarrytown, NY, 2007.

[44] D. Quin and R. Grimes, "The Effect of Reynolds Number on Microaxial Flow Fan Performance," *Journal of Fluids Engineering,* vol. 130, 2008.

[45] J. Neustein, "Low Reynolds-Number Experiemnts in an Axial-Flow Turbomachine," *Journal of Engineering for Power,* vol. 86, no. 3, pp. 257-295, 1964.

[46] H. Glauert, "The Effect of Compressibility on the Lift of an Airfoil," *Proceedings of the Royal Society of London Series A-containing Papers of a Mathematical and Physical Character,* vol. 118, pp. 113-119, 1928.

[47] R. Feldt, "github.com," 2019. [Online]. Available: https://github.com/robertfeldt/BlackBoxOptim.jl. [Accessed 2021].

[48] A. Swenson, "Surrogate Reactor Modelling for Space Electrical System Mass Optimization," University of Wisconsin, Madison, WI, 2019.

[49] K. Lee, D.-Y. K. J. Koh, H. Yeom, C.-H. Son and J.-I. Yoon, "Design and Performance Test of 2 kW Class Reverse Brayton Cryogenic System," *Energies,* vol. 13, 2020.

[50] D. Plachta and P. Kittel, "An Updated Zero Boil-off Cryogenic Propellant Storage Analysis Applied to Upper Stages or Depots in an LEO Environment," National Aeronautics and Space Administration, Cleveland, OH, 2003.

[51] A. Niblick, J. Cox and M. Zaragola, "A Lightweight, High-Effectiveness Recuperator for Next-Generation Airborne Cryocoolers," in *International Cryocooler Conference*, Boulder, CO, 2018.

[52] M. Zaragola, J. Breedlove and K. Cragin, "Demonstration of a High-Capacity Cryocooler for Zero Boil-Off Cryogen Storage in Space," in *International Cryocooler Conference*, Boulder, CO, 2012.

[53] A. Juhasz, "Heat Transfer Analysis of a Closed Brayton Cycle Space Radiator," National Aeronautics and Space Administration, Cleveland, OH, 2007.

[54] Engineering Sciences Data Unit, "Convective Heat Transfer During Crossflow of Fluids Over Plain Tube Banks," London, 1973.

[55] J. Hust and A. Lankford, "Update of Thermal Conductivity and Electrical Resistivity of Electrolytic Iron, Tungsten, and Stainless Steel," National Bureau of Standards, Boulder, CO, 1984.

[56] R. I. Loehrke and H. M. Nagib, "Experiments of Managenment of Free-Stream Turbulence," AGARD, 1972.

[57] S. W. Churchill and H. Ozoe, "Correlations for Laminar Forced Convection with Uniform Heating in Flow over a Plate and in Developing and Fully Developed Flow in a Tube," *Journal of Heat Transfer,* vol. 95, no. 1, pp. 78-84, 1973.

[58] L. Han, "Hydrodynamic Entrance Lengths for Incompressible Laminar Flow in Rectangular Ducts," *Journal of Applied Mechanics,* vol. 27, no. 3, pp. 403-409, 1960.

[59] R. K. Shah and A. L. London, Laminar Flow Forced Convection in Ducts, 1978.

[60] R. Webb, "Entrance and Exit Losses for Developing Flow in Parallel PLate Channels," *Heat Transfer Engineering,* vol. 27, no. 10, 2006.

[61] S. A. Klein, "EES-Engineering Equation Solver," F-Chart Software, 29 11 2022. [Online]. Available: https://fchartsoftware.com. [Accessed 29 03 2023].

[62] M. A. Gibson, S. R. Oleson, D. I. Poston and P. McClure, "NASA's Kilopower Reactor Development and the Path to Higher Power Missions," in *IEEE Aerospace Conference*, Big Sky, MT, 2017.